NICKEL-BASED ANODIC ELECTROCATALYSTS

FOR FUEL CELLS AND WATER SPLITTING

by

Dayi Chen

A dissertation submitted to the faculty of
The University of Utah
in partial fulfillment of the requirements for the degree of

Doctor of Philosophy

Department of Chemistry

The University of Utah

May 2016

The University of Utah Graduate School

STATEMENT OF DISSERTATION APPROVAL

The dissertation of **Dayi Chen**

has been approved by the following supervisory committee members:

Shelley D. Minteer	, Chair	**January 7th 2016** Date Approved
Cynthia J. Burrows	, Member	**January 7th 2016** Date Approved
Matthew Kieber-Emmons	, Member	**January 7th 2016** Date Approved
Jon D. Rainier	, Member	**January 7th 2016** Date Approved
Jules J. Magda	, Member	**January 7th 2016** Date Approved

and by **Cynthia J. Burrows** , Chair/Dean of

the Department/College/School of **Chemistry**

and by David B. Kieda, Dean of The Graduate School.

ABSTRACT

Our world is facing an energy crisis, so people are trying to harvest and utilize energy more efficiently. One of the promising ways to harvest energy is via solar water splitting to convert solar energy to chemical energy stored in hydrogen. Another of the options to utilize energy more efficiently is to use fuel cells as power sources instead of combustion engines. Catalysts are needed to reduce the energy barriers of the reactions happening at the electrode surfaces of the water-splitting cells and fuel cells. Nickel-based catalysts happen to be important nonprecious electrocatalysts for both of the anodic reactions in alkaline media. In alcohol fuel cells, nickel-based catalysts catalyze alcohol oxidation. In water splitting cells, they catalyze water oxidation, i.e., oxygen evolution. The two reactions occur in a similar potential range when catalyzed by nickel-based catalysts. Higher output current density, lower oxidation potential, and complete substrate oxidation are preferred for the anode in the applications.

In this dissertation, the catalytic properties of nickel-based electrocatalysts in alkaline medium for fuel oxidation and oxygen evolution are explored. By changing the nickel precursor solubility, nickel complex nanoparticles with tunable sizes on electrode surfaces were synthesized. Higher methanol oxidation current density is achieved with smaller nickel complex nanoparticles. DNA aggregates were used as a polymer scaffold to load nickel ion centers and thus can oxidize methanol completely at a potential about

0.1 V lower than simple nickel electrodes, and the methanol oxidation pathway is changed. Nickel-based catalysts also have electrocatalytic activity towards a wide range of substrates. Experiments show that methanol, ethanol, glycerol and glucose can be deeply oxidized and carbon-carbon bonds can be broken during the oxidation. However, when comparing methanol oxidation reaction to oxygen evolution reaction catalyzed by current nickel-based catalysts, methanol oxidation suffers from high overpotential and catalyst poisoning by high concentration of substrates, so current nickel-based catalysts are more suitable to be used as oxygen evolution catalysts. A photoanode design that applies nickel oxides to a semiconductor that is incorporated with surface-plasmonic metal electrodes to do solar water oxidation with visible light is proposed.

TABLE OF CONTENTS

ABSTRACT iii

LIST OF TABLES viii

LIST OF FIGURES ix

ACKNOWLEDGEMENTS xiii

Chapters

1. INTRODUCTION 1

    1.1 The Energy Crisis: Role of Solar Water Splitting and Fuel Cells 1
    1.2 Alkaline Direct Alcohol Fuel Cells and Nickel-based Anodic Electrocatalysts 3
        1.2.1 Alkaline Direct Alcohol Fuel Cells 3
        1.2.2 Nickel-based Anodic Electrocatalysts for Alkaline Direct Alcohol Fuel Cells 6
    1.3 Solar Water Splitting and Nickel-based Anodic Electrocatalysts 9
        1.3.1 Solar Water Splitting 9
        1.3.2 Nickel-based Anodic Electrocatalysts for Solar Water Splitting 10
    1.4 Characterization Techniques Background 11
        1.4.1 X-ray Photoelectron Spectroscopy (XPS) 12
        1.4.2 Cyclic Voltammetry (CV) 13
        1.4.3 Chronoamperometry (CA) 16
    1.5 Summary 17
    1.6 References 18

2. NICKEL CYSTEINE COMPLEXES AS ANODIC ELECTROCATALYSTS FOR FUEL CELLS 20

    2.1 Introduction 21
    2.2 Experimental 22
        2.2.1 Reagents 22
        2.2.2 Apparatus 22
        2.2.3 Electrodes Preparation 24

2.2.4 Chronoamperometry 24
2.3 Results and Discussion 25
2.3.1 Cysteine Effects on Nickel Catalyst Deposition 25
2.3.2 Possible Structures of Electrodeposited Ni and NiCys Catalysts 29
2.3.3 Surface Morphology of the Catalysts 41
2.3.4 Methanol Oxidation by Ni and NiCys Electrodes 47
2.4 Conclusion 50
2.5 References 50

3. FUEL DIVERSITY STUDIES OF NICKEL-BASED CATALYSTS AND METHANOL OXIDATION MECHANISM ALTERATION WITH DNA SCAFFOLDS 53

3.1 Introduction 54
3.2 Experimental 56
3.2.1 Reagents 56
3.2.2 Sample Preparation- Electrodeposition 57
3.2.3 Sample Characterization 58
3.3 Results and Discussion 61
3.3.1 Surface Morphologies 61
3.3.2 Electrocatalytic Properties 67
3.3.3 Electronic Transitions in UV-Vis 78
3.3.4 Chemical Composition Analysis with XPS 81
3.4 Conclusion 93
3.5 References 94

4. MECHANISTIC STUDY OF NICKEL-BASED CATALYSTS FOR OXYGEN EVOLUTION COMPARED TO METHANOL OXIDATION REACTIONS IN ALKALINE MEDIUM 98

4.1 Introduction 99
4.2 Experimental 101
4.2.1 Reagents and Apparatus 101
4.2.2 Electrodes Preparation 102
4.2.3 Chronoamperometry 103
4.2.4 Stability Tests via Bulk Electrolysis 105
4.3 Results and Discussions 105
4.3.1 Cyclic Voltammetry 105
4.3.2 Chronoamperometry 113
4.3.3 Electrode Stability Test 130
4.4 Conclusions 133
4.5 References 133

5. CONCLUSION AND FUTURE WORK 136

5.1 References 140

LIST OF TABLES

1.1. Some metal prices in 2014.....7

2.1. Deconvolutional components of oxygen 1s XPS spectra.....32

3.1. Particle sizes of electrodeposited samples on GC plates.....64

3.2. Fuel oxidation peak position and peak current at Ni and DNA-Ni electrodes.....69

3.3. Product distributions of the oxidations of methanol, ethanol, glycerol and glucose.....72

3.4. Formaldehyde oxidation peak position and peak current.....75

3.5. The atomic concentrations (%) of elements in DNA and DNA-Ni.....82

3.6. XPS high-resolution C 1s spectra of DNA and DNA-Ni aggregates.....86

4.1. Preparation of nickel-based electrodes.....104

4.2. Properties of nickel-based electrodes.....108

4.3. Bulk electrolysis data comparison.....132

LIST OF FIGURES

1.1. Schematic diagram of a fuel cell 4

1.2. Simulated cyclic voltammetry process 15

2.1. Nickel catalyst deposition: representative cyclic voltammograms of Ni and NiCys AS-4 electrodes in 0.1 M NaOH. Scan rate 50 mV/s, 30 cycles. (A) 0.01 M NiCl2 precursor. (B) 0.01 M NiCl2 and 0.05 M cysteine precursor. 26

2.2. Nickel catalysts deposition: (A) Representative 30th cycle of cyclic voltammograms from scanning Ni and NiCys AS-4 electrodes in 0.1 M NaOH. (B) Representative 30th cycle of cyclic voltammograms from scanning Ni1Cys6 AS-4 electrodes in 0.1 M NaOH. (C) Electrons produced by cysteine oxidation and NiOOH surface concentration versus cysteine concentration..... 28

2.3. XPS spectra: (A) Nickel 2p. (B) Carbon 1s. (C) Oxygen 1s. (D) Nitrogen 1s. (E) Sulfur 2p..... 30

2.4. Deconvolutional oxygen 1s XPS spectra: (A) Ni sample (FWHM 1.66 eV). (B) Ni-cys sample (FWHM 1.59 eV). 33

2.5. FTIR spectra of relevant samples: (A) Bare glassy carbon plate, electrodeposited Ni sample and chemically prepared Ni1Cys5 sample. (B) Chemically prepared cysteine (pH 5.73) and cysteine in 0.1 M NaOH samples. (C) Chemically prepared cysteine in 0.1 M NaOH and Ni1Cys5 samples..... 35

2.6. The possible structure of oxidized cysteine in the Ni1Cys5 sample. 37

2.7. Possible structures of Ni and NiCys samples, newly prepared by electrodeposition. 40

2.8. AFM 3D height sensor images: (A) Bare glassy carbon plate. (B) Ni1Cys0.5 catalyst deposited with 0.01 M NiCl2 and 0.005 M cysteine precursor. (C) Ni1Cys2 catalyst deposited with 0.01 M NiCl2 and 0.02 M cysteine precursor. (D) Ni1Cys5 catalyst deposited with 0.01 M NiCl2 and 0.05 M cysteine precursor. (E) Ni catalyst deposited with 0.01 M NiCl2 precursor, area with large aggregates. (F) Ni catalyst deposited with 0.01 M NiCl2 precursor, area with small particles..... 42

2.9. From left to right: NiCl2, Cysteine, Ni-cysteine (1:0.5) and Ni-cysteine (1:5)..... 44

2.10. Nickel catalysts deposition: The representative 30th cycles of cyclic voltammograms from scanning Ni and NiCys electrodes in 0.1 M NaOH. 46

2.11. (A) Representative cyclic voltammograms of Ni and NiCys AS-4 electrodes in 0.1 M NaOH and 0.1 M methanol. (B) Chronoamperometric response for a Ni1Cys0.5 (0.01 M NiCl2 and 0.005 M Cysteine) AS-4 electrode in 0.1 M NaOH and increasing concentrations of methanol at 0.7 V (vs. Hg/HgO). (C) Calibration curves of methanol oxidation for Ni and NiCys AS-4 electrodes. Data were calculated from chronoamperometry experiments (e.g. Figure 2.11B). 48

3.1. AFM 3D height sensor images on GC plates: (A) Bare GC plate. (B) 0.1 M NaCl electrodeposited at 1.8 V. (C) NiCl2 electrodeposited at 1.8 V. (D) DNA electrodeposited at 1.8 V. (E) DNA-Ni electrodeposited at 1.8 V. 62

3.2. AFM 3D height sensor images of DNA-Ni on GC plates: (A) Soaked in DNA-Ni precursor solution for 30 min. (B) DNA-Ni electrodeposited at 0.9 V. 63

3.3. Representative cyclic voltammograms at a scan rate of 0.05 V/s: (A) 0.1 M NaOH. (B) 0.1 M NaOH and 0.1 M methanol. (C) 0.1 M NaOH and 0.1 M ethanol.(D) 0.1 M NaOH and 0.025 M glycerol.(E) 0.1 M NaOH and 0.025 M glucose. 68

3.4. Representative cyclic voltammograms of formaldehyde and formate oxidation in 0.1 M NaOH: (A). 0.1 M formaldehyde at the scan rate of 0.05 V/s. (B) 0.1 M formate at the scan rate of 0.05 V/s. (C) 0.1 M formate at the scan rate of 0.005 V/s. 74

3.5. Representative cyclic voltammograms of formaldehyde oxidation by Ni, PO4-Ni, AMP-Ni, TMP-Ni, CMP-Ni, GMP-Ni and DNA-Ni electrodes in 0.1 M NaOH. Scan rate 0.05 V/s. 77

3.6. UV-Vis spectra of NiCl2, ligand-Ni and DNA-Ni after 1.8 V treatments: (A). NiCl2 before and after 1.8 V. (B). Ligand-Ni and DNA-Ni after 1.8 V showing the aromatic ring absorption range. (C). Ligand-Ni and DNA-Ni after 1.8 V showing the Ni2+ d-d transition absorption range. 79

3.7. Normalized UV-Vis spectra of ligand and ligand-before and after applying potentials: (A). CMP-Ni. (B). TMP and TMP-Ni. (C). GMP and GMP-Ni. (D). AMP and AMP-Ni. (E). DNA and DNA-Ni. 80

3.8. Chemical structures of the nucleotides used in this study and possible oxidation products. 84

3.9. XPS high-resolution deconvolution C 1s spectra: (A) DNA aggregates. (B) DNA-Ni aggregates. 87

3.10. XPS spectra (subtracted the Shirley backgrounds, and for quick comparing the peaks' shapes, all the peaks were normalized with their own highest peak intensities):

(A) Carbon. (B) Phosphorus. (C) Nitrogen. (D) Oxygen. 89

3.11. XPS Ni 2p spectra: (A). XPS high-resolution deconvolution Ni 2p spectra (Asymetric peak shape for peaks. (B). DNA-Ni spectrum compared to Cysteine-Ni and Ni spectra in Chapter 2..... 92

4.1. Depositing nickel catalysts onto electrode surfaces: (A) Representative 30th cycle of cyclic voltammograms from scanning electrodes modified with nickel-based catalysts in 0.1 M NaOH. (B). E1/2 and □ Ep trends vs. nickel catalyst thickness. 106

4.2. Representative 30th cycle of cyclic voltammograms from scanning electrodes modified with nickel-based catalysts in 0.1 M methanol and 0.1 M NaOH..... 111

4.3. Representative 30th cycle of cyclic voltammograms from scanning Ni and NiCys AS-4 electrodes in 0.1 M NaOH and in 0.1 M NaOH with 0.1 M methanol (using the same electrode respectively).. 112

4.4. Amperometric response for electrode with 0.01 M NiCl2 and 0.005 M Cysteine in 0.1 M NaOH and increasing concentrations of methanol at 0.7 V (vs. Hg/HgO).... 115

4.5. Methanol oxidation for different nickel-based electrodes: (A). Calibration curves of methanol oxidation for different nickel-based electrodes. Data were calculated from amperometry experiments (Figure 4.4). (B). Turnover frequency (TOF) of methanol oxidation with different nickel-based electrodes. (C). NiOOH reaction order change vs. methanol concentrations..... 116

4.6. Fitting of NiOOH reaction order for methanol oxidation with 0.1 M NaOH. Electrodes were from category I. 117

4.7. Fitting of methanol reaction order in methanol oxidation with 0.1 M NaOH.. 121

4.8. Langmuir plot of methanol (0.05 M to 1.0 M) adsorption in 0.1 M NaOH. 123

4.9. Representative amperometric response for Ni1 electrode with 0.01 M NiCl2 in 0.1 M Methanol at a series pH at 0.607 V (vs. SCE) and 0.7 V (vs. Hg/HgO)..... 125

4.10. (A) and (B) are calibration curves for different nickel-based electrodes at different pH. Data were calculated from amperometry experiments (e.g., Figure 4.9). (A).With 0.1 M methanol. (B).Without methanol. (C) and (D) are TOF of different nickel-based electrodes. (C).With 0.1 M methanol. (D).Without methanol, i.e. TOF_{oxygen}. (E). The difference between (C) and (D), the result of $TOF_{with\ methanol}$ minus $TOF_{no\ methanol}$, i.e. $TOF_{methanol}$ (F). $TOF_{methanol}$ over TOF_{oxygen}. 126

4.11. Fitting of OH- reaction order in the presence of 0.1 M methanol.. 128

4.12. Fitting of OH- reaction order with oxygen evolution reaction.. 129

4.13. Potentiostatic bulk electrolysis of Ni1 AS-4 and Ni1Cys5 AS-4 electrodes in 0.1 M NaOH and 0.1 M 13C-methanol. The potential is hold at 0.7 V (vs. Hg/HgO). 131

5.1. The diagram of the photoanode design. 138

ACKNOWLEDGEMENTS

I would like to express my sincere gratitude to my advisor, Prof. Shelley D. Minteer for her guidance, understanding, patience, and most importantly, for giving me the freedom to explore the research on my own and guiding me carefully throughout my projects. When I first met her, I was at the point of having a little doubt about whether I should continue studying chemistry. Her support on my research ideas greatly encouraged me and now I have confidence to do research in chemistry and really take pleasure in doing research.

Besides my advisor, I would like to thank the rest of my supervisory committee: Prof. Cynthia J. Burrows, Prof. Jon D. Rainier, Prof. Kenneth J. Woycechowsky, Prof. Jules J. Magda and Prof. Matthew Kieber-Emmons, for their encouragements, insightful comments, and support. Prof. Cynthia J. Burrows' "Nucleic Acid" class inspired me to use DNA as scaffolds, which became the work in Chapter 3. Prof. Kenneth J. Woycechowsky has left the Department of Chemistry in the University of Utah, but I would remember his sincere conversation with me about how he worked as a graduate student, as a postdoc, and finally became a professor to arrange a whole research group, which inspired me a lot.

I would also like to thank all of the members of the Minteer research group, especially Dr. Fabien F. Giroud for his research advice, Dr. Michelle Rasmussen for

proofreading a lot of my writing, and Dr. Lindsey Pelster for various help. All of the members in the Minteer research group create a kind laboratory environment, and I can get help from everybody.

I am grateful for the experience of working in Prof. John Conboy's group. The experience taught me the importance of communication. I would like to thank Dr. Trang Nguyen, Dr. Kathryn Smith, and Dr. Grace Yin Stokes for their understanding, support, and encouragement.

Ms. Jolanda I Hoovey, the Graduate Program Coordinator, is another person I would like to thank. There were millions of times I went to her office to ask for advice, and she always thought carefully and gave the advice best for my situation.

A lot of the characterization of my research work was done in the Utah Nanofab. Dr. Brian Van Devener and Dr. Paulo Perez did the X-ray photoelectron spectroscopy experiments for me. Dr. Brian Van Devener also taught me how to use atomic force microscopy and scanning electron microscopy. The cleanroom supervisor, Tony L. Olsen, and staff process engineer, Brian Baker, trained me on the instruments in the cleanroom. I warmly appreciate them.

My sincere thanks also go to Prof. Ashutosh Tiwari and his group. They allow me to use the solar simulator in their lab. Each time I went to use the solar simulator, they helped me to set up the instruments and treated me as a group member.

Joining the Materials Research Science and Engineering Center (MRSEC) at the University of Utah is a great opportunity for me. I met and collaborated with people from the Department of Electrical and Computer Engineering. I also mentored undergraduates

for the Research Experience for Undergraduates Summer Programs (REU). I appreciate the efforts of the undergraduate student Haneen Abul-Fadl, who worked with me on the photoanode project.

Last but not the least, I would like to thank my parents and my friends. My parents always have confidence in my experimental skills and my ability to generate interesting research ideas. They encouraged me to study on the other side of the earth, although they miss me a lot. My friends also helped me to overcome the difficulties I encountered during these years. Their support always provides me with the energy to continue.

CHAPTER 1

INTRODUCTION

1.1 The Energy Crisis: Role of Solar Water Splitting and Fuel Cells

Our world is now facing an energy crisis. The current main energy resources are fossil fuels (oil, coal and gas), and the oil supplies are predicted to be depleted in 50-150 years.[1] The extraction, transport, and conventional combustion-based usage of fossil fuels are also polluting our environment. The emission of greenhouse gases, especially carbon dioxide (CO_2), is causing global warming, which will result in a series of negative consequences, such as sea level rise.[2]

Utilization of solar energy is considered a promising solution to the energy crisis. The total worldwide primary energy consumption in 2012 is 17.5 TW,[3] and the magnitude of the available solar power striking the earth's surface is equal to 65000 1.0 TW power plants.[4] This means 0.027% utilization of the sunlight can supply the energy for the whole world in 2012. There are three principal strategies to convert solar energy. The first is to use devices such as photovoltaics to directly convert light to electrical energy. The efficiency can reach 43.5%,[5] but it depends on daylight time and intensity and needs an extra energy storage system to store and distribute the electricity. The second and the third strategies produce energy sources that are easy to store and transport. The second is using nature's photosynthetic apparatus to grow plants and then produce biofuels like

ethanol from them. The energy conversion efficiency of nature's photosynthetic apparatus can achieve 7% under optimum conditions. Feedstocks such as agricultural crops have less than 1% efficiency over their entire lifecycle.[6] The third option involves artificial photosynthesis, converting light to chemical energy (carbohydrates, alcohols, or hydrogen). Solar water splitting is the major artificial photosynthesis reaction under study, because it produces hydrogen and hydrogen is a clean energy source with high theoretical mass energy density.[7] The "solar-to-hydrogen" (STH) efficiency of some solar water-splitting techniques can exceed 10%.[8]

Using fuel cells, a device converting chemical energy stored in the fuels to electricity, as the power sources or energy conversion devices could be part of the solution to the energy crisis. First, fuel cells can convert chemical energy in the fuel to electrical energy with efficiencies of up to 60%,[9] while the efficiency of internal combustion engines for commercial vehicles was only 42% in 2010.[10] Second, fuel cells can use fuels produced by renewable energy sources. Alcohol fuel cells can use alcohols produced from biomass, such as methanol, ethanol, glycerol, and glucose.[11] Hydrogen fuel cells use hydrogen, which can be produced by water splitting and reforming of biomass-derived fuels. Moreover, hydrogen fuel cells emit only water, so there are no air pollutants or CO_2 emissions.[9]

In this dissertation, nickel-based anodic electrocatalysts for alcohol fuel cells and water splitting are studied. Both of these two topics are important in the clean and renewable energy research area, as mentioned above. The following two sections will provide background about alkaline direct alcohol fuel cells and water splitting and explain the advantages of nickel-based anodic electrocatalysts.

1.2 Alkaline Direct Alcohol Fuel Cells and Nickel-based Anodic Electrocatalysts

1.2.1 Alkaline Direct Alcohol Fuel Cells

1.2.1.1 Fuel Cell

A fuel cell is a device for converting chemical energy stored in a fuel to electricity. As shown in Figure 1.1, a fuel cell has an anode and a cathode. The fuel is filled into the anode chamber, and the half reaction of fuel oxidation happens at the anode with a potential E_a. The half reaction of reduction is occurring at the cathode with a potential E_c. Usually air is fed to the cathode and O_2 is reduced to water at the cathode. The cathode and the anode are usually separated by an electrolyte membrane and the ions can move through the membrane. The output potential E will be

$$E = E_c - E_a \tag{1.1}$$

The electrons produced at the anode are driven by this potential to go through an external circuit and feedback to the cathode. A flow of electricity (electrical current) is thus created.

1.2.1.2 Alkaline Direct Alcohol Fuel Cells

Alkaline fuel cells (AFCs) use alkaline media as the electrolyte separating the anode and the cathode, and the redox reactions happen in an alkaline environment. During the 1960s to the 1980s, they were extensively studied, typically using H_2 as the fuel, but then proton exchange membrane fuel cells (PEMFCs) gained popularity, because of the successful development of the Nafion membrane, a proton-exchange membrane that can

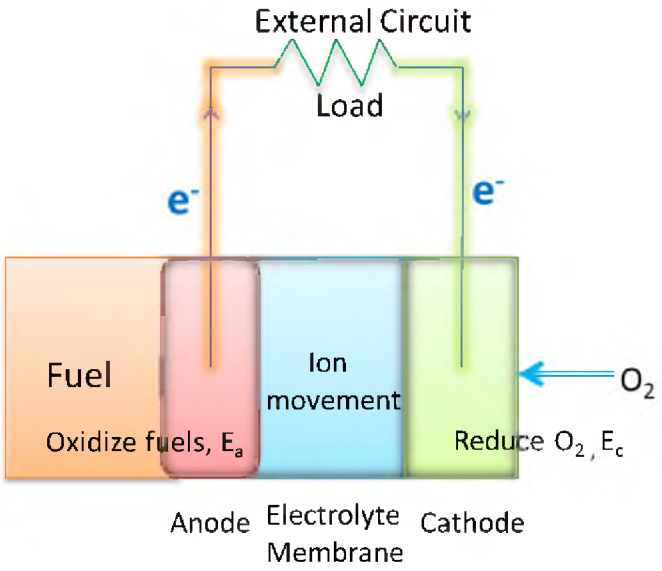

Figure 1.1 Schematic diagram of a fuel cell.

be used as the solid electrolyte. The use of solid or polymer electrolytes can avoid electrolyte leakage, and in the case of AFCs, carbonate precipitation in the electrolyte can also be avoided. Recently, research on alkaline anion-exchange membranes (AAEMs) has been rapidly increasing, because of the commercial development of AAEMs. The studies of AFCs assembled with AAEMs are thus becoming a major research focus again. Compared to PEMFCs, AFCs with AAEMs have many advantages:

a. The kinetics of the oxygen reduction reaction happening at the cathode is more facile.

b. The range of options for the materials for supports and catalysts is wider, including non-noble and low-cost metal (metal oxide) electrocatalysts.

c. Corrosion is less.

d. When using alcohols as the fuel, the alcohol oxidation kinetics can be facilitated in alkaline media and alcohol crossover (alcohols pass through the membrane and get oxidized at the cathode or reduce the effectiveness of the cathode catalysts, resulting in cell voltage decreases) can be inhibited.[12]

Although H_2 is a clean energy source and has high theoretical mass energy density and electrical efficiency, the production, storage, and distribution difficulties of H_2 are still limiting its applications for automobile and portable consumer electronics. On the other hand, alcohols are liquids with high theoretical mass energy densities (methanol 6.1 $kWh \cdot kg^{-1}$ and ethanol 8.0 $kWh \cdot kg^{-1}$ are close to gasoline 10.5 $kWh \cdot kg^{-1}$), so they are easy to handle, easy to store and transport, and thus convenient for those applications. Alkaline direct alcohol fuel cells are now under extensive study in the US and abroad.[13]

When methanol is the fuel used in alkaline media (alkaline direct methanol fuel cells),

the redox reactions will be[14]

$$\text{Anode: } CH_3OH + 6OH^- \rightarrow CO_2 + 5H_2O + 6e^-$$

$$E^o_a = 0.02 \text{ V} - 0.059 \text{ pH V vs NHE (at pH 14, } E^o_a = -0.81 \text{ V)} \quad (1.2)$$

$$\text{Cathode: } 1.5O_2 + 3H_2O + 6e^- \rightarrow 6OH^-$$

$$E^o_c = 1.23 \text{ V} - 0.059 \text{ pH V vs NHE (at pH 14, } E^o_c = 0.40 \text{ V)} \quad (1.3)$$

$$\text{Overall: } CH_3OH + 1.5O_2 \rightarrow CO_2 + 2H_2O$$

$$E^o = E^o_c - E^o_a = 1.21 \text{ V} \quad (1.4)$$

1.2.2 Nickel-based Anodic Electrocatalysts for Alkaline Direct Alcohol Fuel Cells

Although the theoretical output potential of an alkaline direct methanol fuel cell is 1.21 V, in reality it cannot be reached, because of the overpotentials needed at the cathode and the anode. The overpotentials are the extra voltage added to reduce the energy barrier of the reactions. Catalysts are used on the cathode and the anode to reduce the energy barrier and thus lower the overpotentials of the reactions. Platinum group metal-based catalysts are commonly used in fuel cells, but these noble metals are expensive and have limited reserves worldwide. Table 1.1 shows their price (London Metal Exchange, average annual, 2014) as well as the price of nickel. The price of platinum is 2746 times the price of nickel. Also, the world total reserves of all the platinum-group metals (platinum, palladium, rhodium, ruthenium and iridium) are 6.6×10^7 kilograms, while nickel reserves are 8.1×10^{10} kilograms,[15] so developing non-noble and low-cost catalysts, such as nickel-based catalysts, has great advantages over

Table 1.1 Some metal prices in 2014.

Metal	Price (dollars per gram)
Platinum	46.30
Palladium	26.7
Rhodium	37.94
Ruthenium	2.2
Iridium	18.4
Nickel	0.01686

platinum-group catalysts when considering the cost and sustainability.

Nickel-based catalysts are the most investigated nonplatinum anodic electrocatalysts for methanol oxidation in alkaline media.[12] Since Fleischmann et al. published the first results of the oxidation of organic compounds (amines, alcohols, and so on) at nickel electrodes in alkaline media in 1971,[16] numerous studies of nickel-based catalysts have followed. Because nickel electrodes with a planar surface show poor catalytic activities,[17] most of the studies turn to perovskite oxides that contain nickel, nickel alloys (Ni-Cr, Ni-Cu, Ni-Ru), and nickel macrocyclic complexes. These methods disperse nickel centers in three-dimensional structures and have higher alcohol oxidation current density than planar nickel electrodes.[12] Most of the studies agree that the catalytic active species is Ni[III]:

$$Ni(OH)_2 + OH^- \rightleftharpoons NiOOH + H_2O + e^- \quad (1.5)$$

NiOOH (Ni-oxyhydroxide) then oxidizes the alcohol to the corresponding carboxylate and carbonate. When carbonate is the oxidation product, this means the alcohol has been completely oxidized and all of the energy stored in the chemical bonds is released.[18]

Other than the compositions of the nickel-based catalysts, the concentration of OH^-, morphology of the modifying catalyst layer (thickness and permeability), surface concentration of active sites, charge transport through the catalyst layer, and the electron transfer rate at the substrate/nickel hydroxide interface all affect a catalyst's efficiency.[19-21] These are the factors that also need to be optimized for a nickel-based catalyst. The fuel oxidation half reactions catalyzed by nickel-based catalysts are characterized in this

dissertation.

1.3 Solar Water Splitting and Nickel-based Anodic Electrocatalysts

1.3.1 Solar Water Splitting

The water-splitting reaction breaks water into H_2 and O_2, and the produced H_2 can be used as a carbon-free energy source and an energy-rich reagent to store atmospheric CO_2 in the form of methane, methanol, or even hydrocarbons.[5] In alkaline media, the reactions will be[1]

$$\text{Anode: } 4OH^- \rightarrow O_2 + H_2O + 4e^-$$

$$E^o_a = 1.23 \text{ V} - 0.059 \text{ pH V vs NHE (at pH 14, } E^o_a = 0.40 \text{ V)} \quad (1.6)$$

$$\text{Cathode: } 4H_2O + 4e^- \rightarrow 2H_2 + 4OH^-$$

$$E^o_c = 0 \text{ V} - 0.059 \text{ pH V vs NHE (at pH 14, } E^o_c = -0.83 \text{ V)} \quad (1.7)$$

$$\text{Overall: } 2H_2O \rightarrow O_2 + 2H_2$$

$$E^o = E^o_c - E^o_a = -1.23 \text{ V} \quad (1.8)$$

The overall E^o of -1.23 V indicates the reactions need energy input. Solar water splitting uses solar light as the energy input. There are three approaches: photovoltaic electrolysis (PV), photoelectrolysis (PE), and photocatalysis (PC). PV connects an electrolyzer to a solar cell and the electrolyzer is totally powered by the solar cell. The "solar-to-hydrogen" (STH) efficiency of it can exceed 10%. PE uses photocatalytic electrodes and is partially powered by electrical energy, such as a photovoltaic element. The STH efficiency can reach 2 to 3%. It is believed to be a cheaper solution than PV for

H_2 production. PC uses light-irradiated catalysts, typically suspended in water in the form of powders, and it is the simplest approach.[8]

Both electricity-driven and photo-driven water-splitting processes are limited by the slow kinetics of the oxygen evolution half reaction. The oxygen evolution involves four electrons and requires a large overpotential. Moreover, the side reaction of H_2O_2 formation, a kinetically competing two-electron reaction, often poisons or degrades the photocatalysts, so developing a good oxygen evolution catalyst is very important.[8] Currently, the fastest catalytic system is still the oxygen evolution center in photosystem II of the living plant. Its turnover numbers (TON) achieve 180,000 molecules of O_2 per site and turnover frequencies (TOF) of 100-400 s^{-1}. The active site of photosystem II is a $CaMn_4O_5(H_2O)_4$ cluster, but the mechanism of how it works is still not entirely understood.[22]

1.3.2 Nickel-based Anodic Electrocatalysts for Solar Water Splitting

A lot of oxides have been studied as oxygen evolution catalysts. In 1980, Trasatti related the activities of the oxides with their enthalpies of a lower to higher oxide transition and a "volcano" plot was thus made. In this "volcano" plot, IrO_2 and RuO_2 are predicted to be the most active oxygen evolution catalysts.[23] Many studies of oxygen evolution are based on IrO_2 and RuO_2,[7,24] but as mentioned in section 1.2.2, iridium and ruthenium are expensive and rare. The long term stability of IrO_2 and RuO_2 in alkaline media are also poor, so their widespread commercial utilization is impractical and not economical.[25]

Researchers have tested many different metal oxide catalysts in alkaline media.[26-28]

McCrory et al. tested IrO_2, RuO_2, and a series non-noble metal oxides, for example, CoO_x, NiO_x, $CoFeO_x$, $NiFeO_x$, $NiCoO_x$, NiCr, and so on. They found that most of these catalysts can achieve 10 $mA \cdot cm^{-2}$ current density at overpotentials of ~0.33-0.5 V (IrO_2 0.34 V ± 0.01 V, RuO_2 0.29 V ± 0.03 V) and most of the non-noble metal oxides show comparable or better specific activity (output current density normalized by electrochemically active surface area) when compared to IrO_2 and RuO_2. Boettcher et al. prepared thin films of MnO_x, FeO_x, IrO_2, CoO_x, $Ni_{0.25}Co_{0.75}O_x$, $Ni_{0.5}Co_{0.5}O_x$, $Ni_{0.75}Co_{0.25}O_x$, NiO_x, and $Ni_{0.9}Fe_{0.1}O_x$ to avoid the many corrections, such as electrochemically active surface area, mass transport, electrocatalyst conductivity, and so on. Their results indicate that NiO_x and $Ni_{0.9}Fe_{0.1}O_x$ are better oxygen evolution catalysts than IrO_2 in terms of both overpotential and output current density. Besides the high activity, nickel-based electrocatalysts also have long-term physical and chemical stability and their cost is commercially viable. Therefore, nickel-based anodic electrocatalysts should be strong catalyst candidates for solar water oxidation. The catalytically active species is thought to be NiOOH as well.[25]

1.4 Characterization Techniques Background

In this dissertation, surface characterization techniques, electrochemical characterization techniques, and other characterization techniques are used to study the nickel-based catalysts. A brief introduction to the three most used techniques is given here.

1.4.1 X-ray Photoelectron Spectroscopy (XPS)

XPS is a technique that provides information on chemical composition and chemical bonding states of a surface by measuring the binding energy (E_{be}) of elements' core level electrons. It is based on the photoelectric effect. The X-ray flux (Mg $K_{\alpha 1,2}$, 1253.6 eV or Al $K_{\alpha 1,2}$, 1486.6 eV) hits the surface of the sample and an electron with a binding energy E_{be} absorbs a photon of the X-ray flux (E_i) and leaves the surface with kinetic energy E_{kin}. The detector records E_{kin} and thus E_{be} can be calculated through

$$E_{be} = E_i - E_{kin} - \Phi, \tag{1.9}$$

where Φ is the work function of the material and $\Phi = E_{vacuum} - E_{Fermi}$.[29] When E_i is around 1400 eV, most ejected electrons detected are from depths within 10 nm, so XPS is a surface characterization technique. With a sputtering process, depth profiles of up to 100 nm can be obtained.[30]

The electron counts versus binding energy are plotted as an XPS spectrum. An XPS spectrum might contain a continuous background of inelastic secondary electrons, Auger peaks, peaks due to plasmon losses, and the core level electrons. The photoelectric cross-section of the shallow valence band levels is very low, so the valence band features in the XPS are very week. XPS compares the peaks of the core level electrons to obtain the information of the surface. The peak locations are defined by the electron binding energies and they are essential characteristics of certain atomic species. Moreover, chemical states of an element (i.e., chemical components) can also be identified by the chemical shifts, typically in a range from 1 to 10 eV. The binding energy of an electron at

a given level is determined by the Coulomb attraction between the electron and the nucleus and the screening of this attraction by other electrons in the atom. When the atom forms a chemical bond, a chemical shift of binding energy shows up, because the electron transfer leads to a charge density change on the atom. If the charge density increases, the binding energy will decrease because of the enhanced electron screening. Conversely, the peak will shift to a higher binding energy when the charge density decreases. By comparing the experimental peaks with the tabulated binding energies of electrons in elements, atomic species and their chemical bonding states can be identified.[29]

In real applications, usually a survey spectrum covering the whole binding energy range is first taken to identify which elements are in the sample. High-resolution spectra of individual elements that are of interest are then acquired to analyze the chemical bonding states of the element. Physisorbed carbon 1s peak at 284.8 eV can be used as an internal standard to correct other peak positions so that peak positions can be compared from sample to sample. XPS can also be used to do quantitative analysis, including atomic ratio and chemical component ratio. The number of electrons recorded for a given transition is proportional to the number of the component at the surface.[30]

1.4.2 Cyclic Voltammetry (CV)

In this dissertation, a three-electrode configuration was applied throughout all electrochemical techniques. Three electrodes were connected to a potentiostat which tests the electrochemical behavior. The working electrode is the anode, which is modified with the nickel-based catalysts. A reference electrode is connected to the working electrode so that the potential on the working electrode can be correctly applied and monitored. A

counter electrode works as the cathode. The electrons result from fuel and/or water oxidation at the anode and pass through the potentiostat to the cathode, reducing the solvent or other components in the solution so that a circuit is completed.

CV is a technique that monitors the electron transfer process on the working electrode surfaces by measuring the current while sweeping the electrode potential from E_1 to E_2 and then back to E_1 at a certain scan rate. An example of cyclic potential sweep and the corresponding simulated cyclic voltammogram are shown in Figure 1.2A and B. The simulated reaction is

$$A + e \rightleftharpoons B \qquad (1.10)$$

The initial concentration is set to be A at 1 M and B at 0 M. The cathodic scan starts from 0.4 V to -0.4 V. At first there is only nonfaradaic current that comes from the iR drop of the solution and the charging effect due to the capacitance of the electrode surfaces. As the potential scans close to the reduction potential of A, the reduction begins and the faradaic current starts to flow. The reduction consumes A at the electrode surfaces, so the A in the bulk solution diffuses to the electrode surfaces to compensate for the surface concentration decrease. This mass transport forms a concentration gradient from the bulk solution to the electrode surfaces. At E_{pc}, the concentration of A at the electrode surfaces drops to nearly zero and the mass transport reaches its maximum rate, so the reduction current cannot increase anymore, that is, it reaches its maximum. After E_{pc}, the potential is still becoming more negative to consume A, but at the same time the gradient is relaxing due to diffusion, therefore the surface concentration of A is further decreased

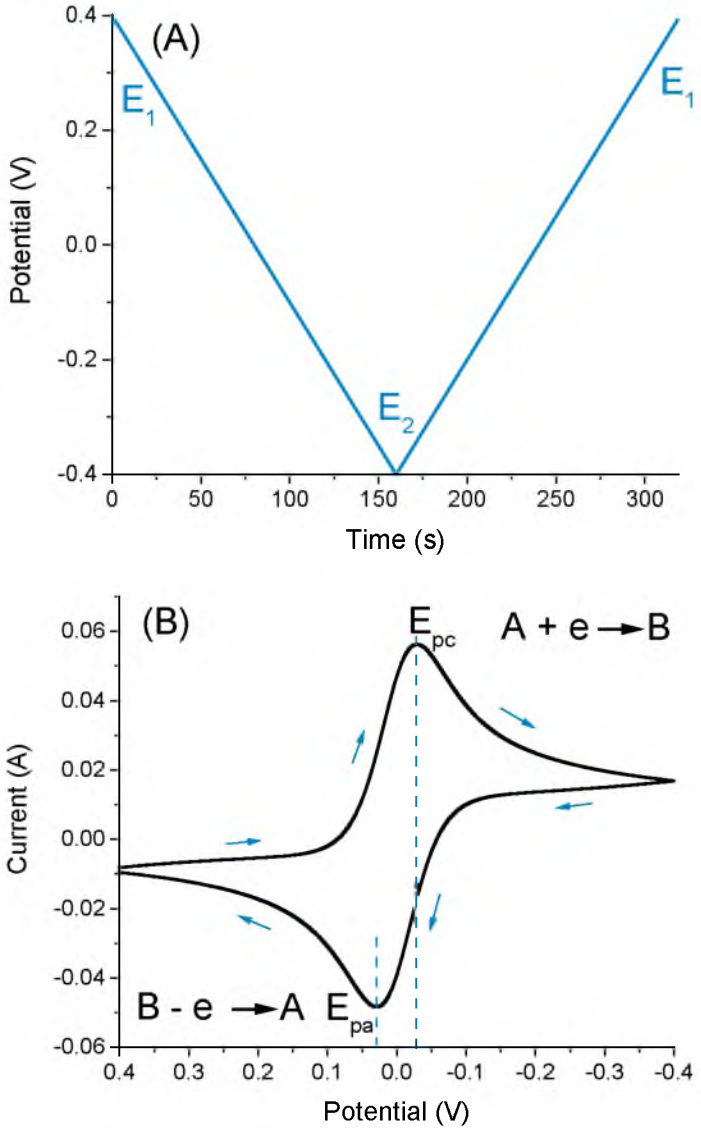

Figure 1.2. Simulated cyclic voltammetry process. (A). Cyclic potential scan. (B). Resulting cyclic voltammogram.

and the current also decreases correspondingly. In the reverse anodic scan from -0.4 V to 0.4 V, a significant amount of B near the electrode surface formed by the cathodic scan gets oxidized, a reverse current flows and reaches the maximum at E_{pa}. The shape of the anodic peak is much like that of the cathodic peak when the reaction is reversible.[31,32] The Randles-Sevcik equation can be applied to the reversible process at a planar electrode:

$$I_p = 2.69 \times 10^5 n^{3/2} A D^{1/2} v^{1/2} C \quad (1.11)$$

where I_p is the peak current, n is the number of the electrons transferred during the redox process, A is the geometric area of the electrode, v is the scan rate, and C is the bulk concentration of electroactive species. C, n, and D can be calculated if other parameters are known. Furthermore, the separation (ΔEp) between E_{pc} and E_{pa} is 0.059/n V, when the reaction is reversible.[33]

1.4.3 Chronoamperometry (CA)

CA is a technique that probes the oxidation of substrate with high sensitivity and is mostly applied in the construction of sensors. A constant potential is applied to the working electrode and the current is recorded as a function of time. In this dissertation, all of the CA experiments were performed while stirring the solution. The potential is usually chosen at around the peak potential in the CV of the system. Typically, at first the potential is applied when there is only the supporting electrolyte and the current is recorded as the background current. A small volume of the substrate is then added to the

electrolyte at certain time intervals, and the current is thus increased as the concentration of the substrate increases until the electrode surface gets saturated. After subtracting the background current, the current can be plotted versus the concentration of the substrate, which is the calibration curve of this substrate and can be used to study the kinetics of this electrochemical reaction and probe this substrate in the future.[33]

1.5 Summary

This chapter elucidates why the study of fuel cells and solar water splitting are important and why nickel-based catalysts in alkaline media were studied to catalyze anodic reactions in alcohol fuel cells and water splitting, that is, alcohol oxidation and oxygen evolution (water oxidation). The following chapters will study the mechanisms and applications of nickel-based anodic electrocatalysts for alcohol oxidation and oxygen evolution. Chapter 2 synthesizes nickel complex nanoparticles on electrode surfaces to increase the electrochemically active surface area and thus enhance the current output. Chapter 3 tests the ability of nickel-based electrocatalysts to oxidize complex fuels, and uses DNA as a polymer scaffold to load nickel hydroxides and thus change the methanol oxidation pathway (compared to nickel hydroxides without DNA scaffold). Chapter 4 demonstrates nickel-based catalysts are more efficient as oxygen evolution catalysts than methanol oxidation catalysts, by investigating the turnover frequency of the two reactions in alkaline media. Chapter 5 proposes a design to apply nickel oxides to a semiconductor that is incorporated with surface-plasmonic metal electrodes to do solar water oxidation with visible light.

1.6 References

(1) Du, P.; Eisenberg, R. *Energy Environ. Sci.* **2012**, *5*, 6012.

(2) Turner, J. A. *Science* **1999**, *285*, 687.

(3) Chiang, L.; Herasymchuk, K.; Thomas, F.; Storr, T. *Inorg. Chem.* **2015**, *54*, 5970.

(4) Walter, M. G.; Warren, E. L.; McKone, J. R.; Boettcher, S. W.; Mi, Q.; Santori, E. A.; Lewis, N. S. *Chem. Rev.* **2010**, *110*, 6446.

(5) Osterloh, F. E. *Chem. Soc. Rev.***2013**, *42*, 2294.

(6) Tachibana, Y.; Vayssieres, L.; Durrant, J. R. *Nat. Photonics* **2012**, *6*, 511.

(7) Eisenberg, R. *Science* **2009**, *324*, 44.

(8) Liu, J.; Liu, Y.; Liu, N.; Han, Y.; Zhang, X.; Huang, H.; Lifshitz, Y.; Lee, S.-T.; Zhong, J.; Kang, Z. *Science* **2015**, *347*, 970.

(9) Office of Energy Efficiency & Renewable Energy, Department of Energy: http://energy.gov/eere/fuelcells/fuel-cells, 2015; Vol. 2015.

(10) Office of Energy Efficiency & Renewable Energy, Department of Energy: http://energy.gov/eere/vehicles/vehicle-technologies-office-advanced-combustion-engines, 2015; Vol. 2015.

(11) Xuan, J.; Leung, M. K. H.; Leung, D. Y. C.; Ni, M. *Renew. Sust. Energ. Rev.* **2009**, *13*, 1301.

(12) Antolini, E.; Gonzalez, E. R. *J. Power Sources* **2010**, *195*, 3431.

(13) Leger, J.-M.; Coutanceau, C.; Lamy, C. In *Fuel Cell Catalysis: A Surface Science Approach*; Koper, M. T. M., Ed.; John Wiley & Sons, Inc.: Hoboken, New Jersey, 2009, p 343.

(14) Scott, K.; Yu, E. In *Electrocatalysis of Direct Methanol Fuel Cells: From Fundamentals to Applications*; Liu, H., Zhang, J., Eds.; Wiley-VCH Verlag GmbH & Co. KGaA: 2009, p 487.

(15) U.S. Geological Survey, Mineral Commodity Summaries 2015: U.S. Geological Survey, 196 p., http://dx.doi.org/10.3133/70140094.; Survey, U. S. G., Ed. 2015.

(16) Fleischmann, M.; Korinek, K.; Pletcher, D. *J. Electroanal. Chem. Interfacial Electrochem.* **1971**, *31*, 39.

(17) Golikand, A. N.; Asgari, M.; Maragheh, M. G.; Shahrokhian, S. *J. Electroanal. Chem.* **2006**, *588*, 155.

(18) Kowala, A.; Portb, S. N.; Nichols, R. J. *Catal. Today* **1997**, *38*, 483.

(19) Trevin, S.; Bedioui, F.; Villegasb, M. G. G.; Bied-Charretonc, C. *J. Mater. Chem.* **1997**, *7*, 923.

(20) Ciszewski, A.; Milczarek, G. *J. Electroanal. Chem.* **1996**, *413*, 137.

(21) Ojani, R.; Raoof, J.; Zavvarmahalleh, S. *Electrochim. Acta* **2008**, *53*, 2402.

(22) Singh, A.; Spiccia, L. *Coord. Chem. Rev.* **2013**, *257*, 2607.

(23) Trasatti, S. *J. Electroanal. Chem. Interfacial Electrochem.* **1980**, *111*, 125.

(24) Hamann, T. W. *Nat. Mater.* **2014**, *13*, 3.

(25) Lyons, M. E. G.; Brandon, M. P. *Int. J. Electrochem. Sci.* **2008**, *3*, 1386.

(26) McCrory, C. C.; Jung, S.; Ferrer, I. M.; Chatman, S. M.; Peters, J. C.; Jaramillo, T. F. *J. Am. Chem. Soc.* **2015**, *137*, 4347.

(27) McCrory, C. C.; Jung, S.; Peters, J. C.; Jaramillo, T. F. *J. Am. Chem. Soc.* **2013**, *135*, 16977.

(28) Trotochaud, L.; Ranney, J. K.; Williams, K. N.; Boettcher, S. W. *J. Am. Chem. Soc.* **2012**, *134*, 17253.

(29) Oura, K.; Lifshits, V. G.; Saranin, A. A.; Zotov, A. V.; Katayama, M. *Surface Science - An Introduction*; First ed.; Springer: New York, United States, 2003.

(30) www.casaxps.com, C. S. L.; Casa Software Ltd. www.casaxps.com: http://www.casaxps.com/help_manual/casaxps2316_manual/xps_spectra.pdf, 2013; Vol. 2016.

(31) Bard, A. J.; Faulkner, L. R. *Electrochemical Methods - Fundamentals and Applications*; Second ed.; John Wiley & Sons, Inc.: United States, 2001.

(32) Pletcher, D.; Greff, R.; Peat, R.; Peter, L. M.; Robinson, J. *Instrumental Methods in Electrochemistry*; Woodhead Publishing Limited: the United Kingdom, 2011.

(33) Hart, J. P. *Electroanalysis of Biologically Important Compounds*; Ellis Horwood Limited: England, 1990.

CHAPTER 2

NICKEL CYSTEINE COMPLEXES AS ANODIC ELECTROCATALYSTS FOR FUEL CELLS

Compared to platinum, nickel is an inexpensive catalyst that can oxidize methanol in alkaline media. There is a desire to increase nickel loading during electrodeposition for improved performance. In this chapter, a nickel cysteine complex (NiCys) is used as the precursor for electrodeposition on glassy carbon electrode surfaces. After optimization of cysteine concentration, the surface concentration of NiOOH on NiCys electrodes characterized by cyclic voltammetry in 0.1 M NaOH can reach 1.28 (± 0.32)×10^{-7} mol/cm^2. The large amount of NiOOH on NiCys electrodes provide 5 times the methanol oxidation current compared to Ni electrodes prepared without cysteine, as demonstrated by chronoamperometry at 0.7 V versus Hg/HgO. Atomic force microscopy (AFM), X-ray photoelectron spectroscopy (XPS), and attenuated total reflection Fourier transform infrared (ATR-FTIR) spectroscopy have been applied to examine surface morphologies and structures of NiCys and Ni electrodes. The analysis reveals that cysteine adjusts the solubility of $Ni(OH)_2$ in 0.1 M NaOH, so more uniform and smaller size nanoparticles are electrodeposited on electrode surfaces compared to Ni electrodes.

Reproduced from Journal of The Electrochemical Society, 2014, 161 (9), F933-F939. Open access article.

2.1 Introduction

As mentioned in Chapter 1, fuel cells are a promising energy conversion device to convert chemical energy in a fuel to electrical energy. Nickel-based anodic electrocatalysts are cheaper than conventional precious-metal-based catalysts and can oxidize various fuels, for example, alcohols, carbohydrates, amino acids, and alkanes, in alkaline media.[1] Direct methanol fuel cells are attracting more and more interest because methanol has high theoretical energy density and is easy to transport and store. In recent years, there has been extensive research on using nickel-based catalysts to electro-oxidize methanol. Planar nickel electrodes show poor catalytic activities,[2] so some researchers have focused on dispersing nickel centers in three-dimensional structures to increase methanol oxidation current. Based on this concept, many nickel complexes in alkaline solution have been electrodeposited onto glassy carbon electrode surfaces, and the electrochemical properties have been examined.[2-14] Nickel macrocyclic complexes, such as nickel porphyrin, cyclam, annulene, salen, and cyanine, have been studied. These examples show methanol oxidation currents are 5 to 80 times higher than their nickel control electrodes.[5,15] However, none of these studies provide a thorough description of the three-dimensional structure, that is, how nickel centers are dispersed by these nickel complexes. It is also not discussed as to how these nickel complexes relate to NiOOH (the catalytically active species) in chemical structure. Very few papers present surface morphology images.[3,4] Most of these nickel complexes have NiOOH surface concentrations in the range of 10^{-9} to 10^{-8} mol/cm^2. One of the nickel annulene has reached the highest value of 9.7×10^{-8} mol/cm^2.[16]

We noticed that cysteine can dissolve $Ni(OH)_2$ in 0.1 M NaOH, so cysteine should

have a strong interaction with $Ni(OH)_2$. This chapter studies the electrodeposition of nickel cysteine in 0.1 M NaOH with different cysteine concentrations. The NiOOH surface concentration in 0.1 M NaOH was measured for each system, and catalytic activities for methanol oxidation have also been examined. Atomic force microscopy (AFM), X-ray photoelectron spectroscopy (XPS), and attenuated total reflection Fourier transform infrared (ATR-FTIR) spectroscopy have been performed to characterize surface morphologies and chemical structures of the electrodes to reveal how cysteine affects the electrode properties.

2.2 Experimental

2.2.1 Reagents

L-cysteine and nickel (II) chloride (anhydrous, powder, 99.99% trace metals basis) were purchased from Sigma-Aldrich. Five weight percent AS-4 solution was supplied by Tokuyama Corporation. The ion-exchange capacity of this resin is 1.4 mmol/g. Reagent-grade methanol was purchased from Fisher Scientific. All solutions were made with ultrapure water (Milli-Q system, 18.2 MΩ•cm) and degassed by nitrogen purging.

2.2.2 Apparatus

2.2.2.1 Electrochemical Setups

The electrochemical experiments were performed with a three-electrode configuration. A Hg/HgO (1M NaOH) electrode was used as the reference electrode and a platinum mesh electrode was used as the counter electrode. The working electrode was a glassy carbon disc electrode (CH Instruments: diameter of 3 mm). Prior to electrode

modification, the glassy carbon electrode was soaked in a saturated EDTA solution and stirred overnight to remove nickel residues from previous experiments and then polished with 1μm and 0.05μm alumina polish media successively, followed by sonication in ultrapure water and ethanol. Cyclic voltammetry (CV) was performed with a Biologic SP-150 Potentiostat/Galvanostat. Chronoamperometry was carried out with CH Instruments 611C potentiostat.

2.2.2.2 Surfaces Characterization

Modified electrode surfaces were characterized by atomic force microscopy (Bruker Dimension Icon-PT atomic force microscope with Peak Force Tapping mode), X-ray photoelectron spectroscopy (Kratos Axis Ultra DLD), and attenuated total reflection Fourier transform infrared spectroscopy (Nicolet iS50). The silicon nitride lever of AFM has a single cantilever with force constant k=0.4 N/m, resonant frequencies f_0=50-90 kHz, radius of curvature of 2 nm. Images were taken with 1 μm size (512 samples/line) at room temperature and analyzed with Nanoscope Analysis software version 1.20. First-order flattening was applied to the images. In the XPS experiments, the base chamber pressure was 3×10^{-10} torr. The X-ray source was monochromatized Al K_α radiation (hν = 1486.6 eV) at 180 W; the survey and high-resolution spectra (O 1s, C 1s, N 1s, S 2p, Ni 2p) were acquired with pass energies of 160 and 40 eV, respectively. Spectra were analyzed with CasaXPS software. The binding energy was corrected with physisorbed C 1s at 284.8 eV. Shirley-type background was subtracted in the spectra. Each ATR-FTIR spectrum took 64 scans and the resolution was 4 cm^{-1}, resulting in a data spacing of 1.928cm^{-1}.

2.2.3 Electrode Preparation

Nickel loading dependency on cysteine concentration was studied in this work. In the precursor, Ni^{2+} ($NiCl_2$) concentration was held at 0.01 M and cysteine concentrations were varied from 0.005 M to 0.06 M. The control was studied with 0.01 M $NiCl_2$. The nickel cysteine solutions were stirred for 3.5 hours prior to using to ensure complex formation. $NiCl_2$ solution or 5 μL nickel cysteine complex (with different nickel cysteine ratios) solution was drop-casted onto glassy carbon electrode surfaces. After the solution was dry, 3.54 μL of AS-4 (an ionomer that promotes OH^- exchange) solution was drop-casted on top of it and allowed to dry overnight. Nickel-based catalysts were evaluated by cyclic voltammetry (CV) in 0.1 M NaOH for 30 cycles from 0 V to 0.9 V versus Hg/HgO at a scan rate of 50 mV/s. Electrodes were then tested in 0.1 M NaOH with 0.1 M methanol with CVs for 30 cycles as well. For surface characterizations, glassy carbon plates instead of glassy carbon electrodes were used and AS-4 solution was not applied during preparation.

2.2.4 Chronoamperometry

Chronoamperometry with methanol concentration from 0 to 1 M was performed in 0.1 M NaOH at 0.7 V versus Hg/HgO while stirring at a constant, controlled rate. In each experiment, the charging current was allowed to dissipate for >1000 s, and for each methanol concentration, there were at least 300 seconds between injections to make sure steady-state current was reached.

2.3 Results and Discussion

2.3.1 Cysteine Effects on Nickel Catalyst Deposition

Nickel-based catalysts were deposited onto AS-4 coated glassy carbon electrode surfaces by cyclic voltammetry in 0.1 M NaOH for 30 cycles. According to literature[17,18], C-O-Ni oxo bridges are formed during this process, so that the catalysts are attached to the electrode surfaces and the pair of redox peaks in the CVs are the $Ni(OH)_2$ and NiOOH peaks. The redox reaction of Ni could be expressed in a simple way as

$$Ni(OH)_2 + OH^- \leftrightarrow NiOOH + H_2O + e^- \quad (2.1)$$

or

$$Ni(OH)_2 \leftrightarrow NiOOH + H^+ + e^- \quad (2.2)$$

Many electrochemical quartz microbalance characterizations of $Ni(OH)_2$ thin film have been done to justify whether this process is based on H^+ transport or OH^- transport, and to discern how many H_2O and other ions are involved in this process,[19] but these are not our focus. Our focus is on the production of the electrocatalytic active species NiOOH and its surface concentration Γ. The current increase after 0.7 V in the CVs is from oxygen evolution: [16]

$$4NiOOH \rightarrow 4NiO + 4\ {}^{\bullet}OH \rightarrow 4NiO + O_2 + 2H_2O \quad (2.3)$$

Without cysteine (Figure 2.1A), the NiOOH peak current does not increase from cycle 2 to cycle 30. With cysteine present (Figure 2.1B), the first cycle shows a peak

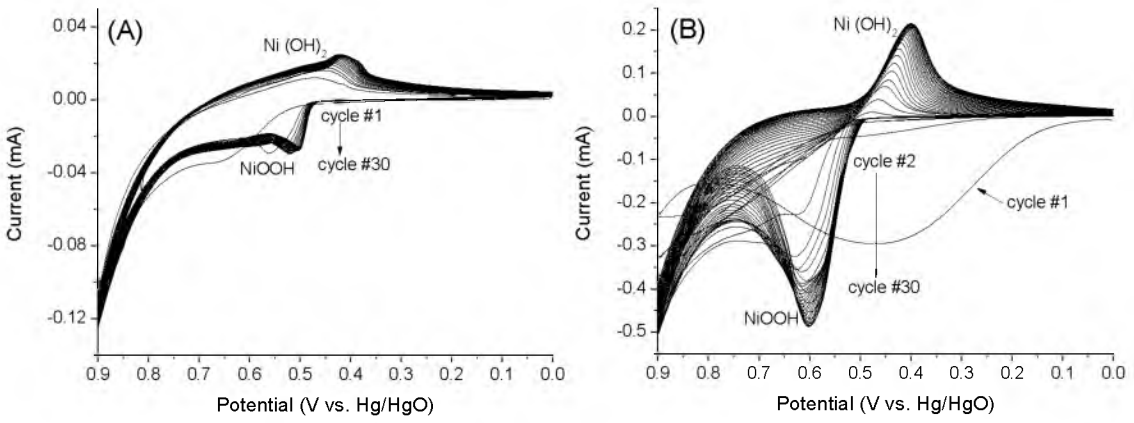

Figure 2.1. Nickel catalyst deposition: representative cyclic voltammograms of Ni and NiCys AS-4 electrodes in 0.1 M NaOH. Scan rate 50 mV/s, 30 cycles. (A) 0.01 M $NiCl_2$ precursor. (B) 0.01 M $NiCl_2$ and 0.05 M cysteine precursor.

around 0.45 V, resulting from cysteine oxidation.[20] After irreversible cysteine oxidation in the first one or two cycles (depending on the amount of cysteine), nickel peaks are observed, which increase as the cycle number increase. We scanned 30 cycles in order to have stable peak currents.

The 30th cycle of Ni and NiCys deposition in 0.1 M NaOH are shown in Figure 2.2A. When cysteine concentration increases, NiOOH peak current also increases, indicating more Ni centers on the electrode surfaces are accessible by OH^-. NiOOH surface concentration Γ is calculated by Equation (2.4): [4]

$$\Gamma = \frac{Q}{nFA} \tag{2.4}$$

where F is Faraday's constant, A is the geometric surface area of the glassy carbon electrodes, and n is the number of electrons transferred during $Ni(OH)_2$ to NiOOH, which is assumed to be 1. Q is the charge under the NiOOH peak and the baseline is chosen as shown in Figure 2.2B. By this method, the charge resulting from side reactions, such as oxygen evolution, can be subtracted. The oxygen evolution reaction starts around 0.7 V in the anodic scan. This makes the NiOOH peak asymmetric, because the current produced by oxygen evolution reaction is also included in the NiOOH peak. By assuming the oxygen evolution reaction happens at the same rate in anodic and cathodic scan, the current curve from cathodic scan can be moved down to the anodic scan to be the baseline of NiOOH peak to rule out the charge from the oxygen evolution reaction. The number of electrons produced by cysteine oxidation is also converted by Equation 2.4, assuming n=1, so that the relationship between NiOOH amount and cysteine oxidation

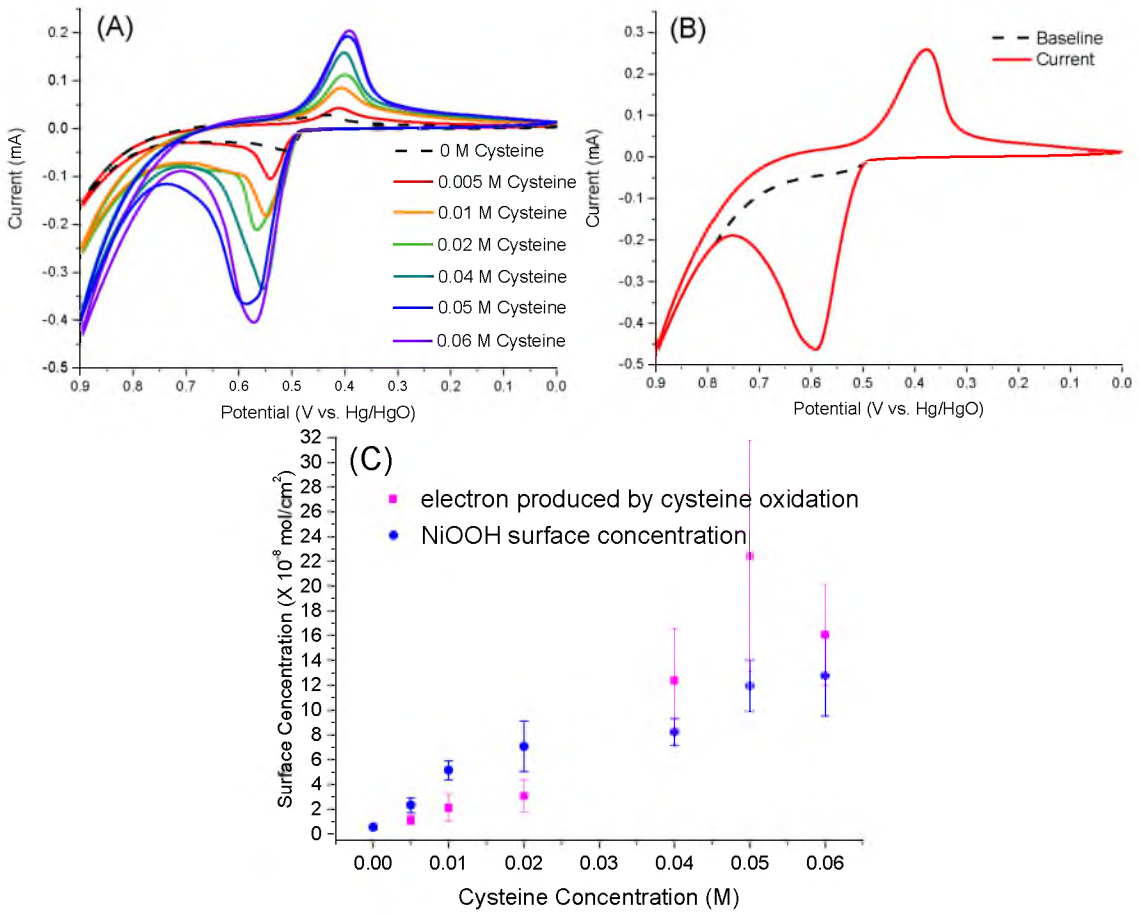

Figure 2.2. Nickel catalysts deposition: (A) Representative 30th cycle of cyclic voltammograms from scanning Ni and NiCys AS-4 electrodes in 0.1 M NaOH. Scan rate 50 mV/s. Cysteine concentration increased from 0 M to 0.06 M and $NiCl_2$ concentration was kept at 0.01 M. (B) Representative 30th cycle of cyclic voltammograms from scanning Ni1Cys6 AS-4 electrodes in 0.1 M NaOH. Scan rate 50 mV/s. The black dash line represents the baseline created by moving the curve from cathodic scan to the anodic scan in the potential range of NiOOH peak. (C) Electrons produced by cysteine oxidation and NiOOH surface concentration versus cysteine concentration. In this plot the number of electrons produced by cysteine oxidation is converted by equation (3), assuming n=1, so it has the same unit as the NiOOH surface concentration.

can be revealed. The results are plotted in Figure 2.2 C. Both the amount of NiOOH and the amount of oxidized cysteine increase as initial cysteine concentration increases, but they follow different trends. In Figure 2.2C, the surface concentrations of cysteine oxidation are below NiOOH when cysteine concentration is lower than 0.02 M, while when cysteine concentration is above 0.04 M, the case is the opposite. There could be some transition between 0.02 M and 0.04 M cysteine. The significance of this work is the NiOOH amount reaches 12.8 (± 3.2) × 10^{-8} mol/cm^2 when cysteine concentration is 0.06 M. To our knowledge, the previously reported highest NiOOH amount on glassy carbon electrode prepared by nickel complexes is 9.7×10^{-8} mol/cm^2,[16] so our NiCys AS-4 electrodes have achieved comparable nickel loading to the highest reported one.

2.3.2 Possible Structures of Electrodeposited Ni and NiCys Catalysts

2.3.2.1 XPS Characterization

Ni (0.01 M $NiCl_2$) and Ni1Cys5 (0.01 M $NiCl_2$ /0.05 M cysteine) modified glassy carbon plates were prepared without the AS-4 polymer layer on glass carbon surfaces and characterized by X-ray photoelectron spectroscopy (XPS). As shown in Figure 2.3, carbon, oxygen, and nickel are detected in the Ni (0.01 M $NiCl_2$) sample, while carbon, oxygen, nitrogen, sulfur, and nickel are detected in the Ni1Cys5 (0.01 M $NiCl_2$ /0.05 M cysteine) sample. The Ni to S ratio is about 1:1 based on the quantitative analysis, suggesting the sample contains equivalent nickel ions and cysteine oxidation product, although in the precursor, the Ni to cysteine ratio is 1:5.

There is no apparent binding energy difference in the two Ni 2p spectra, indicating the oxidation states of Ni in the Ni and Ni1Cys5 samples are the same and fall in the

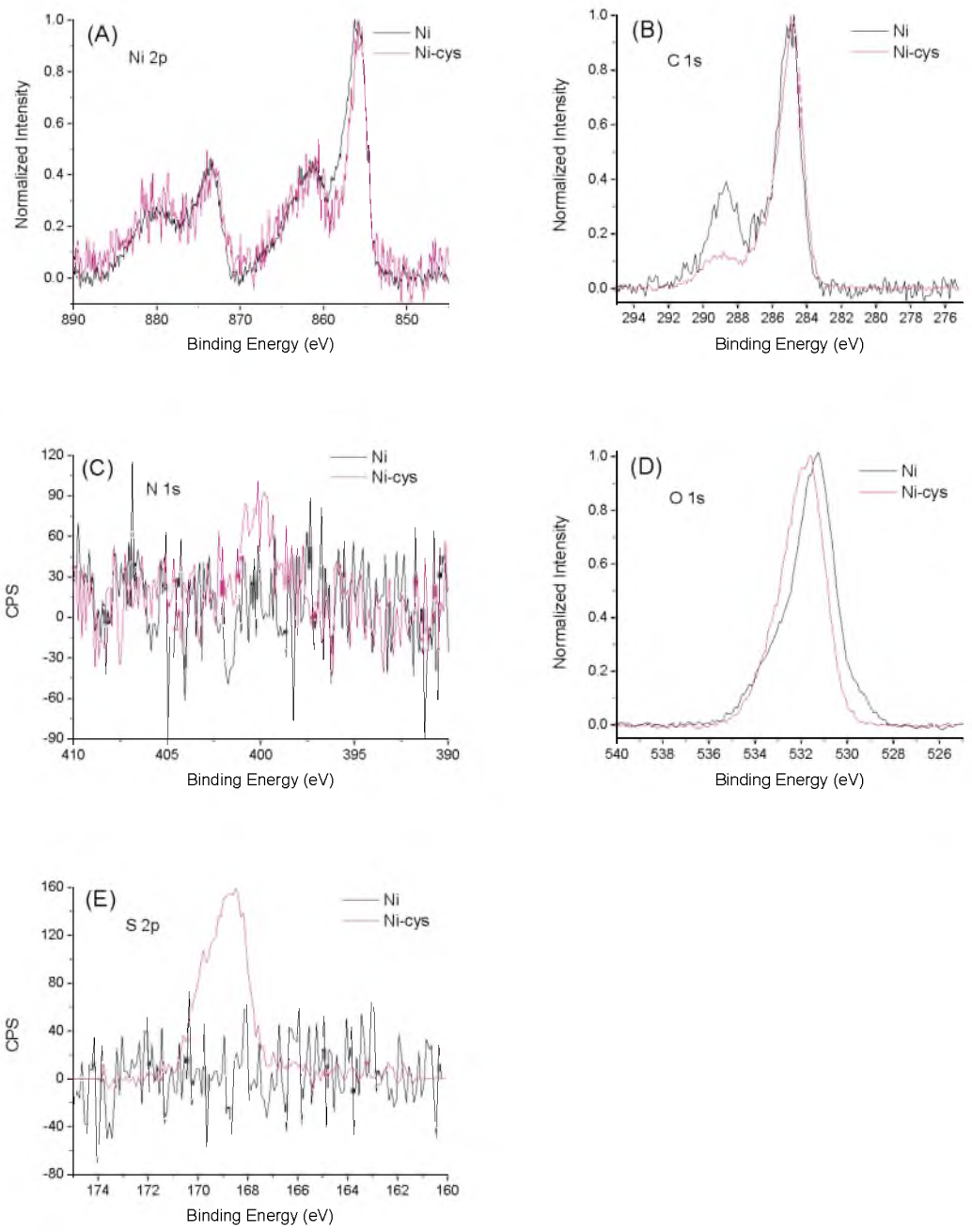

Figure 2.3. XPS spectra (subtracted the Shirley backgrounds, and for easy comparison the peaks' shapes, nickel 2p, carbon 1s, and oxygen 1s peaks were normalized with their own highest peak intensities): (A) Nickel 2p. (B) Carbon 1s. (C) Oxygen 1s. (D) Nitrogen 1s. (E) Sulfur 2p.

binding energy range of NiO, $Ni(OH)_2$, and NiOOH.[21] The peak around 289 eV in the carbon 1s spectrum of the Ni sample suggests some carbon on the glassy carbon plate is oxidized to carboxylate, and/or CO_3^{2-} has contaminated the sample in the alkaline solution during sample preparation.[22] Based on the following ATR-FTIR data, both assignments are possible. The deconvolution components (Table 2.1 and Figure 2.4) of oxygen 1s show both the Ni and Ni1Cys5 sample contain hydroxide, and the Ni sample also contains small amounts of oxide. In literature,[21] the NiO oxygen 1s spectral component is usually found at 529.3 eV, and the binding energy of 531.1 eV is proposed to come from defective sites within the oxide crystal, adsorbed oxygen, or hydroxide. In $Ni(OH)_2$ there would be a single peak with binding energy of 530.9 eV, so component 1 can be the oxygen in NiO and the component 2 can be the oxygen in NiO and $Ni(OH)_2$. The oxygen in $-SO_3^-$ and CO_3^{2-} groups also has binding energy in component 2 range. During the cyclic voltammetry, part of the carbon plate is oxidized. Component 3 and 4 can be assigned to the oxidation products C–O–C (aliphatic), $-COO^-$ and $(-ORC(O)-)_n$ groups. C–O–C is ranged from 532.4 eV to 532.9 eV. In the –COOH group, the carbonyl oxygen usually has binding energy 531.9 eV to 532.5 eV, and the hydroxyl oxygen usually has binding energy 533.2 eV to 533.9 eV, but after –COOH forms $-COO^-$, the two oxygen atoms are almost equivalent and will have binding energy around 532 eV (component 3). If $(-ORC(O)-)_n$ groups also formed in the oxidation, the carbonyl oxygen can be part of the component 3 and the hydroxyl oxygen can be part of the component 4. Component 4 could also come from water molecules bound in the catalysts.[23] In the NiCys sample, there are fewer component 2 and more component 3 compared to the Ni sample, probably because more CO_3^{2-} is in the Ni sample and cysteine contains the

Table 2.1. Deconvolutional components of oxygen 1s XPS spectra

Components	Assignment	Ni sample		Ni-cys sample	
		Binding energy (eV)	Atomic conc. (%)	Binding energy (eV)	Atomic conc. (%)
1	NiO	529.5	5.46		
2	NiO, $Ni(OH)_2$, $-SO_3^-$, CO_3^{2-}	531.3	68.09	531.5	60.32
3	C-O-C, $-COO^-$, $(-ORC(O^*)-)_n$	532.8	18.01	532.5	28.74
4	$(-O^*RC(O)-)_n$, H_2O	534.0	8.43	533.6	10.94

* The oxygen with the "*" is the assigned oxygen.

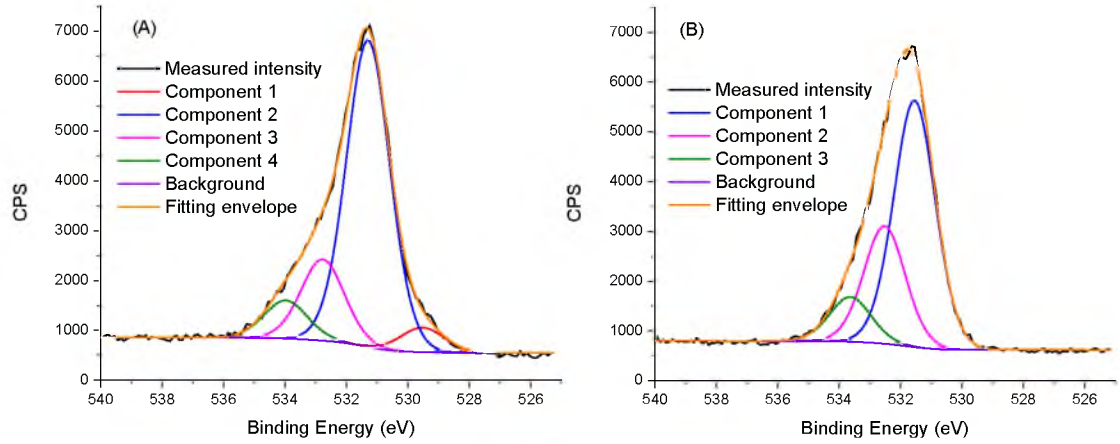

Figure 2.4. Deconvolutional oxygen 1s XPS spectra: (A) Ni sample (FWHM 1.66 eV). (B) Ni-cys sample (FWHM 1.59 eV).

carboxylate group. The binding energy of the N 1s spectrum in the Ni1Cys5 sample fit the profile of $-NH_2$ group.[22,24] The binding energy of sulfur is in the range of S=O group, suggesting sulfur is oxidized.[25] Although researchers have used cysteine and cystamine dihydrochloride to prepare Ni_3S_2, Ni_3S_2 can be ruled out, because its S 2p peaks are located at 161.5 to 162.5 eV.[26,27] To summarize, the Ni sample contains nickel hydroxide and a small amount of nickel oxide, whereas the Ni1Cys5 sample contains nickel hydroxide and the oxidized cysteine product in a ratio of Ni:Cys of 1:1.

2.3.2.2 FTIR Characterization

More structural information can be revealed via ATR-FTIR spectroscopy (Figure 2.5). The samples were prepared on glassy carbon plates without the AS-4 layer. Figure 2.5 shows the FTIR spectra of the bare glassy carbon plate, the electrodeposited Ni sample, and the chemically prepared Ni1Cys5 sample (the electrodeposited Ni1Cys5 sample was too thin to be probed by ATR-FTIR). In the spectra of the Ni and Ni1Cys5 samples, the peak around 466 cm^{-1} is the Ni-O stretching mode. The broad and intense peak around 3200 cm^{-1} can be assigned to O-H stretching mode. These suggest both Ni and Ni1Cys5 samples could have formed a layered nickel hydroxide structure.[28]

In the Ni spectrum, the strong peak around 1359 cm^{-1} could be the stretching mode of CO_3^{2-} groups intercalated between $Ni(OH)_2$ layers. A small amount of $-COO^-$ stretching modes around 1610-1400 cm^{-1} could be buried in the broad 1359 cm^{-1} peak (the peak around 1558 cm^{-1} should be $\nu_{as}(COO^-)$). The peak at 1653 cm^{-1} is the scissoring mode of water. The main peaks of this spectrum are almost identical to the spectrum of electrodeposited CO_3^{2-} intercalated α-$Ni(OH)_2$ reported by M. Figlarz et al.[28]. When

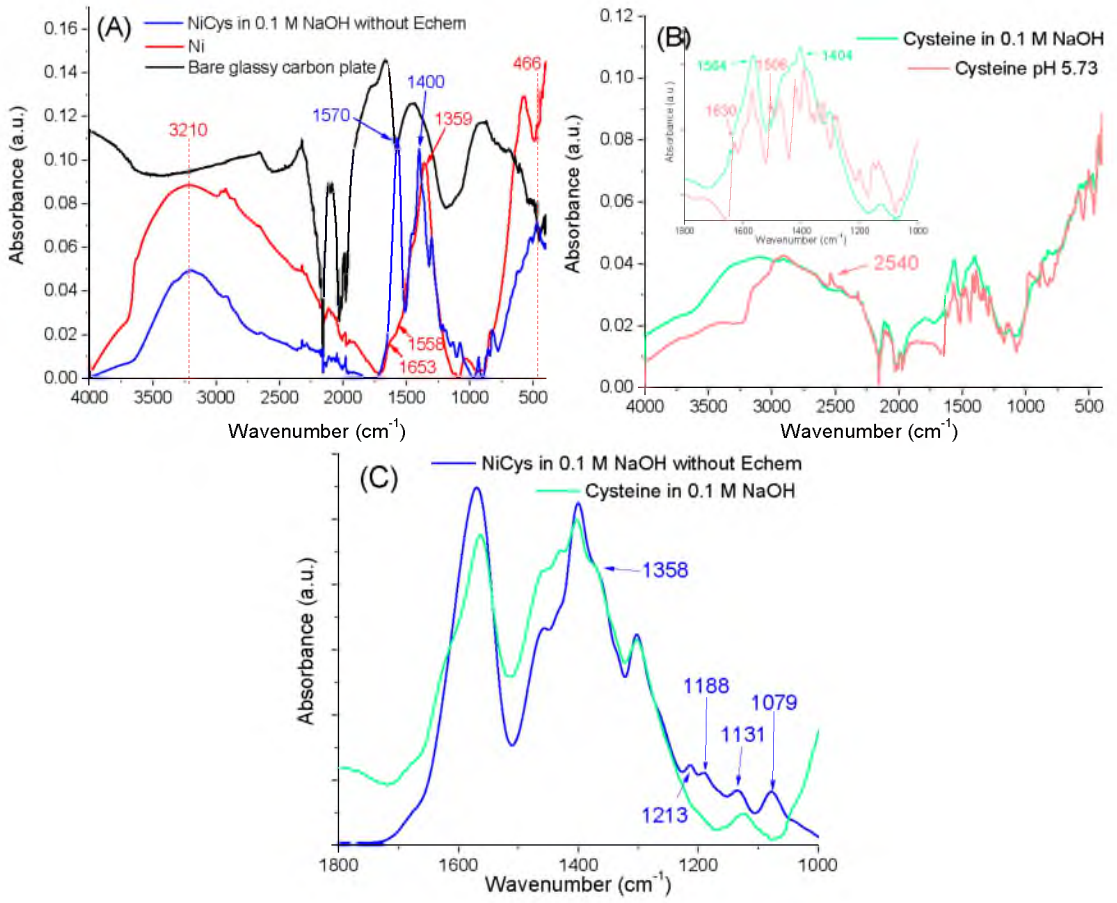

Figure 2.5. FTIR spectra of relevant samples: (A) Bare glassy carbon plate, electrodeposited Ni sample and chemically prepared Ni1Cys5 sample. (B) Chemically prepared cysteine (pH 5.73) and cysteine in 0.1 M NaOH samples. The intercalated spectra also belong to these two samples, but the absorbance intensity has been adjusted in order to compare the peaks in 1000-1800 cm^{-1} range. (C) Chemically prepared cysteine in 0.1 M NaOH and Ni1Cys5 samples. The absorbance intensity has also been adjusted in order to compare the peaks in the 1000-1800 cm^{-1} range.

having cysteine in alkaline media (Figure 2.5B), the –SH stretching at 2540 cm^{-1} in the pH 5.73 cysteine sample has disappeared, suggesting it is deprotonated or oxidized. The 1506 cm^{-1} peak and 1630 cm^{-1} peak in the pH 5.73 cysteine sample are $\delta_s(NH_3^+)$ and $\delta_{as}(NH_3^+)$, respectively. In the alkaline environment, these two peaks disappeared because $-NH_3^+$ is deprotonated. The 1562 cm^{-1} peak and 1400 cm^{-1} peak are $\delta_{as}(COO^-)$ and $\delta_s(COO^-)$, respectively. The NiCys5 sample does not have the –SH stretching peak as well, instead four new peaks show at 1213 cm^{-1}, 1188 cm^{-1}, 1131 cm^{-1} and 1079 cm^{-1} in Figure 2.5C, which are the stretching modes of –S–O and/or –S=O.[29-32] This suggests –SH has been oxidized during sample preparation. Compared to sulfonate ($-SO_3^-$), sulfinate ($-SO_2^-$) usually has peaks at lower frequency, having asymmetrical S=O stretch at 1030 cm^{-1} and a strong symmetrical S=O stretch at 980 cm^{-1},[33,34] so the four new peaks cannot be assigned to sulfonate, but sulfonate. This assignment also matches the XPS results of the electrodeposited Ni1Cys5 sample, which shows sulfur has been oxidized to sulfonate. It can be concluded that cysteine is very easy to oxidize in the presence of Ni ions in an alkaline environment. Compared to cysteine in 0.1 M NaOH sample, the NiCys sample has the $\delta_{as}(COO^-)$ move from 1564 cm^{-1} to 1570 cm^{-1} and $\delta_s(COO^-)$ move from 1404 cm^{-1} to 1400 cm^{-1}, so Ni^{2+} has interacted with the $-COO^-$ group. The shoulder peak at 1358 cm^{-1} in both samples indicates the existence of CO_3^{2-} groups. The oxidized structure is shown in Figure 2.6. Based on the structure in Figure 2.6 and the information from FTIR, Ni ions probably coordinate to the $-COO^-$ and $-SO_3^-$ groups.

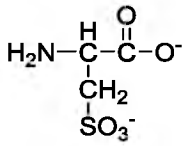

Figure 2.6. The possible structure of oxidized cysteine in the Ni1Cys5 sample.

2.3.2.3 Possible Structures of Electrodeposited Ni and NiCys Catalysts

Bode's representation of nickel oxyhydroxides and nickel hydroxides[35] has well represented the different phases of $Ni(OH)_2$ and NiOOH. All of these nickel hydroxides and oxyhydroxides have layered structures, and the distance (*d*) between two adjacent layers in α-$Ni(OH)_2$, γ-NiOOH, β-$Ni(OH)_2$, and β-NiOOH are 8.0 Å, 6.9 Å, 4.6 Å, and 4.84 Å, respectively. Normally, the charge and discharge conversion happens between α-$Ni(OH)_2$ and γ-NiOOH or between β-$Ni(OH)_2$ and β-NiOOH. If the charge and discharge conversion is between α-$Ni(OH)_2$ and β-NiOOH or between β-$Ni(OH)_2$ and γ-NiOOH, there will be swelling or volume expansion of the nickel film, making the catalyst unstable. Figlarz et al. have studied the species intercalated between chemically precipitated nickel hydroxide layers.[36] They found out their sample is α-$Ni(OH)_2$ and that anions, such as NO_3^- and CO_3^{2-}, as well as water molecules can intercalate between the layers. The formula can be written as $Ni(OH)_{2-x}(A)_y(B)_z \cdot nH_2O$, where A and B can be mono and divalent anions, respectively, and $y + 2z = x$.[28] Larger anions, for example, acetate, succinate, glutarate, and adipate, can intercalate between hydroxide layers, and there is a linear relationship between the intersheet distance (d) and the number of carbon atoms of the carboxylate ions (i.e., the length of the ions).[36] They also studied the difference between electrodeposited and chemically precipitated CO_3^{2-} intercalated $Ni(OH)_2$. It turns out both of them are α-$Ni(OH)_2$ and the intersheet distance of electrodeposited α-$Ni(OH)_2$ (7.6 Å) is slightly smaller than chemical precipitated α-$Ni(OH)_2$ (8.1 Å), probably due to the slightly lower hydration degree.[28] Since electrodeposition and chemical precipitation can lead to similar product structure and the intersheet distance has a dependence on intercalated ion size, our newly prepared Ni

catalyst could also be a CO_3^{2-} intercalated α-$Ni(OH)_2$ with intersheet distance around 7.6 Å, and the Ni1Cys5 catalyst could be a oxidized cysteine intercalated α-$Ni(OH)_2$ with intersheet distance around 11.5 Å (the length of oxidized cysteine is about 6 Å, almost identical to the length of succinate, and the intersheet distance of succinate intercalated α-$Ni(OH)_2$ is about 11.5 Å. The lengths are measured with ChemBio3D Ultra 12.0. Default MM2 job had been run to minimize the energy of the structures, and the lengths are measured between two negatively charged groups at the ends of the structures). Based on the XPS and FTIR data as well as the deduction above, the possible structures of our newly prepared Ni and NiCys samples are shown in Figure 2.7. Because Ni and NiCys samples were prepared at pH 13 and pH 13 is much higher than the pKa of $-NH_2$, $-COO^-$ and $-SO_3^{2-}$ groups, these groups are all deprotonated.

2.3.2.4 The Effects of the Phases of the Nickel Catalysts on Catalytic Performance

The phase of the prepared catalyst is important for its performance. Normally, the charge and discharge conversion happens between α-$Ni(OH)_2$ and γ-NiOOH or between β-$Ni(OH)_2$ and β-NiOOH. γ-NiOOH has many advantages over β-NiOOH for methanol oxidation. The intersheet distance of γ-NiOOH is about 2 Å larger than β-NiOOH and the oxidation state of Ni in γ-NiOOH is 3.67, 0.67 higher than in β-NiOOH.[37] The looser packing of γ-NiOOH than β-NiOOH in agglomerates can provide more porosity, and the higher oxidation state gives higher discharge electrochemical capacity.[38] Oxygen evolution consumes NiOOH that could have been used to catalyze methanol oxidation, and the oxygen bubble formed by oxygen evolution might cause the catalysts to fall from the electrode surfaces. β-NiOOH has been shown to be more active than γ-NiOOH on

Figure 2.7. Possible structures of Ni and NiCys samples, newly prepared by electrodeposition.

oxygen evolution.[37] Moreover, the study of Barnard et al. has shown the formal potential of the α-$Ni(OH)_2$ / γ-NiOOH couple (0.392-0.440 V vs. Hg/HgO/KOH) is lower than the β-$Ni(OH)_2$ / β-NiOOH couple (0.443-0.470 V vs. Hg/HgO/KOH). This also means methanol can be oxidized at lower potential with the α-$Ni(OH)_2$ / γ-NiOOH couple than with the β-$Ni(OH)_2$ / β-NiOOH couple,[39] so preparing stable α-$Ni(OH)_2$ instead of β-$Ni(OH)_2$ will improve catalyst performance and benefit methanol fuel cell applications.

2.3.3 Surface Morphology of the Catalysts

2.3.3.1 AFM Characterizations

Surface morphology of the catalysts was probed by AFM to reveal other differences between Ni and NiCys samples (Figure 2.8). Ni (0.01 M $NiCl_2$), Ni1Cys0.5 (0.01 M $NiCl_2$ /0.005 M cysteine), Ni1Cys2 (0.01 M $NiCl_2$ /0.02 M cysteine) and Ni1Cys5 (0.01 M $NiCl_2$ /0.05 M cysteine) were prepared on glassy carbon (GC) plates without the AS-4 polymer layer coating on the top. The root mean square roughness (R_q) of the samples are 0.577 nm (bare glassy carbon plate), 10.7 ± 2.4 nm (Ni1Cys0.5), 10.0 ± 1.6 nm (Ni1Cys2), 6.8 ± 1.4 nm (Ni1Cys5), 33.5 ± 3.9 nm (Ni with large aggregates, e.g., Figure 2.8E), and 4.5 ± 0.1 nm (Ni with thin layer, e.g., Figure 2.8F).

Section analysis shows both the Ni- and NiCys-modified surfaces have nanoparticles on the surface. The Ni1Cys5 surfaces have these particles distributed quite uniformly, with diameters of 20 – 35 nm and heights of 5 – 20 nm. The Ni surfaces also have these particles, but the surfaces are heterogeneous - the particles either form large aggregates (Figure 2.8 E) with heights over 100 nm or the particles cannot fully cover the surfaces (Figure 2.8 F). The particle size of the Ni1Cys0.5 and Ni1Cys2 surfaces is between the

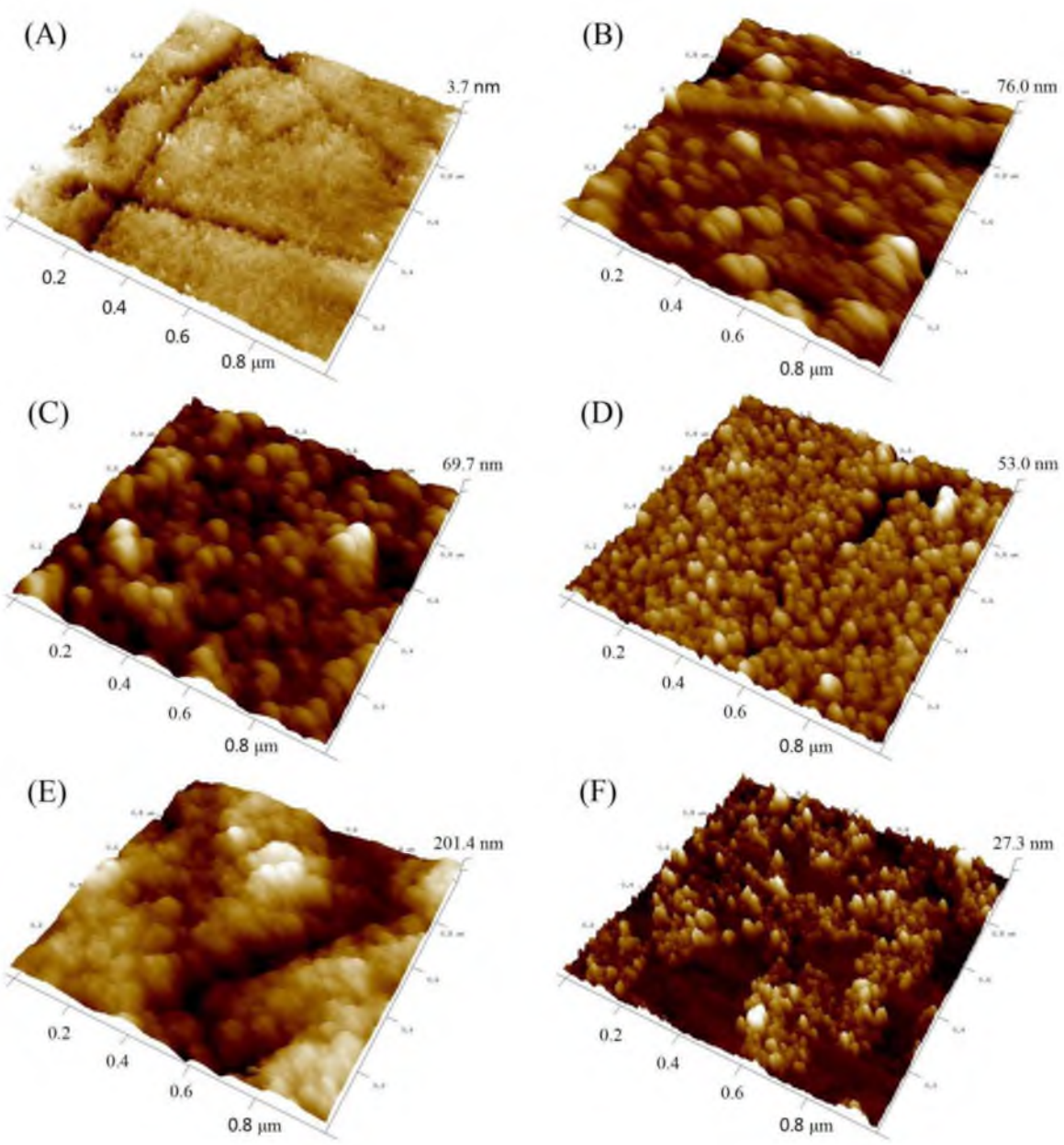

Figure 2.8. AFM 3D height sensor images: (A) Bare glassy carbon plate. (B) Ni1Cys0.5 catalyst deposited with 0.01 M $NiCl_2$ and 0.005 M cysteine precursor. (C) Ni1Cys2 catalyst deposited with 0.01 M $NiCl_2$ and 0.02 M cysteine precursor. (D) Ni1Cys5 catalyst deposited with 0.01 M $NiCl_2$ and 0.05 M cysteine precursor. (E) Ni catalyst deposited with 0.01 M $NiCl_2$ precursor, area with large aggregates. (F) Ni catalyst deposited with 0.01 M $NiCl_2$ precursor, area with small particles.

Ni and Ni1Cys5 surfaces. The majority of the particles are 25 – 40 nm in diameter and 10 – 20 nm in height. Besides, about 25% of the particles found on Ni1Cys0.5 surfaces are 50 – 60 nm in diameter and 20 – 30 nm in height.

The trend is, as the cysteine concentration increases, the heterogeneity of the surface and the particle size decrease. This could be due to the solubility of $Ni(OH)_2$ in 0.1 M NaOH with different cysteine concentrations (Figure 2.9). In 0.1 M NaOH, 0.01 M $NiCl_2$ precipitates to form $Ni(OH)_2$ immediately, and the mixture of 0.01 M $NiCl_2$ and 0.005 M cysteine solution has some $Ni(OH)_2$ precipitates in the bottom, while the remaining Ni^{2+} stays in the solution. Newly prepared mixtures of 0.01 M $NiCl_2$ and 0.02 M cysteine and mixtures of 0.01 M $NiCl_2$ and 0.05 M cysteine stay clear, but after two days, the 0.01 M $NiCl_2$ and 0.02 M cysteine solution has some precipitates while 0.01 M $NiCl_2$ and 0.05 M cysteine solution can stay clear for at least a week, so when there is no cysteine present, OH^- precipitates Ni^{2+} from $NiCl_2$ immediately. Correspondingly, when Ni AS-4 electrodes are prepared by electrodeposition, the NiOOH is all deposited during the first CV, and further scans do not increase the NiOOH peak current, as shown in Figure 2.1A. On the other hand, cysteine can dissolve $Ni(OH)_2$ in alkaline media. The presence of cysteine can probably decrease the nickel precipitation rate to make the deposition more uniform, so the NiOOH peak current of NiCys AS-4 electrodes increases during the first several cycles, in contrast to Ni AS-4 electrodes (Figure 2.1B). Furthermore, as pointed in Figure 2.2C, there could be some transition between 0.02 M and 0.04 M cysteine, such as when cysteine concentration is at or below 0.02 M, cysteine oxidation products only intercalate between $Ni(OH)_2$ layers; but when cysteine concentration is above 0.04 M, there are some cysteine oxidation products adsorbed onto $Ni(OH)_2$ surfaces besides those

Figure 2.9. From left to right: $NiCl_2$, Cysteine, Ni-cysteine (1:0.5) and Ni-cysteine (1:5).

intercalate between $Ni(OH)_2$ layers. So in the case of Ni1Cys5, the large amount of cysteine might partially dissolve the deposited particles, causing the particle size of Ni1Cys5 to be the smallest.

2.3.3.2 A Possible Method to Produce Nanoparticles on Electrode Surfaces

In this chapter, different sizes of nanoparticles are prepared by adding a new equilibrium to the particle growth process. The adding ligand can partially dissolve the nanoparticles so that the nanoparticle nucleation process slows down and the nanoparticle growth process is adjusted. By tuning the concentrations of the ligand, nanoparticles of different sizes can be produced. This method adds a new parameter to control nanoparticle growth. It could be that a universal method can be extended to other nanoparticle preparations.

2.3.3.3 Effects of AS-4 layer

These samples are not covered by the AS-4 layer. According to the results from cyclic voltammetry, Ni1Cys5 samples have about 25% nickel loading (NiOOH surface concentration) compared to Ni samples, both without the AS-4 layer, and 10 times higher nickel loading compared to Ni samples when they are both covered with the AS-4 layer (Figure 2.10). It is probable that when Ni1Cys5 sample is prepared without the AS-4 layer, only the very thin layer closest to glassy carbon surfaces is left. When they are prepared with the AS-4 layer, nickel complexes are less able to leach, so the amount of Ni will be about the same among all Ni and NiCys samples. In this situation, smaller particle size will have higher surface area. This explains why Ni1Cys5 AS-4 electrodes

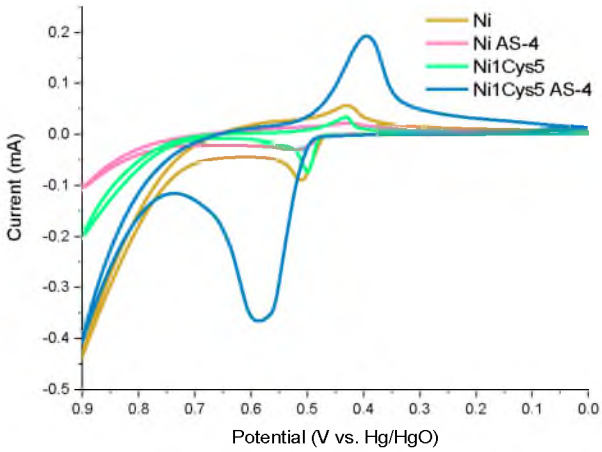

Figure 2.10. Nickel catalysts deposition: The representative 30th cycles of cyclic voltammograms from scanning Ni and NiCys electrodes in 0.1 M NaOH. The calculated (averaged from at least 3 electrodes) NiOOH surface concentrations are Ni: 1.5 (± 0.4) × 10^{-8} mol/cm^2; Ni AS-4: 1.1 (± 0.3) × 10^{-8} mol/cm^2; Ni1Cys5: 0.5 (± 0.2) × 10^{-8} mol/cm^2; Ni1Cys5 AS-4: 11.8(± 2.9) × 10^{-8} mol/cm^2.

have the highest NiOOH surface concentration among these 4 samples. The effect of AS-4 layer on catalyst performance is further discussed in Chapter 4. AFM analysis suggests adding more cysteine in the Ni-cysteine precursor will result in smaller nanoparticles and more homogeneous distribution on the surface. The particle size and surface homogeneity could affect the catalytic efficiency.

2.3.4 Methanol Oxidation by Ni and NiCys Electrodes

2.3.4.1 Methanol Oxidation by Ni and NiCys Electrodes

As shown in Figure 2.11A, the large peak around 0.7 V is the methanol oxidation peak. The reaction is[16]

$$\text{NiOOH} + \text{fuel} \rightarrow \text{Ni(OH)}_2 + \text{oxidation product} \qquad (2.5)$$

Since higher cysteine concentration provides higher NiOOH surface concentration, electrodes with higher cysteine concentration also produce higher methanol oxidation current. This is further investigated by chronoamperometry. Figure 2.11B is a representative example of the amperometric experiments. The arrows represent each methanol injection. After adding methanol, the current increased immediately. At high methanol concentrations, the nickel centers were saturated and the current did not increase further. Figure 2.11C shows the current density (calculated versus the geometric surface area of the glassy carbon electrodes) change with increasing methanol concentration, and the maximum methanol oxidation current is reached at 0.3 M methanol. The methanol oxidation current increases as cysteine concentration in the

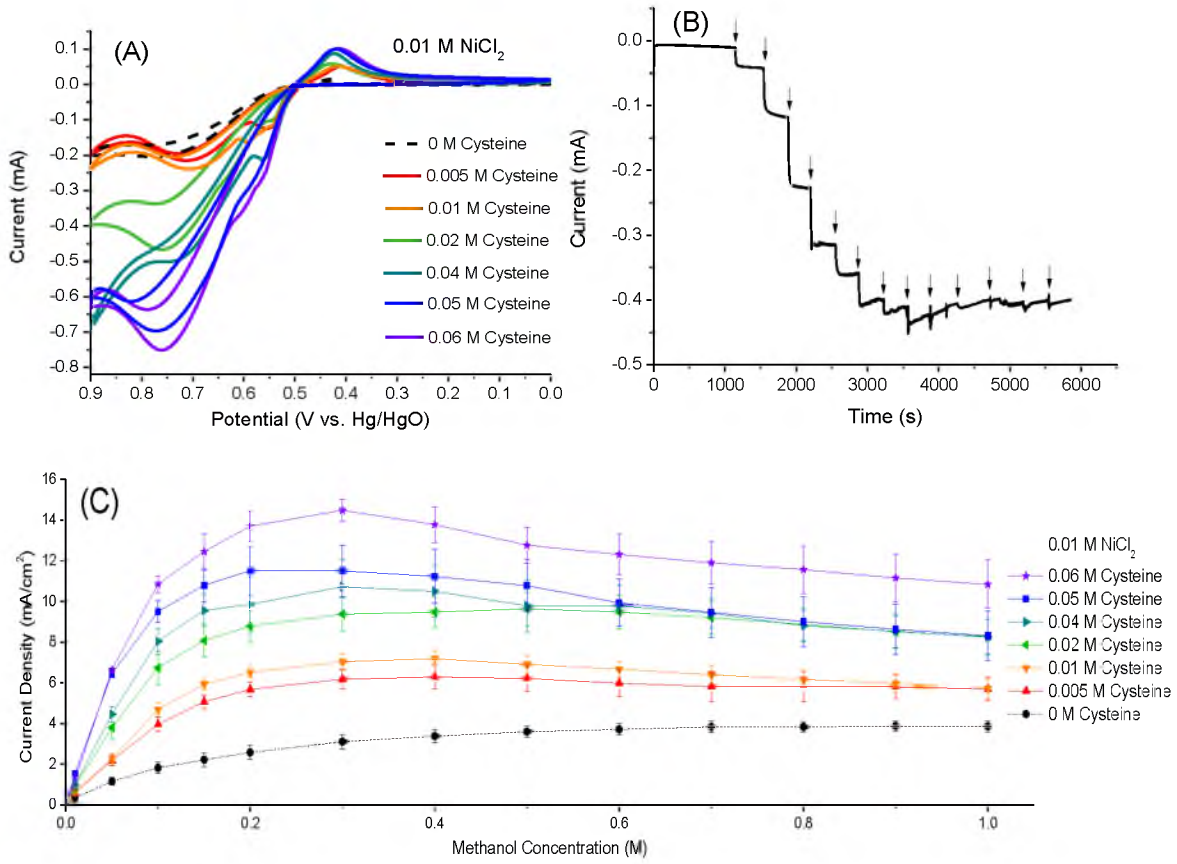

Figure 2.11. (A) Representative cyclic voltammograms of Ni and NiCys AS-4 electrodes in 0.1 M NaOH and 0.1 M methanol, scan rate 50 mV/s. (B) Chronoamperometric response for a Ni1Cys0.5 (0.01 M $NiCl_2$ and 0.005 M Cysteine) AS-4 electrode in 0.1 M NaOH and increasing concentrations of methanol at 0.7 V (vs. Hg/HgO). The methanol concentration ranges from 0 M to 1 M. (C) Calibration curves of methanol oxidation for Ni and NiCys AS-4 electrodes. Data were calculated from chronoamperometry experiments (e.g., Figure 2.11B).

precursor increases due to the increasing NiOOH surface concentration. The current has about 5 times enhancement at 0.3 M methanol when comparing Ni1Cys6 AS-4 to Ni AS-4 electrodes. This shows that the presence of cysteine can enhance the methanol oxidation current. The methanol oxidation current decreases when methanol concentration is higher than 0.3 M with Ni1Cys4, Ni1Cys5 and Ni1Cys6 AS-4 electrodes. This current decrease is probably due to the "poisoning" of the catalysts. Detailed discussion of this phenomenon will be in Chapter 4.

Platinum has been considered as the most promising anodic catalyst candidate among pure metals for application in direct methanol fuel cells.[40] Methanol oxidation starts at the onset of OH^- adsorption on platinum. The study of Tripkovic et al. shows in 0.1 M NaOH OH^- adsorption starts at around 0.45 V (vs. RHE) on platinum-deposited glassy carbon electrodes.[41] Their platinum electrodes have 8 mA/cm^2 current density maximum at about 0.95 V (vs. RHE) with cyclic voltammetry (scan rate 50 mV/s) when oxidizing 0.5 M methanol in 0.1 M NaOH. On the other hand, methanol oxidation with NiOOH initiates after NiOOH is produced. The potential of the onset of NiOOH production is around 0.6 V (vs. RHE), so methanol is oxidized at higher potential on NiOOH than on platinum. The cyclic voltammograms of 0.1 M methanol oxidized in 0.1 M NaOH with Ni1Cys6 AS-4 electrodes show 10.2(±1.7) mA/cm^2 current density maximum at about 0.92(±0.3) V (vs. RHE) with scan rate 50 mV/s. Moreover, if the current production is converted to current per catalyst mass (A/g, using the NiOOH surface concentration to calculate the mass of NiOOH), Ni1Cys6 AS-4 electrodes produce current about 1240 (±320) A/g with 0.3 M methanol in 0.1 M NaOH at 0.82 V (vs. RHE) calculated from chronoamperometry data. Some studies of platinum or platinum ruthenium alloy only have a current range

from 300 A/g to 900 A/g with 1 M methanol in acidic environments,[42] so nickel cysteine complexes are competitive anodic electrocatalysts for methanol fuel cells.

2.4 Conclusion

NiCys AS-4 electrodes have achieved comparable NiOOH surface concentration to the highest reported nickel complexes on glassy carbon electrodes. Compared to Ni AS-4 electrodes, NiCys AS-4 electrodes can enhance methanol oxidation current by 5 times in 0.3 M methanol, because of the high NiOOH surface concentration. The high methanol oxidation current production makes nickel cysteine complexes competitive anodic electrocatalysts for methanol fuel cells. Surface characterization shows that cysteine adjusts the solubility of $Ni(OH)_2$ in 0.1 M NaOH, so more uniform and smaller size nanoparticles are electrodeposited on electrode surfaces. The surface area of the catalysts is enlarged thus more $Ni(OH)_2$ are accessible to OH^- to form NiOOH. This benefits the methanol oxidation process. The method of adding a ligand that can adjusting nanoparticle solubility to produce nanoparticles of different sizes might extend to other nanoparticle synthesis.

2.5 References

(1) Chen, D.; Lee, G. G. W.; Minteer, S. D. *ECS Electrochem. Lett.* **2012**, *2*, F9.

(2) Golikand, A. N.; Asgari, M.; Maragheh, M. G.; Shahrokhian, S. *J. Electroanal. Chem.* **2006**, *588*, 155.

(3) Cataldi, T. R. I.; Desimoni, E.; Ricciardi, G.; Lelj, F. *Electroanalysis* **1995**, *7*, 435.

(4) Golabi, S. M.; Nozad, A. *Electroanalysis* **2004**, *16*, 199.

(5) Revenga-Parra, M.; García, T.; Lorenzo, E.; Pariente, F. *Sens. Actuators B Chem.* **2008**, *130*, 730.

(6) Trevin, S. p.; Bedioui, F.; Villegas, M. G. G.; Bied-Charreton, C. *J. Mater. Chem.* **1997**, *7*, 923.

(7) Ciszewski, A.; Milczarek, G. *J. Electroanal. Chem.* **1996**, *413*, 137.

(8) Cataldi, T. R. I.; Centoze, D.; Ricciardi, G. *Electroanalysis* **1995**, *7*, 312.

(9) Ciszewski, A.; Milczarek, G. *J. Electroanal. Chem.* **1997**, *426*, 125.

(10) Jafarian, M.; Haghighatbin, M. A.; Gobal, F.; Mahjani, M. G.; Rayati, S. *J. Electroanal. Chem.* **2011**, *663*, 14.

(11) Ureta-Zañartu, M. S.; Alarcón, A.; Muñoz, G.; Gutiérrez, C. *Electrochim. Acta* **2007**, *52*, 7857.

(12) Ojani, R.; Raoof, J.-B.; Zavvarmahalleh, S. R. H. *Electrochim. Acta* **2008**, *53*, 2402.

(13) Ciszewski, A.; Stepniak, I. *Electrochim. Acta* **2012**, *76*, 462.

(14) Zheng, L.; Song, J.-f. *J. Solid State Electrochem.* **2010**, *14*, 43.

(15) Taraszewska, J.; Roslonek, G. *J. Electroanal. Chem.* **1994**, *364*, 209.

(16) Casella, I. G.; Cataldi, T. R. I.; Salvi, A. M.; Desimoni, E. *Anal. Chem.* **1993**, *65*, 3143.

(17) Roslonek, G.; Taraszewska, J. *J. Electroanal. Chem.* **1992**, *325*, 285.

(18) Zhou, G.; Wang, D.-W.; Yin, L.-C.; Li, N.; Li, F.; Cheng, H.-M. *ACS Nano* **2012**, *6*, 3214.

(19) Wehrens-Dijksma, M.; Notten, P. H. L. *Electrochim. Acta* **2006**, *51*, 3609.

(20) Jia, D.; Li, F.; Sheng, L.; Ren, Q.; Dong, S.; Xu, S.; Mu, Y.; Miao, Y. *Electrochem. Commun.* **2011**, *13*, 1119.

(21) Biesinger, M. C.; Payne, B. P.; Lau, L. W. M.; Gerson, A.; Smart, R. S. C. *Surf. Interface Anal.* **2009**, *41*, 324.

(22) Naumkin, A. V.; Kraut-Vass, A.; Gaarenstroom, S. W.; Powell, C. J.; the National Institute of Standards and Technology: http://srdata.nist.gov/xps/, 2012; Vol. 2000.

(23) Wang, R.; Kido, M.; Morihiro, N. *Mater. Trans.* **2003**, *44*, 389.

(24) Jermakowicz-Bartkowiak, D.; Kolarz, B. N.; Tylus, W. *Polymer* **2003**, *44*, 5797.

(25) Wang, K.; Hong, L.; Liu, Z.-L. *Ind. Eng. Chem. Res.* **2008**, *47*, 6517.

(26) Zhang, B.; Ye, X.; Dai, W.; Hou, W.; Xie, Y. *Chemistry* **2006**, *12*, 2337.

(27) Falkowski, J. M.; Concannon, N. M.; Yan, B.; Surendranath, Y. *J. Am. Chem. Soc.* **2015**, *137*, 7978.

(28) Portemer, F.; Delahaye-Vidal, A.; Figlarz, M. *J. Electrochem. Soc.* **1992**, *139*, 671.

(29) Padalkar, K. V.; Gaikar, V. G.; Aswal, V. K. *J. Mol. Liq.* **2009**, *144*, 40.

(30) Trujillano, R.; Holgado, M. J.; Rives, V. *Stud. Surf. Sci. Catal.* **2002**, *142*, 1387.

(31) Li, S.; Shen, Y.; Xiao, M.; Liu, D.; Fa, L.; Wu, K. *J. Ind. Eng. Chem.* **2014**, *20*, 1280.

(32) Biswas, S.; Zhang, J.; Li, Z.; Liu, Y. Y.; Grzywa, M.; Sun, L.; Volkmer, D.; Van Der Voort, P. *Dalton Trans.* **2013**, *42*, 4730.

(33) Kerres, J. *Fuel Cells* **2006**, *6*, 251.

(34) Lewis, D.; Mama, J.; Hawkes, J. *Appl. Spectrosc.* **2014**, *68*, 1327.

(35) Bode, H.; Dehmelt, K.; Witte, J. *Electrochim. Acta* **1966**, *11*, 1079.

(36) Genin, P.; Delahaye-Vidal, A.; Portemer, F.; Tekaia-Elhsissen, K.; Figlarz, M. *Eur. J. Solid State Inorg. Chem.* **1991**, *28*, 505.

(37) Yeo, B. S.; Bell, A. T. *J. Phys. Chem. C* **2012**, *116*, 8394.

(38) Ezhov, B. B.; Malandin, O. G. *J. Electrochem. Soc.* **1991**, *138*, 885.

(39) Barnard, R.; Randell, C. F.; Tye, F. L. *J. Appl. Electrochem.* **1980**, *10*, 109.

(40) Chen, A.; Holt-Hindle, P. *Chem. Rev.* **2010**, *110*, 3767.

(41) Tripković, A. V.; Popović, K. D.; Lović, J. D.; Jovanović, V. M.; Kowal, A. *J. Electroanal. Chem.* **2004**, *572*, 119.

(42) Hutton, L. A.; Vidotti, M.; Patel, A. N.; Newton, M. E.; Unwin, P. R.; Macpherson, J. V. *J. Phys. Chem. C* **2011**, *115*, 1649.

CHAPTER 3

FUEL DIVERSITY STUDIES OF NICKEL-BASED CATALYSTS AND METHANOL OXIDATION MECHANISM ALTERATION WITH DNA SCAFFOLDS

In this chapter, the catalytic specificity and degree of oxidation of different fuels with nickel-based catalysts were studied. $NiCl_2$ and DNA-Ni complexes were electrodeposited onto glassy carbon electrode surfaces at 1.8 V vs Ag/AgCl to prepare Ni and DNA-Ni electrodes. These electrodes have shown electrocatalytic activity for oxidation of methanol, ethanol, glycerol, and glucose at room temperature in alkaline (0.1 M NaOH) solutions. Bulk electrolysis products identified by ^{13}C NMR include carbonate in methanol, glycerol, and glucose's oxidation products, suggesting these three fuels can be deeply oxidized and carbon-carbon bonds were broken during the oxidation. The capability of deep oxidation of fuels under relatively moderate conditions makes nickel-based catalysts a candidate for fuel cell applications. Although Ni and DNA-Ni electrodes have very similar activities towards these fuels, DNA-Ni and Ni could oxidize them in different pathways. In alkaline media, methanol can lose two electrons to produce formaldehyde, four electrons to produce formate, or six electrons to produce

carbonate. DNA-Ni electrodes oxidize formaldehyde at about 0.08 V higher than Ni electrodes, with about 1.4 mA/cm^2 higher current output, while oxidizing formate at a lower potential than Ni electrodes. Overall, DNA-Ni electrodes can completely oxidize methanol at a potential about 0.1 V lower than Ni electrodes, which will benefit methanol fuel cell applications. Electrodes modified with small ligand-Ni complexes such as nucleotide-Ni complexes behave similarly to Ni electrodes, so this mechanism change needs a polymer backbone. Atomic force microscopy (AFM) shows that DNA and DNA-Ni aggregates on the electrode surfaces form nanoparticles instead of strands. UV-Vis spectroscopy suggests Ni-ligand coordination and an increased degree of π-π stacking in the DNA structure. X-ray photoelectron spectroscopy (XPS) confirmed that DNA was oxidized during electrodeposition and the electronic structure of Ni ion in DNA-Ni is different from Ni ion in small ligand-Ni, that is, more electron density is transferred from Ni ion to the ligands in DNA-Ni. The three-dimensional (3D) structure of DNA-aggregates should account for the change of the catalytic properties of metal centers. It is possible that other polymer backbones modified with specific ligands can also form microenvironments that can alter the catalytic properties of metal centers by forming this kind of aggregates.

3.1 Introduction

An important feature of fuel cells is their high energy density. To utilize the energy stored in the fuel completely and efficiently, efficient catalysts are needed. Ethanol, glycerol, and glucose are important high-energy-density fuels, along with the more common methanol fuel. Unlike methanol, they are less toxic and can be produced from

agriculture. To completely oxidize these fuels, the carbon-carbon bond needs to be broken, which most precious metal-based catalysts have difficulties doing.[1] In this study, the ability of nickel-based catalysts to oxidize complex fuels is evaluated.

Catalysts are often supported on polymer scaffolds to allow larger surface area and better microenvironment to the catalysts. The selectivity of the reaction products sometimes can also be altered by the scaffolds.[2] The selectivity of the reaction products is important. For example, in alkaline medium, methanol can lose two electrons to produce formaldehyde, four electrons to produce formate, or six electrons to produce carbonate. The oxidation of methanol to formaldehyde is preferred in industry, because formaldehyde is an important precursor in chemical synthesis, but in the direct methanol fuel cell applications, formaldehyde is an unwanted product, because the production of formaldehyde means methanol is not completely oxidized and formaldehyde itself has high toxicity. Besides selectivity, as described in Chapter 1, lower fuel oxidation potential is favored for the fuel cell applications to gain higher open circuit potential.

DNA could be an intriguing polymer scaffold to immobilize nickel. The 3D structure of DNA could have some catalytic effects.[3] Cu^{2+} complexes integrated into a DNA binding domain have shown enantioselectivity for Diels-Alder reactions.[4] It has also been reported that DNA can enhance peroxidase activity of a DNA aptamer-hemin complex, which is dependent on the hemin-binding DNA oligomers' specific folded structures.[5] Since DNA could be used as a self-assembly template,[6] DNA-templated organic synthesis has been developed[7] and metal complexes have been anchored to DNA to make more precisely controlled catalysts.[8] Wei et al. developed a nickel catalyst for a methanol sensor utilizing DNA for formation of catalytic structures on electrode surfaces. DNA-Ni

aggregates were electrodeposited onto a glassy carbon electrode.[9] The electrodeposition time and DNA : Ni ratio were optimized, and the electrode has a linear response range for methanol from 2.0 μM to at least 3 mM. Although this catalyst was developed for a sensor, the cyclic voltammogram in 0.1 M methanol (with the presence of 0.1 M NaOH) showed that the catalyst can tolerate much higher methanol concentration and therefore may be applicable to other applications, including fuel cell electrocatalysis. However, the catalytic mechanism, catalytic specificity and degree of oxidation were not studied by Wei et al.

In this chapter, Ni and DNA-Ni electrodes were prepared to test the catalytic specificity and degree of oxidation of methanol, ethanol, glycerol, and glucose. Methanol oxidation mechanism is examined by performing voltammetric analysis on formaldehyde and formate. It turns out DNA-Ni electrodes oxidize formaldehyde at a significantly higher potential and current than Ni and nucleotide-Ni electrodes, but oxidize formate at a significantly lower potential than Ni and nucleotide-Ni electrodes, and the overall methanol oxidation potential is about 20 mV lower with DNA-Ni electrodes. The 3D structure of DNA-Ni aggregate suggested by AFM, UV-Vis, and XPS should account for this mechanism change. This work is the first evidence of DNA-aggregate-scaffold changes reaction mechanism in alcohol oxidation.

3.2 Experimental

3.2.1 Reagents

Formaldehyde (methanol-free) was obtained from Thermo. Sodium formate-^{13}C, ethanol-2-^{13}C, glycerol-^{13}C3 were obtained from Cambridge Isotope Laboratories, Inc.

Sodium carbonate-^{13}C was from Isotec. Deoxyribonucleic acid sodium salt from calf thymus, nickel (II) chloride (anhydrous, 99.99% trace metals basis), methanol-^{13}C, glucose-$^{13}C6$, adenosine 5'-monophosphate disodium salt (AMP), thymidine 5'-monophosphate disodium salt hydrate (TMP), cytidine 5'-monophosphate disodium salt (CMP) and guanosine 5′ -monophosphate disodium salt hydrate (GMP) were purchased from Sigma-Aldrich. The calf thymus DNA used has a molecular weight between 10-15 million Daltons, 41.9 mole % G-C and 58.1 mole % A-T, corresponding to about 15-23 thousands of base pairs. The approximate length is 5-7 μm, with a diameter about 2 nm. All chemicals were used as received without further purification. All solutions were made with ultrapure water (Milli-Q system, 18.2 MΩ·cm) and degassed with nitrogen. The fuel solutions were all in 0.1 M NaOH solutions and have pH 12.8~12.9.

3.2.2 Sample Preparation- Electrodeposition

Glassy carbon (GC) electrodes were polished with 1 μm and 0.05 μm alumina (Buehler), successively, and then sonicated in ultrapure water and ethanol. According to the procedure of Wei et al.,[9] a 0.1 mg/mL DNA solution and a 0.5 mg/mL $NiCl_2$ solution were made and then mixed and stirred for an hour. Sodium chloride was added before electrodeposition to make a solution containing 0.1 M NaCl electrolyte. Electrodeposition of DNA-Ni onto glassy carbon electrode surfaces was performed with a CH Instruments 611C potentiostat interfaced to a PC computer at 1.8 V (vs. Ag/AgCl (1 M)) for 30 minutes. Ni (0.5 mg/mL $NiCl_2$ precursor solution), DNA (0.1 mg/mL DNA precursor solution), AMP-Ni, TMP-Ni, GMP-Ni, CMP-Ni, and PO_4-Ni electrodes were prepared in the same way. To be consistent with the ligand molar ratio (Ni : ligand = 13.8 : 1) in

DNA-Ni, 0.092 mg/mL AMP, 0.098 mg/mL TMP, 0.098 mg/mL CMP, 0.088 mg/mL GMP were used. To have a Ni to PO_4^{3-} molar ratio of 1 to 1, 0.533 mg/mL NaH_2PO_4 was used for PO_4-Ni. A three-electrode configuration was used throughout all of the electrochemical measurements. The GC electrode (diameter 3mm) was used as the working electrode, platinum mesh as the counter electrode, and Ag/AgCl (1M), saturated calomel electrode (SCE), or Hg/HgO (0.1 M NaOH) as the reference electrode. For consistency, all the results shown were converted to be versus Hg/HgO (1M NaOH). The modified glassy carbon electrodes were rinsed with ultrapure water after electrodeposition and other electrochemical measurements. The same electrodeposition procedure was done to glassy carbon plates for the surface characterization via microscopy and spectroscopy.

3.2.3 Sample Characterization

3.2.3.1 Cyclic Voltammetric Experiments

All cyclic voltammograms (CVs) were collected in the 3-electrode configuration mentioned above. In 0.1 M NaOH, 0.1 M sodium formate (pH 12.8–12.9), 0.1 M formaldehyde (pH 12.8–12.9), 0.1 M methanol (pH 12.8–12.9), 0.1 M ethanol (pH 12.8–12.9), 0.025 M glycerol (pH 12.8–12.9), and 0.025 M glucose (pH 12.7–12.8) solutions were prepared. CVs were taken between 0.288 V and 0.888 V at 0.05 V/s at room temperature. All solutions were degassed with nitrogen and all experiments performed in at least triplicate.

3.2.3.2 Bulk Electrolysis and Product Determinations with NMR

Bulk electrolysis of 0.1 M methanol-^{13}C, 0.1 M ethanol-2-^{13}C, 0.025 M glycerol-^{13}C3 and 0.025 M glucose-^{13}C6 in 0.1 M NaOH was conducted with either a Pine Wavenow potentiostat or a CH Instruments 650A potentiostat at 0.67 V vs Hg/HgO (0.1 M NaOH). Since glucose can be oxidized by air in the alkaline media, the bulk electrolysis of glucose was carried out in an anaerobic glove box (filled with nitrogen). The bulk electrolysis was run for 72 hours in triplicate for each fuel, with 300 μL samples taken at 0 hr, 1 hr, 6 hr, 24 hr, 48 hr, and 72 hr to do NMR. For glucose, a control 0.025 M glucose-$^{13}C_6$ in 0.1 M NaOH solution was also put in the glove box and tested each time as the bulk electrolysis sample. For NMR locking purposes, 300 μL D_2O was added to each sample, and 1800 scans of NMR were taken for most of the fuels, except for glucose, where 3600 scans were used; the shifts are reported relative to tetramethyl silane (TMS). To validate the identification of the oxidation products, 0.1 M sodium formate-^{13}C and 0.1 M sodium carbonate-^{13}C in 0.1 M NaOH solutions were also made and tested in the same way, showing a formate peak at 171.2 ppm and a carbonate peak at 168.4 ppm. According to the literature, the peak at 82.7 ppm should be formaldehyde[10] and the peak at 173.5 ppm should be oxalate.[11]

3.2.3.3 Atomic Force Microscopy (AFM)

A bare glassy carbon plate along with NaCl, Ni, DNA, and three DNA-Ni modified glassy carbon plates (one soaked in DNA-Ni precursor solution for 30 min, one electrodeposited at 0.9 V vs. Ag/AgCl and one electrodeposited at 1.8 V vs. Ag/AgCl) were characterized by a Bruker Dimension Icon-PT atomic force microscope with Peak

Force Tapping mode. Samples were air-dried. The silicon nitride lever has a single cantilever with force constant k=0.4 N/m, resonant frequencies f_0=50-90 kHz, radius of curvature of 2 nm. Images were taken with 1 μm size (512 samples/line) at room temperature. Images were analyzed with Nanoscope Analysis software version 1.20 and first-order flattening was applied to the images.

3.2.3.3 X-ray photoelectron spectroscopy (XPS)

The X-ray photoelectron spectra of DNA-Ni and DNA aggregates electrodeposited on GC plates were acquired by Kratos Axis Ultra DLD. Samples were degassed in the vacuum for two days. The base chamber pressure was 3×10^{-10} torr. The X-ray source is monochromatized Al K_α radiation ($h\nu$ = 1486.6 eV) at 180 W; the survey and high-resolution spectra (O 1s, C 1s, N 1s, P 2p, Ni 2p) were acquired with pass energies of 160 and 40 eV, respectively. Sample charging was controlled using a low-energy electron source coupled with a magnetic immersion lens. Spectra were analyzed with CasaXPS software. 284.8 eV of physisorbed C1s was used to correct the binding energy. Shirley-type background was subtracted before fitting of the peaks. Since the samples were not conductive, asymmetric functions were used to fit the peaks.

3.2.3.4 UV-Visible absorption spectroscopy (UV-Vis)

The ligand-Ni and ligand solutions used before and after electrodeposition were measured with Evolution 260 Bio UV-Visible spectrophotometer from Thermo Scientific. Spectra were scanned from 1100 nm to 200 nm with 60.00 nm/min scan speed, 1 nm bandwidth, and 1.00 nm data interval.

3.3 Results and Discussion

3.3.1 Surface Morphologies

Surface morphologies were characterized with AFM. The bare glassy carbon plate shown in Figure 3.1A has a 0.577 nm root-mean-square roughness for a 1μm×1μm surface area, so the glassy carbon plate is flat enough for use as an AFM substrate. Since the nickel catalysts were electrodeposited in 0.1 M NaCl solution, a control experiment was done where GC plates were submerged in 0.1 M NaCl and a 1.8 V potential was applied. The representative micrograph for this control is shown in Figure 3.1B. The NaCl control contained several residual random size particles with a root-mean-square roughness of 1.26 nm. Compared to the Ni (Figure 3.1C), DNA (Figure 3.1D) and DNA-Ni samples (Figure 3.1E), it is still sufficiently flat. As shown is Figure 3.1 and 3.2, electrodeposition leads to the formation of nanoparticles on GC plates. Even DNA and DNA-Ni look like small particles overlapping each other instead of long strands usually seen on hydrophilic mica surface.[12,13] Section analyses were taken to measure the particle sizes, and the results are summarized in Table 3.1. $NiCl_2$ and DNA-Ni samples have similar particle sizes. The DNA-Ni particle aggregates are slightly larger than DNA aggregates, probably because of the easier crosslinking of DNA strands and the shielding of negative charges of phosphate groups.

This aggregation of DNA to form nanoparticles instead of staying the form of strands is an interesting phenomenon. There are several reasons that might cause the DNA aggregation: The most important reason should be the high voltage (1.8 V) applied during the electrodeposition. Figure 3.2 indicates when no voltage is applied, almost no particles are found on the surface, but DNA-Ni does adsorb on the surface, because the root-mean-

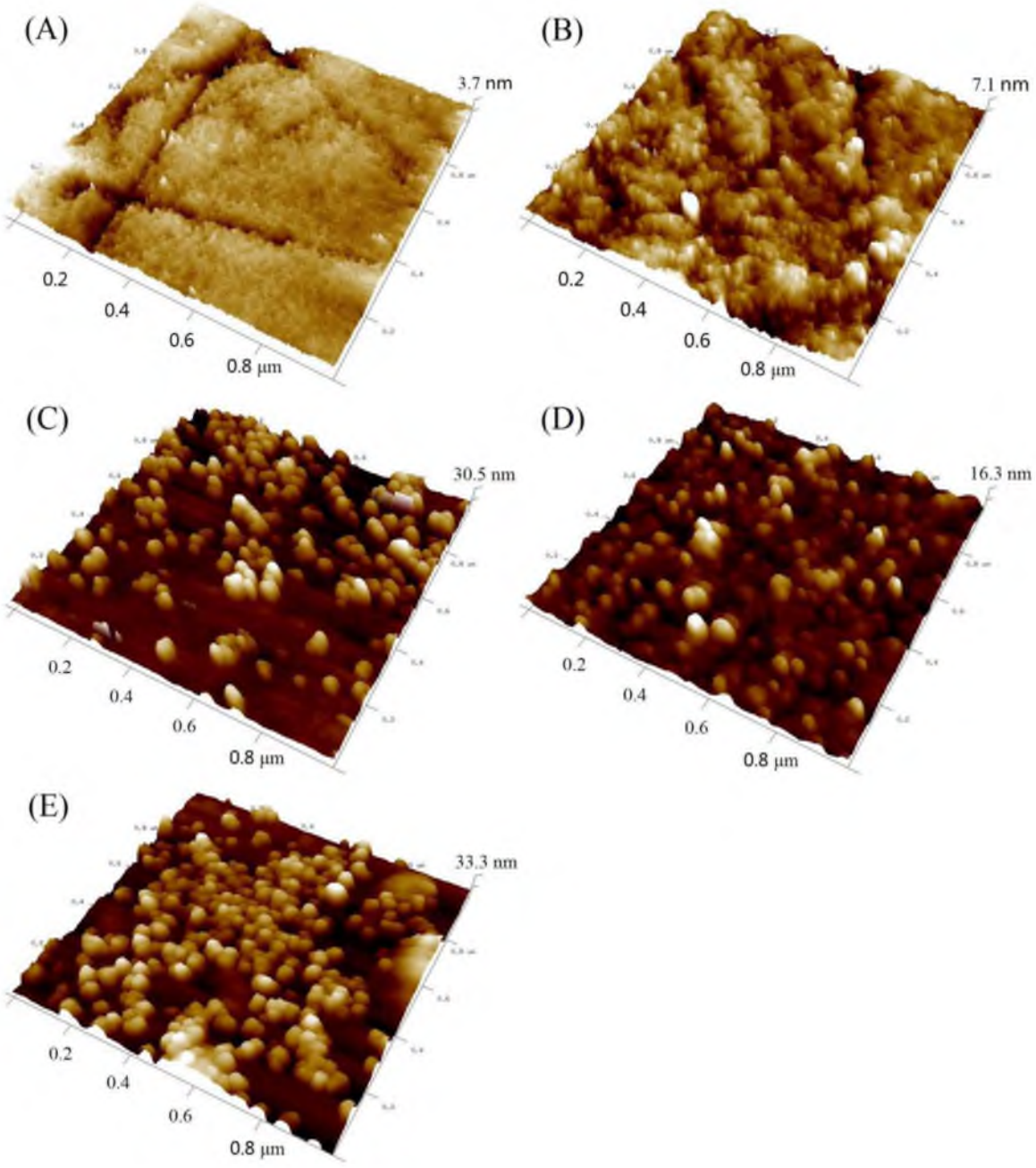

Figure 3.1. AFM 3D height sensor images on GC plates: (A) Bare GC plate. (B) 0.1 M NaCl electrodeposited at 1.8 V. (C) $NiCl_2$ electrodeposited at 1.8 V. (D) DNA electrodeposited at 1.8 V. (E) DNA-Ni electrodeposited at 1.8 V.

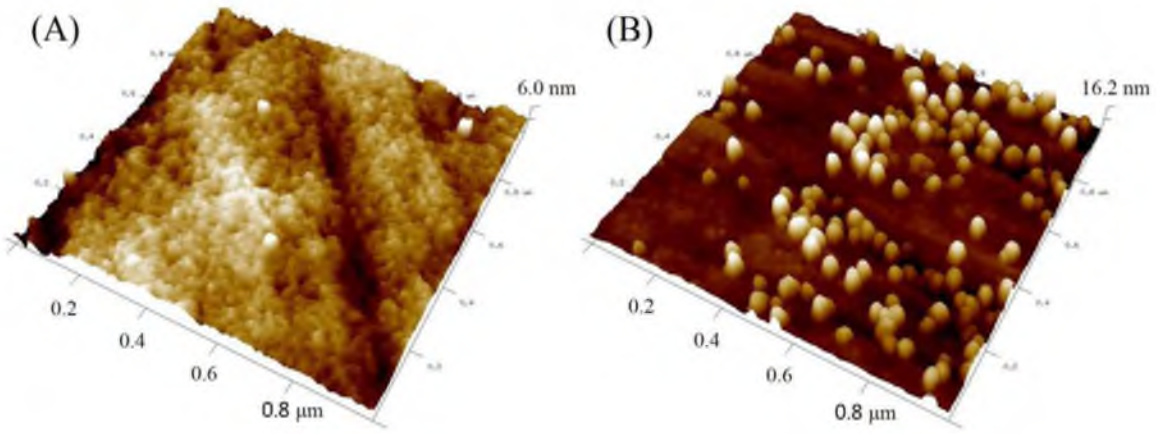

Figure 3.2. AFM 3D height sensor images of DNA-Ni on GC plates: (A) Soaked in DNA-Ni precursor solution for 30 min. (B) DNA-Ni electrodeposited at 0.9 V.

Table 3.1. Particle sizes of electrodeposited samples on GC plates.

Sample	Diameter (nm)	Height (nm)
$NiCl_2$ 1.8 V	40 – 50	10 – 15
DNA 1.8 V	40 – 50	5 – 7 (majority), 2 – 3 and 10 – 15 (minority)
DNA-Ni 1.8 V	40 – 50	10 – 15 (majority), 5 – 10 and 15 – 25 (minority)
DNA-Ni 0.9 V	~ 40	5 – 8

square roughness is 1.12 ± 0.21 nm, which is much larger than the bare GC plate. The particles formed at 0.9 V have smaller height than particles formed at 1.8 V. There is also a study pointing out that on a highly oriented pyrolytic graphite (HOPG) surface when applying a 0.3 V potential (vs Ag wire), the holes among the intertwined DNA mesh became larger and the height also increased slightly compared to free adsorbed DNA.[14] When applying a much higher voltage (i.e., 1.8 V), this effect will be much stronger. Second, glassy carbon is a hydrophobic surface. In the DNA double helix structure, the negative charged sugar phosphate chain is external while the hydrophobic base pairs are in the internal part. On a hydrophilic mica surface, although DNA longer than ~50 nm behave as flexible filaments,[13] 2-5 nM 1868 base pair DNA[13] and 80 μg/mL 3000 base pair DNA[15] on mica still look like individual long strands with height below 1 nm and width around 10 nm[13], but on a hydrophobic carbon surface, the surface free energy will probably draw the DNAs to aggregate. It has been reported that at room temperature the hydrophobic surface can induce local denaturation of DNA to increase the number of bases exposed to the surface,[14] and AFM of 10 μg/mL DNA spontaneous adsorbed on a HOPG surface shows DNA molecules overlap and superpose on each other and look like particles on strands with height around 2 nm and width around 40-50 nm,[16] having similar width with our results. Third, the surface roughness of the substrate and the concentration of DNA solution might also have an effect. For example, 0.1 mg/mL DNA electrodeposited on a HOPG and 0.013 mg/mL DNA electrodeposited on carbon fiber column electrode (CFCE) at 1.8 V both resulted in mesh like DNA structure, but 0.1 mg/mL DNA electrodeposited on CFCE provided large particle-like aggregates.[12] Our GC plates are also rougher than HOPG electrode surface (0.06 nm root-mean-square

roughness for a 1 μm×1 μm surface area[16]). The rough surface will make the nucleation process easier during aggregation. Our concentration is also 0.1 mg/mL, which is relatively high and therefore likely supports easy aggregation.

The sizes of the particles can be used to roughly estimate how many base pairs are in the individual particles. For normal double-stranded DNA structure, A-DNA has the smallest rise per base pairs, 2.56 Å, and Z-DNA has the largest value of 3.7 Å. The diameter of the double-stranded DNA is about 2 to 2.5 nm.[17,18] Because double-stranded DNA has a helix structure, the space that a base pair might take up can be approximated to a cylinder that has the diameter of the DNA as the diameter and the rise per base pair as the height. The volume of the cylinder is from 0.804 nm^3 (using 2.56 Å and 2 nm) to 1.82 nm^3 (using 3.7 Å and 2.5 nm). The shape of the particles can be approximate to a spherical cap and the volume can thus be calculated. The number of the base pair can be roughly estimated by the value of the volume of the spherical cap divided by the volume of a single base pair. If we set the radius of the spherical cap to be 22 nm (because the diameter of the particle is of 40 to 50 nm), the height of 3 nm, 7 nm, 10 nm, 15 nm, and 25 nm corresponding to about 1300 to 2900 base pairs, 3000 to 6800 base pairs, 4500 to 10,000 base pairs, 7300 to 16,000 base pairs, and 15,000 to 34,000 base pairs. Because the initial calf thymus DNA is about 15,000 to 23,000 base pairs, it is very possible that the initial DNA is broken and/or does not reserve double-stranded structure during the 1.8 V electrodeposition. Indeed, the experiments of Kataoka et al. also suggest that deduction. They packaged plasmid DNA (4361 base pairs) into spherical polyplex micelles (diameters of 50 to 100 nm) by simply mixing the polymer and pDNA, and they found out by gel electrophoresis that the dissociation and nuclease cleavage of the packed

double-stranded DNA had occurred randomly.[19] Because double-stranded DNA is a stiff macromolecule, its flexibility is restricted and can be described by the persistence length. The fact that all the diameters of the particles are about 40 to 50 nm might be due to the persistence length of the double-stranded DNA being about 40 to 50 nm in the presence of 0.1 M Na^+.[18]

3.3.2 Electrocatalytic Properties

3.3.2.1 Fuel Diversity

The electrocatalytic properties of Ni and DNA-Ni electrodes were characterized with cyclic voltammetry. Figure 3.3 shows the representative cyclic voltammograms in different fuel solutions (methanol, ethanol, glycerol, and glucose), where bare and DNA aggregate-modified GC electrodes were used as controls. Blank experiments in 0.1 M NaOH and no fuel are also shown. Ni and DNA-Ni behave quite similar in these solutions. Both of them have the irreversible fuel oxidation peaks and redox peaks of Ni(II) and Ni(III), and all of the fuels showed oxidation. The increasing current near 0.7 V is because of the oxygen evolution reaction.[20] The peak positions and peak currents of fuel oxidation are summarized in Table 3.2. Similar to other nickel complex electrocatalysts, Ni was first oxidized to Ni(III) in alkaline solution, and then the Ni(III) oxidized the fuels irreversibly. In the cathodic scan, both freshly chemisorbed substrate and residual adsorbed carbonaceous species were oxidized[21] and Ni(III) was reduced to Ni(II). The "dip" during the cathodic scan is not due to breaking down or serious morphological changes of the electrocatalyst during the cathodic scan for the DNA-Ni aggregates, since the voltammograms are quite stable during multiple scans (>100 scans).

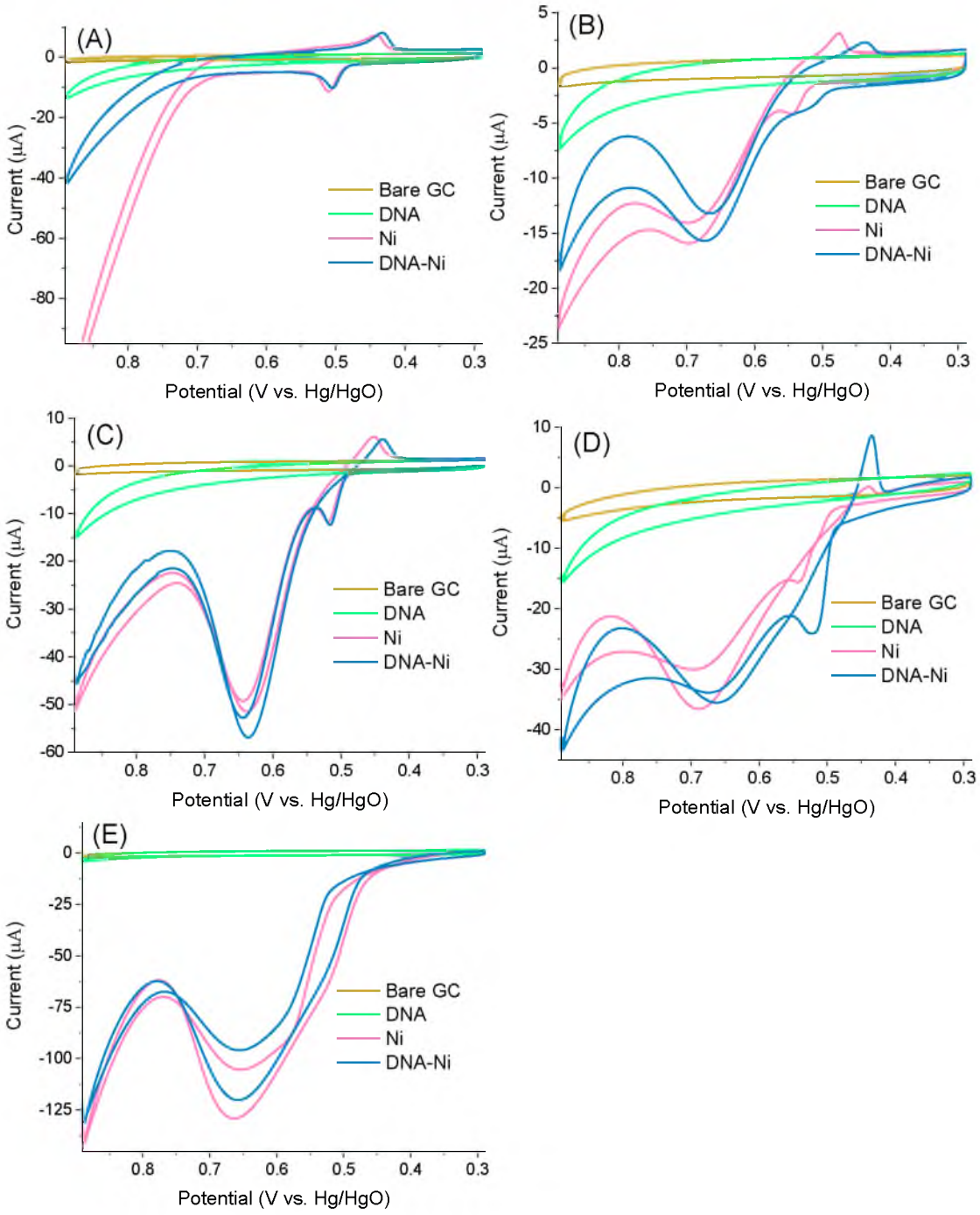

Figure 3.3. Representative cyclic voltammograms at a scan rate of 0.05 V/s: (A) 0.1 M NaOH. (B) 0.1 M NaOH and 0.1 M methanol. (C) 0.1 M NaOH and 0.1 M ethanol. (D) 0.1 M NaOH and 0.025 M glycerol.(E) 0.1 M NaOH and 0.025 M glucose.

Table 3.2 Fuel oxidation peak position and peak current at Ni and DNA-Ni electrodes.

Fuel	Concentration (M)	Catalyst	Peak position (V)	Peak current (μA)
Methanol	0.1	Ni	0.684 ± 0.015	66.01 ± 32.78
		DNA-Ni	0.662 ± 0.012	40.77 ± 21.54
Ethanol	0.1	Ni	0.636 ±0.003	39.23 ± 4.86
		DNA-Ni	0.637 ± 0.007	46.24 ± 9.33
Glycerol	0.025	Ni	0.696 ± 0.015	34.28 ± 10.15
		DNA-Ni	0.667 ± 0.016	32.04 ± 10.14
Glucose	0.025	Ni	0.654 ± 0.021	85.13 ± 27.71
		DNA-Ni	0.644 ± 0.008	74.22 ± 8.08

Wei et al. contributed this "dip" to the reduction of strongly adsorbed OH^-, making available sites for methanol oxidation to happen again,[22] while other studies of nano-structured nickel oxide contributed this to the diffusion and convection mass transfer or the reduction of the passive film formed during anodic scan, making fuel oxidation occur again during the cathodic scan.[23,24] The oxidation peaks of glycerol and glucose are much broader than methanol and ethanol, and they have much higher peak currents, especially the glucose, suggesting either more electrons were produced with glycerol and glucose, or a fast catalytic reaction.

An important feature of any fuel cell or battery is its high energy density. The energy density of pure methanol, ethanol, glycerol, and glucose fuels are 6.1, 8.0,[25] 5.0,[26] 4.4[27] kWh/kg, respectively. Although these energy densities are lower than gasoline (10.5 kWh/kg),[25] they are large compared to the energy density of typical batteries. In order to realize high energy densities, deep oxidation of the fuels is required. Bulk electrolysis with ^{13}C NMR analysis of the waste products was used to determine the final products of the oxidation reactions of each of the fuels.

In the cases of glycerol and glucose, the pH drops during bulk electrolysis. For a solution with an initial pH of 12.90, after bulk electrolysis the pH decreased to 12.75 for glycerol and 12.70 for glucose, which is consistent with the production of protons during fuel oxidation. In glycerol oxidation, the ^{13}C NMR of the product formation during the first 24 hours shows only formate and carbonate as products. After 24 hours, small amounts of formaldehyde, oxalate, and glycolate start forming, showing a pH-dependent electrocatalytic mechanism. For glucose oxidation, in the first 2 hours of glucose's oxidation, only formate showed in the ^{13}C NMR. After that, carbonate and oxalate

showed up with small amounts of glycolate and gluconate. These phenomena show that the catalytic mechanism is pH dependent and changes during the long operation time in batch mode, because pH of the fuel solution is changing with time.

Table 3.3 presents the main products of each fuel. The presence of carbonate in the products indicates that nickel-based catalysts can deeply oxidize the fuels. Methanol can be completely oxidized to carbonate, producing up to 6 electrons per molecule of methanol. This has been verified by performing voltammetric analysis on formaldehyde and formate, and verifying the ability of the Ni and DNA-Ni to oxidize all intermediate oxidation products of methanol, as shown in Figure 3.4 in Section 3.3.2.2. On the other hand, the DNA-Ni do not appear to be able to break the carbon-carbon bond of ethanol, so only 4 electrons can be produced from the oxidation of ethanol to acetate. Glycerol and glucose can be deeply or completely oxidized, as shown by the production of carbonate.

The deep oxidation of glycerol and glucose to carbon dioxide shows the oxidation catalyzed by nickel-based catalysts can even break the carbon-carbon bond, which most precious-metal-based catalysts cannot.[1] It also appears that additional hydroxyl functional groups improve deep oxidation. In methanol, the carbonate showed up between 24 to 48 hours, while in glycerol and glucose the carbonate showed up between 2 to 24 hours. This is consistent with some other inorganic catalysts. For instance, the oxidation of various carbohydrates at copper electrodes also indicated the need for the presence of at least two hydroxyl groups for facile oxidation, and preferably more.[28] All in all, the deep oxidation ability of nickel-based catalysts for these fuels make them a good candidate for fuel cell applications.

Table 3.3. Product distributions of the oxidations of methanol, ethanol, glycerol, and glucose.

Fuel	Catalyst	Main products		
0.1 M Methanol	Ni	Formate	Carbonate	
0.1 M Methanol[a]	DNA-Ni	Formate	Carbonate	
0.1 M Ethanol	DNA-Ni	Acetate		
0.025 M Glycerol	DNA-Ni	Formate	Carbonate	
0.025 M Glucose	DNA-Ni	Formate	Carbonate	Oxalate

[a]For methanol with DNA-Ni, formaldehyde showed up occasionally.

3.3.2.2 Electrocatalytic Properties Differences between Ni and DNA-Ni

Although similar bulk electrolysis products were detected and similar methanol oxidation currents were measured from voltammetric analysis with similar amounts of nickel catalysts (in 0.1 M NaOH the Ni(III) peak current of Ni is 6.19 ± 2.57 μA and DNA-Ni is 8.06 ± 4.41 μA), DNA-Ni electrodes oxidize methanol at a lower potential than Ni electrodes (95% confidence using t-test) by about 22 mV (Table 3.2). Methanol can lose two electrons to form formaldehyde, another two electrons to form formate and another two electrons to form carbonate during the oxidation in alkaline media, as shown in the results of bulk electrolysis. To study the details of this mechanism, formaldehyde and formate were used as fuel substrates with voltammetric analysis to verify the ability of the Ni and DNA-Ni to oxidize all intermediate oxidation products of methanol. It turns out Ni and DNA-Ni electrodes oxidize formaldehyde and formate quite differently. The representative voltammograms are shown in Figure 3.4. DNA-Ni electrodes oxidize formaldehyde with a peak at 0.700 ± 0.010 V and a peak current of 325.10 ± 10.25 μA. Ni electrodes oxidize formaldehyde with a peak at 0.617 ± 0.025 V and a peak current of 209.80 ± 38.91 μA (the data are summarized along with data from other ligand-Ni electrodes in Table 3.4). That is, DNA-Ni electrodes oxidize formaldehyde at about 0.08 V higher than Ni electrodes with about 100 μA more current output. DNA-Ni electrodes also oxidize formate with a peak at 0.602 ± 0.012 V and a peak current of 1.67 ± 0.53 μA. The formate oxidation peak is more pronounced when using a slow scan rate 0.005 V/s, but Ni electrodes do not show any formate oxidation peaks in the voltammograms. Since carbonate was also detected in methanol bulk electrolysis solutions with Ni electrodes, Ni electrodes may oxidize formate at around or higher than 0.7 V, and the

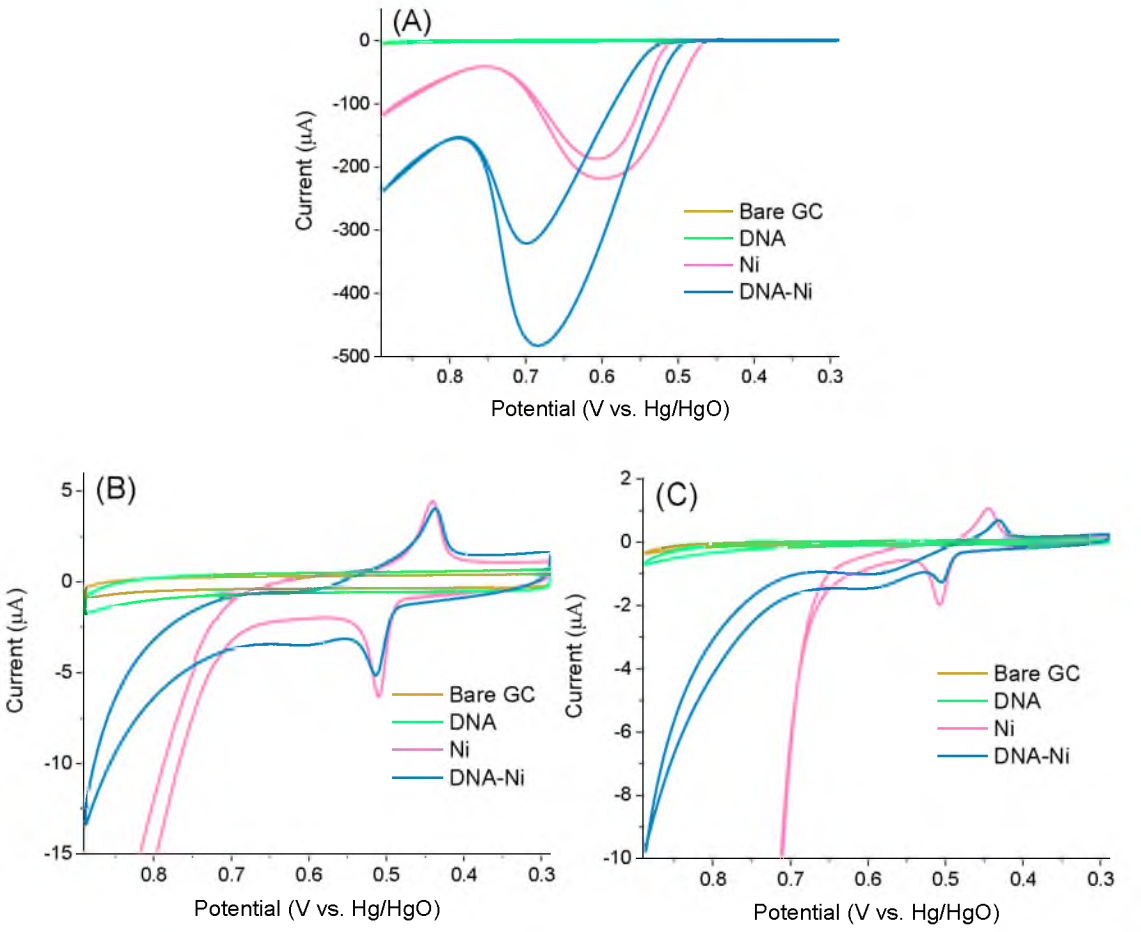

Figure 3.4. Representative cyclic voltammograms of formaldehyde and formate oxidation in 0.1 M NaOH: (A). 0.1 M formaldehyde at the scan rate of 0.05 V/s. (B) 0.1 M formate at the scan rate of 0.05 V/s. (C) 0.1 M formate at the scan rate of 0.005 V/s.

Table 3.4 Formaldehyde oxidation peak position and peak current.

Catalyst	Peak position (V)	Peak current (μA)
Ni	0.617 ± 0.025	209.80 ± 38.91
PO_4-Ni	0.600 ± 0.012	169.06 ± 41.59
AMP-Ni	0.611 ±0.006	151.56 ± 50.26
GMP-Ni	0.580 ± 0.017	173.78 ± 19.85
CMP-Ni	0.611 ± 0.011	76.78 ± 21.32
TMP-Ni	0.638 ± 0.007	177.8 ± 57.6
DNA-Ni	0.700 ± 0.010	325.10 ± 10.25

peak is buried in dramatically increased oxygen evolution current. This has been demonstrated by having Ni electrodes to do bulk electrolysis with formate. Carbonate is detected as the oxidation product, so Ni electrodes oxidize formate at a higher potential than DNA-Ni electrodes do.

This mechanism difference can bring different applications of Ni and DNA-Ni electrodes. Based on the CVs of methanol, formaldehyde, formate oxidation, DNA-Ni electrodes can completely oxidize methanol at a potential about 0.1 V lower than Ni electrodes, because DNA-Ni electrodes can oxidize methanol, formaldehyde and formate at around 0.55 V, but Ni electrodes have to oxidize formate at a potential higher than 0.65 V. In addition, DNA-Ni electrodes oxidize methanol at about 20 mV lower potential than Ni electrodes, so DNA-Ni electrodes are more favored in general fuel cell applications. On the other hand, if the formate produced will be used in direct formic acid fuel cells, which have open circuit potential 0.27 V higher than direct methanol fuel cells and other advantages (e.g., nonflammable, nontoxic, and so on),[29,30] Ni electrodes are preferred.

To clarify the origin of this mechanism difference, PO_4-Ni, AMP-Ni, TMP-Ni, CMP-Ni, and GMP-Ni are also tested, because the phosphate groups and nucleotides are the basic components of DNA. 0.1 M formaldehyde was used because the effect is easy to observe. Figure 3.5 shows all of the DNA component-Ni electrodes oxidize formaldehyde at a lower potential and a lower current than DNA-Ni electrodes, similarly to Ni electrodes. Table 3.4 summarizes the data. Among these nucleotide-Ni electrodes, TMP-Ni has a slightly higher peak potential than others and CMP-Ni has the lowest peak current. The fact that none of the DNA components show similar formaldehyde oxidation behavior as DNA scaffolds indicates the 3D DNA chain structure should be important.

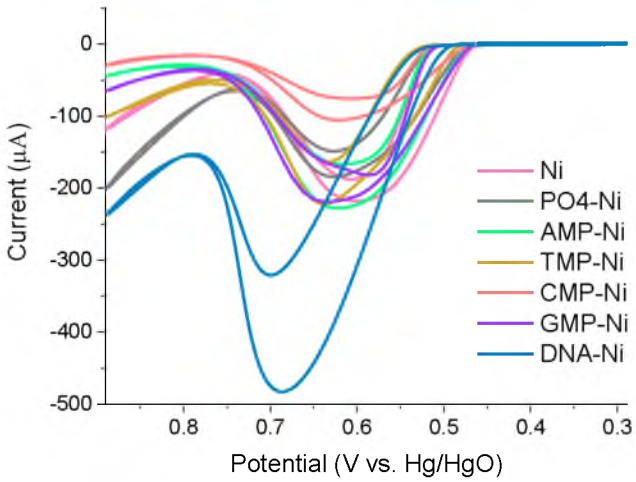

Figure 3.5. Representative cyclic voltammograms of formaldehyde oxidation by Ni, PO_4-Ni, AMP-Ni, TMP-Ni, CMP-Ni, GMP-Ni and DNA-Ni electrodes in 0.1 M NaOH. Scan rate 0.05 V/s.

To further study the differences between small ligand-Ni and DNA-Ni, UV-Vis experiments were performed.

3.3.3 Electronic Transitions in UV-Vis

The catalytic properties are mainly dependent on the metal ion and its environment. UV-Vis absorption spectroscopy can provide information on the electronic transitions in the sample. The solutions used for electrodeposition were tested with UV-Vis absorption spectroscopy before and after electrodeposition. Figure 3.6A shows the spectra of $NiCl_2$. The peaks at 394 nm, 666 nm, and 723 nm are d-d transitions of $^3A_{2g}$ to $^3T_{1g}(P)$, two mixed states of $^3A_{2g}$ to ^1E_g and $^3A_{2g}$ to $^3T_{1g}$ (F), respectively.[31] Treatments with 1.8 V do not change these three peaks. The spectra of $NiCl_2$ with different ligands and DNA scaffold after 1.8 V treatments are shown in Figure 3.6B and C. DNA and the nucleotides have absorption peaks around 250 nm to 260 nm. These absorption bands usually range from 230 nm to 300 nm, but the peaks of GMP-Ni, AMP-Ni and DNA-Ni 1.8 V have tails after 300 nm. The tails of GMP-Ni and AMP-Ni have a "dip" at around 350 nm, but the tail of DNA-Ni does not. Thus the Ni^{2+} peak of $^3A_{2g}$ to $^3T_{1g}(P)$ is buried in the tail of the DNA peak, while with other ligands, it is not. It looks like the $^3A_{2g}$ to $^3T_{1g}(P)$ peak of Ni^{2+} in DNA-Ni is blue shifted a bit, but it is hard to confirm with the UV-Vis data only, because of the overlap with DNA peak. The XPS analysis in the following section will confirm that the energy state of Ni in DNA-Ni is different from small ligand-Ni.

For easy comparison of the peak shape, all spectra are normalized with the peak intensity around 260 nm except the $NiCl_2$ spectrum in Figure 3.7. It is clear that CMP-Ni and TMP-Ni are almost not changed after 1.8 V treatments. GMP-Ni is slightly redshifted

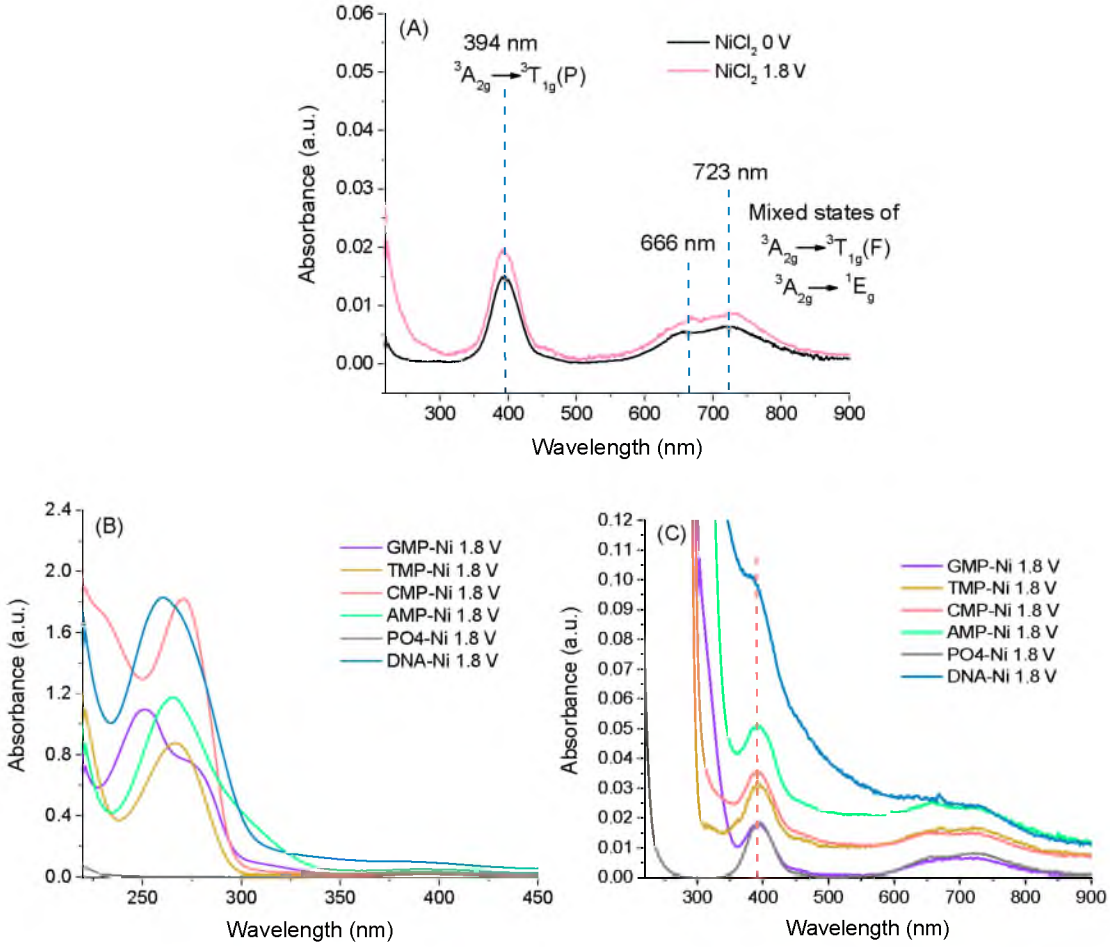

Figure 3.6. UV-Vis spectra of $NiCl_2$, ligand-Ni and DNA-Ni after 1.8 V treatments: (A). $NiCl_2$ before and after 1.8 V. (B). Ligand-Ni and DNA-Ni after 1.8 V showing the aromatic ring absorption range. (C). Ligand-Ni and DNA-Ni after 1.8 V showing the Ni^{2+} d-d transition absorption range.

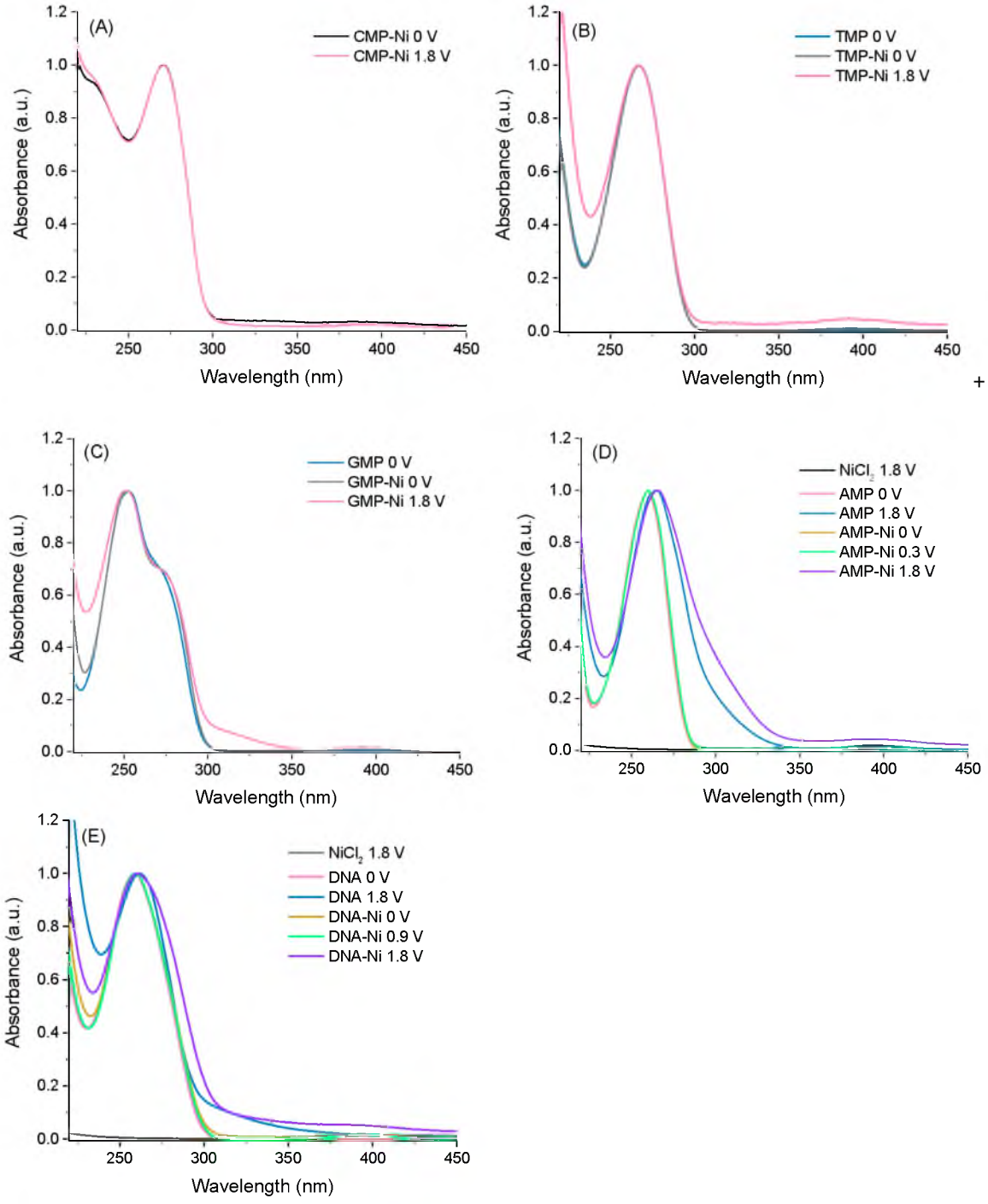

Figure 3.7. Normalized UV-Vis spectra of ligand and ligand-before and after applying potentials: (A). CMP-Ni. (B). TMP and TMP-Ni. (C). GMP and GMP-Ni. (D). AMP and AMP-Ni. (E). DNA and DNA-Ni.

and has a new peak tail at wavelengths larger than 300 nm after 1.8 V treatments. AMP-Ni and DNA-Ni 1.8 V not only have this peak tail, but also show the entire spectra red shifted. These changes only happen with applied potential high enough, since the spectra of AMP-Ni 0.3 V and DNA-Ni 0.9 V do not have these changes. When comparing spectra with and without Ni at 1.8 V, it shows with Ni the peak tail and the peak shift are more pronounced. The existence of the peak tail and the peak shift is considered to be the sign of Ni-ligand coordination and the increased degree of π-π stacking of the nucleotides or DNA.[32,33] Since the DNA and DNA-Ni aggregates form nanoparticles instead of strands, the degree of π-π stacking could increase greatly. In this study, the oxidation of nucleotides suggested by the XPS analysis can also be part of the reason of the spectra change.

3.3.4 Chemical Composition Analysis with XPS

The chemical compositions of DNA and DNA-Ni aggregates were obtained by XPS. The atomic concentrations of each element are summarized in Table 3.5. The theoretical N/P ratio of the calf thymus-dsDNA is 3.7/1.[12] In the DNA aggregates, the N/P ratio is 4.3/1 and, in the DNA-Ni aggregates, the N/P ratio is 3.7/1. Both values are close to the theoretical value, indicating the DNA was immobilized on the GC electrodes. The P/Ni ratio in DNA-Ni is 5/1, which means there is approximately 1 Ni atom per 5 DNA bases in the DNA-Ni. According to literature,[34-36] Ni(II) mainly coordinates with N7 centers of guanines and interacts with phosphate groups of DNA. The study of Sorokin et al. on Ni interaction with native DNA and nucleotides via UV-Vis spectrometry shows that Ni^{2+} coordinates N7 of GMP, N7 and N1 of AMP and interacts with O2 of CMP and the

Table 3.5. The atomic concentrations (%) of elements in DNA and DNA-Ni.

aggregates	O	N	C	P	Ni
DNA	27.2	6.4	65.0	1.5	0.0
DNA-Ni	21.6	11.4	63.2	3.1	0.6

phosphate groups of TMP. Ni^{2+} does not interact with N3 of CMP, but when it is in the DNA structure, the interaction of Ni^{2+} with N7 of guanosine will result in internal protonation of N3 of cytidine of the G-C pairs.[33] On a GC surface, in 60 μg/mL calf thymus DNA solution, guanine will be oxidized at 1.03 V and adenine will be oxidized at 1.30 V (vs Ag/AgCl, 3 M KCl),[16] and in 40 μg/mL single-stranded DNA solution, all bases are oxidized below 1.5 V (vs Ag/AgCl, 3 M KCl) with poly(dG) being oxidized around 0.9 V and poly(dA) being oxidized around 1.2 V,[37] so even though the double-stranded structure may provide more protection of bases than the single-stranded structure, bases can still be oxidized to some degree during the electrodeposition process at 1.8V. In the literature, guanine will be oxidized to guanidinohydantoin (dominates at pH < 10.1) and its isomer iminoallantoin (dominates at pH > 10.1),[38] and adenine will be oxidized to a 2,8-dihydroxyadenine's diimine tautomer.[39] Cytosine and thymine are more difficult to be oxidized than guanine and adenine, and they may have various oxidation products.[40] The 2'-deoxyribose and the orthophosphate are electro-inactive at least from 0.3 V to 1.6 V.[37] According to the UV-Vis results of CMP-Ni and TMP-Ni in Section 3.3.3, cytosine, thymine, 2'-deoxyribose and the orthophosphate are probably not oxidized in DNA. The oxidation of DNA results in more [N–C(=O)–N] groups to guanine and adenine, but their N7 nitrogens are not imine functional groups anymore. Because UV-Vis studies in Section 3.3.3 show that Ni ion still has strong interaction with oxidized GMP and AMP, Ni could coordinate to the functional groups in the new structures. The relevant structures of the nucleotides and nucleosides are shown in Figure 3.8. Since there is about 1 Ni ion per 5 DNA bases and the coordination number of Ni is usually 4 or 6, for 2 Ni ions, there will be 10 bases providing 8 to 12 binding sites.

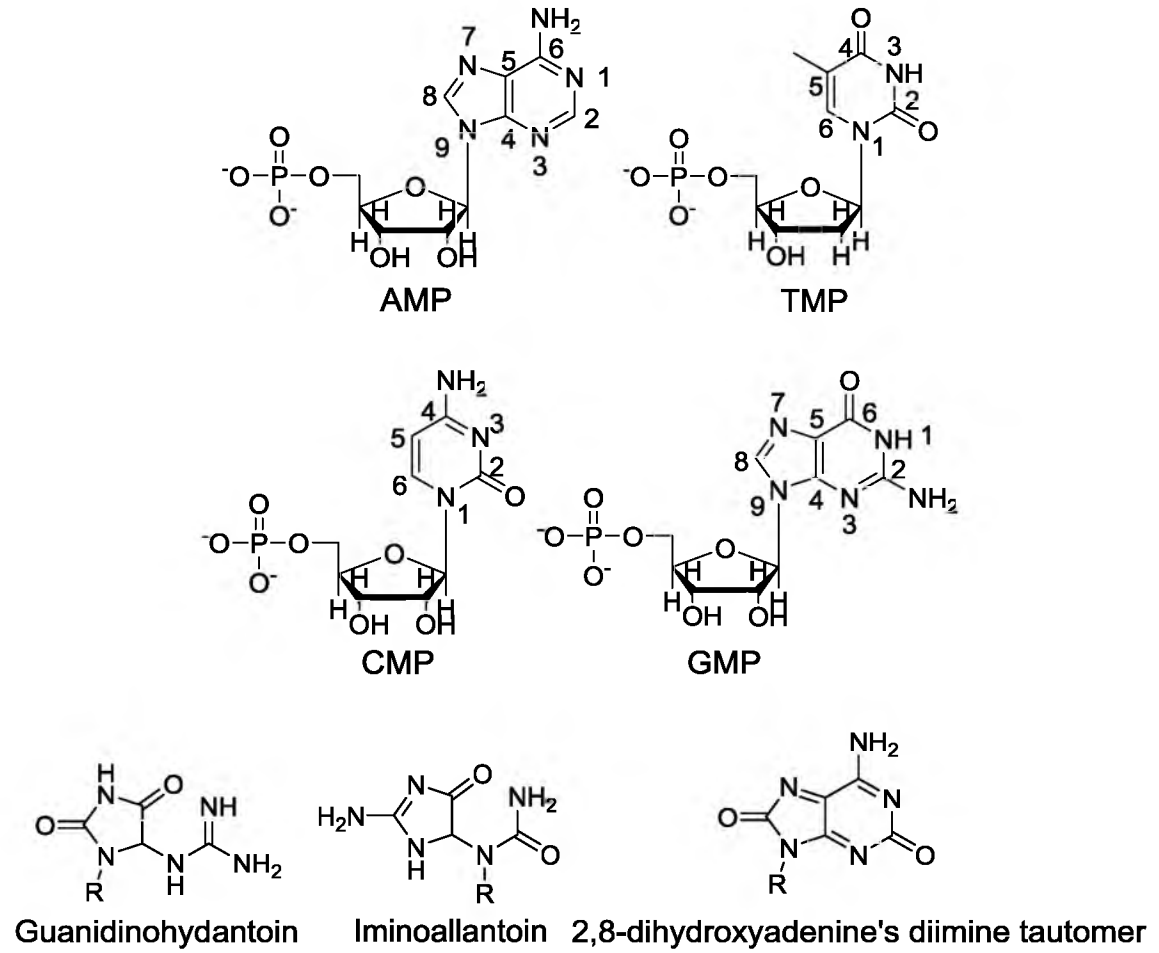

Figure 3.8. Chemical structures of the nucleotides used in this study and possible oxidation products.

Table 3.6 summarizes the C1s components of XPS high-resolution deconvolution spectra of the electrodeposited DNA and DNA-Ni aggregates shown in Figure 3.9. The peak assignments are according to XPS studies of calf thymus DNA and single-stranded DNA.[41,42] In the study by Lin et al., the peak around 289 eV is assigned to the carboxylate group.[12] In theory, the area ratio of these 4 peaks should be 285 eV: 287 eV : 288 eV : 289 eV = 18% : 46% : 37% : 5%. The hydrocarbons' (285 eV) ratios are much higher in the XPS results, due to the large amount of physisorbed hydrocarbon. If the 285 eV component is excluded, the calculated 287 eV, 288 eV and 289 eV components' ratios should be 287 eV : 288 eV : 289 eV = 9 : 6 : 1 = 56.3% : 37.5% : 6.3%. The 289 eV components' ratios are much higher than the theoretical value, indicating the oxidation of bases. In the DNA sample, if we assumed all dA and dG were converted to the final products, 287 eV : 288 eV : 289 eV = 3.51 : 1.73 : 1 = 52.7% : 31.2% : 16.0%; this ratio is pretty close to the experimental value, although the experimental percentage of 287eV and 289 eV components are still relative high and 288 eV is low. This difference may come from the (C–O–C) (287 eV) bonds linking DNA to the carbon surface.[12]

After being coordinated with Ni, all of the peaks' positions look stable, except the 289 eV component drops 0.3 eV, which shows this component is relative to the Ni ions. Meanwhile, the percentage area of the 288 eV component stays at 25.9%, and 7.1% of the 289 eV component is converted to the 287 eV component. Both [N–C(=O)–N] and carboxylate groups interacting with Ni ions can explain these changes. For [N–C(=O)–N] groups, the isomerization to [N=C(–O$^-$)–N] and coordinating Ni ions with either carboxylate group or imine group will drag electrons towards carbon, making the binding energy lower.[43] This isomerization may be favored because it can often recover the ring

Table 3.6. XPS high-resolution C 1s spectra of DNA and DNA-Ni aggregates.

		C-C, C=C, C-H	C-N, C-O, N-C-N	N-C(=O)-C, N=C-N, N-C-O, N-C(=N)-N	N-C(=O)-N, -COO$^-$
Main Peaks (eV)	DNA	284.8	286.7	288.0	289.2
	DNA-Ni	284.8	286.7	287.9	288.9
Area ratio (%)	DNA	68.1	18.5	8.3	5.2
	DNA-Ni	61.6	25.0	10.0	3.4
Area ratio exclude 284.8 eV (%)	DNA		58.0	25.9	16.1
	DNA-Ni		65.1	25.9	9.0

Asymetric peak shape for peaks, CasaXPS peak shape parameter is A(0.25,0.3,30)GL(30), with FWHM of DNA aggregates 1.47eV and DNA-Ni aggregates 1.33 eV.

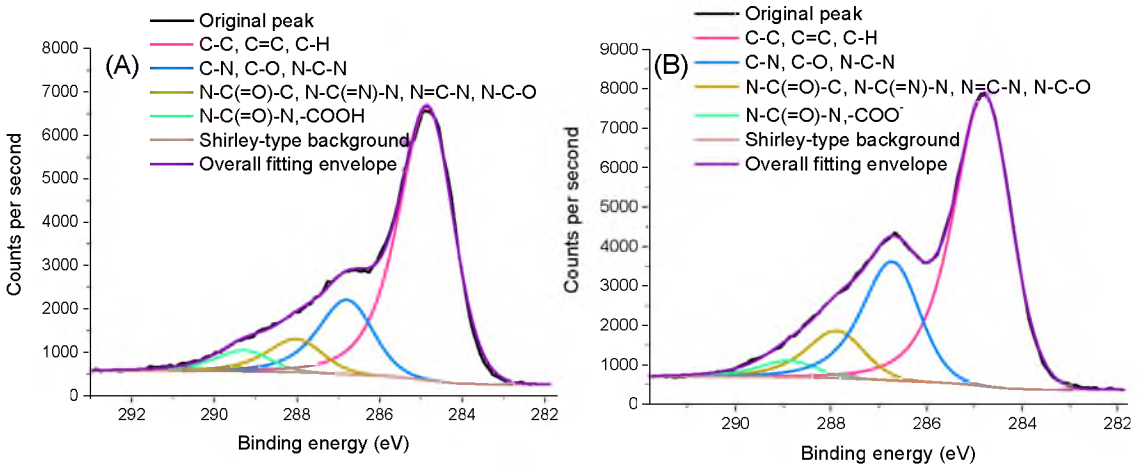

Figure 3.9. XPS high-resolution deconvolution C 1s spectra: (A) DNA aggregates. (B) DNA-Ni aggregates.

structure, although it may break some hydrogen bonds. For carboxylate groups, if they coordinate unidentate with Ni ions, the carbon of the carboxylate group can shift to 288.9 eV;[44] but if they coordinate bidentate with Ni ions, the carbon of the carboxylate group can shift to around 287 eV.[45] In both cases, the electron density of carbon increased.

The deconvolution spectra of the P 2p spectra [asymetric peak shape A(0.25,0.3,30)GL(30)] show that in the DNA aggregates, the P $2p_{3/2}$ peak (FWHM 1.70 eV) is at 133.8eV ($2p_{1/2}$ 134.6 eV) and, in the DNA-Ni aggregates, the P $2p_{3/2}$ peak (FWHM 1.43 eV) is at 133.6eV ($2p_{1/2}$ 134.5 eV). The 0.2 eV difference is quite small, but if the two spectra (after subtracting the Shirley backgrounds) are overlapped, there is a peak shift that can be observed, as shown in Figure 3.10B. It is consistent with the results of the study using Cd^{2+} to react with phosphorothioate $OligoG_{10}$.[46] In this study, the binding energy of P 2p dropped 0.4 eV after Cd^{2+} interacted with PO_2^- group. The smaller energy difference in the Ni aggregate case indicates the interaction between the Ni and the phosphate group is weaker than the Cd^{2+} case in literature. Indeed, Ni ion may bridge phosphate groups of two neighboring duplexes via water.[31] This explains the minor change of the P 2p spectra.

Carbon and phosphorous are elements interacting with Ni indirectly, while oxygen and nitrogen are elements directly coordinating with Ni ions. Since the DNA are not strands anymore, but an aggregate-like sphere, we can predict that there will be more hydrogen bonding connecting many bases together. All of the amine groups could become donors and all imine and carbonyl groups could become acceptors. H_2O could also participate in this large hydrogen bonding network. This large hydrogen bonding network makes the interpretation of O 1s and N 1s XPS spectra very complicated. N 1s

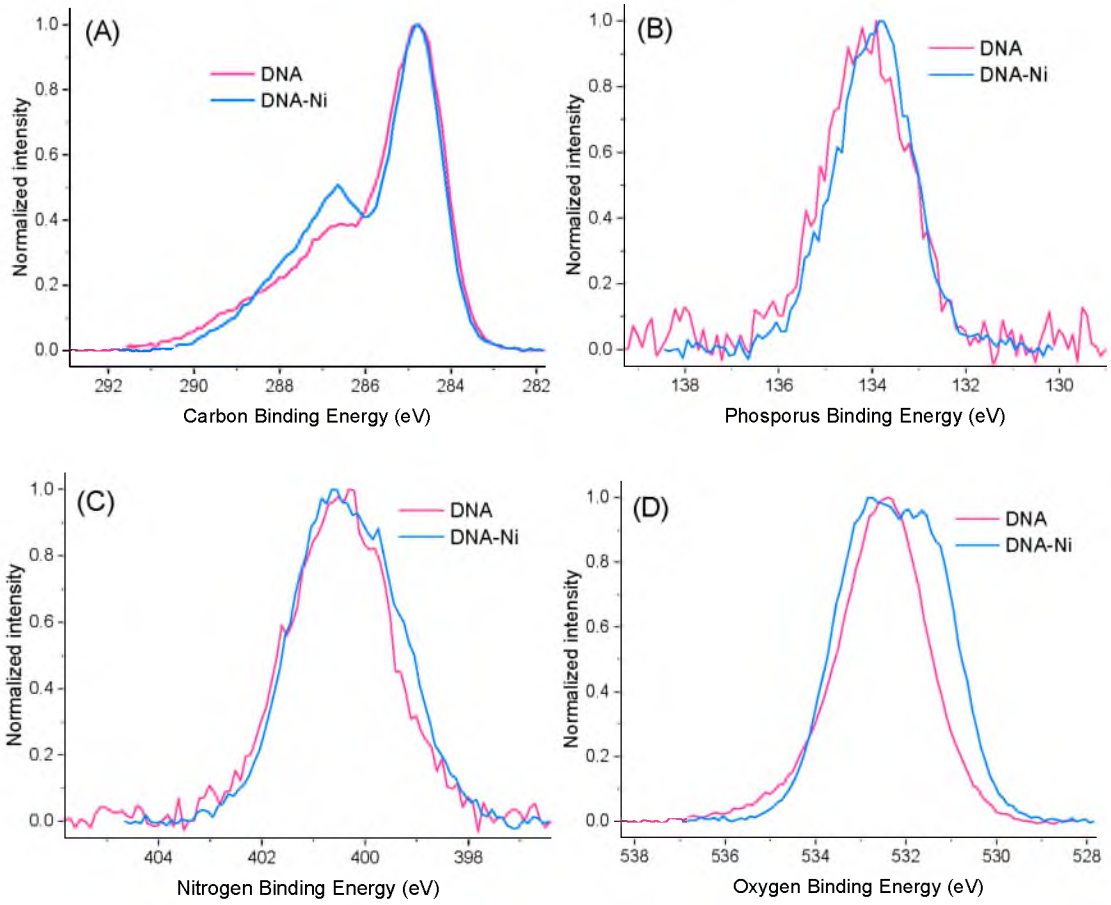

Figure 3.10. XPS spectra (subtracted the Shirley backgrounds, and for quick comparing the peaks' shapes, all the peaks were normalized with their own highest peak intensities): (A) Carbon. (B) Phosphorus. (C) Nitrogen. (D) Oxygen.

spectra usually have -CH=N- groups locate around 399 eV and amine and amide groups locate around 400 eV.[47,48] N 1s spectra of DNA and DNA-Ni have components locating significantly higher than 400 eV. After metal ions coordinate with imine-N, the binding energy can increase from 0.7 to 1.8 eV.[49,50] After amine-N forms hydrogen bonds with the carbonyl groups, the binding energy can increase from 1.3 to 1.9 eV.[51] In double-stranded DNA, the N---N distance in the hydrogen bond is 3.0 Å and the O---N distance is 2.9 Å.[52] It has been reported that in a series of free-base porphycenes, the binding energy differences between amine-N and imine-N are 2.1 eV, 1.75 eV, 1.4 eV and 0.95 eV, corresponding to N---N distances 2.93 Å, 2.79 – 2.80 Å, 2.61 – 2.62 Å, and 2.51 Å.[53] Therefore, even the small distance change of the hydrogen bond can result in large binding energy differences. It will be very difficult to differentiate Ni ions' coordination from hydrogen binding. However, if the spectra (after subtracting the Shirley backgrounds) before and after Ni coordination are overlapped, as shown in Figure 3.10C, it can be observed that the area at lower binding energy grew. In the case of oxygen (Figure 3.10D), there is a significant energy decrease too. These two changes are most likely due to the ligand-Ni coordination.[54] As shown in the following paragraph, DNA-Ni has Ni 2p shift to higher binding energy compared to other small ligand-Ni, so some of the electron density is transferred from Ni to O and N, making Ni binding energy higher and N and O binding energy lower. It could also be because after Ni coordination (e.g., Ni coordinating with base pairs),[55] some hydrogen bonds were broken, opening the hydrogen bonding network a bit. The isomerization of [N–C(=O)–N] groups to [N=C(–O⁻)–N] could be another reason. The isomerization created more imine groups that are not hydrogen bonded or coordinated with Ni ions.

Sets of Ni $2p_{3/2}$ peaks and $2p_{1/2}$ peaks are shown in Figure 3.11A. They are well separated by 17.27 eV as reported. Two types of Ni ion coordination are found at 856.7 and 859.0 eV, and their ratio is 3.33 : 1. In both $2p_{3/2}$ peaks and $2p_{1/2}$ peaks, there are sets of shake up peaks, indicating the two types of Ni are both paramagnetic and may have octahedral or tetrahedral stereochemistry. Depending on the nature of the ligands, when no halogen acts as ligands, there may be two types of shake-up peaks: Type A has one shake-up peak for $2p_{3/2}$ and two for $2p_{1/2}$; Type B has one for both.[56] The area of $2p_{1/2}$ peaks should be half of the $2p_{3/2}$ peaks, but clearly the area percentage of shake-up peaks in $2p_{1/2}$ peaks is much higher than in $2p_{3/2}$ peaks, so 2 peaks were used to fit the $2p_{3/2}$ shake-up peaks while 3 peaks were used to fit the $2p_{1/2}$ shake-up peaks. Therefore the coordination environments of these two types of Ni are different. More importantly, when comparing DNA-Ni spectrum to cysteine-Ni and Ni spectra in Chapter 2 (Figure 3.11B), DNA-Ni has the binding energy shifts to about 1 eV higher, so that more electron density is transferred from the Ni ion to the ligands, usually indicating a higher oxidation state of Ni ions. The electronic structure of the metal center is very important to the catalytic properties. Yumura et al. calculated the potential energy for formaldehyde oxidation to formic acid by FeO^+. It turns out the energy difference is about 10 kcal/mol between the sextet ($^6\Sigma^+$) and the quartet ($^4\Delta$) reaction pathways.[57] The energy difference between $FeO^+(^4\Delta)$ (electron configuration $1\sigma^2 2\sigma^2 1\pi^4 1\sigma^2 2\pi^2 3\sigma^1$ or $1\sigma^2 2\sigma^2 1\pi^4 1\sigma^3 2\pi^2 3\sigma^0$) and $FeO^+(^6\Sigma^+)$ (electron configuration $1\sigma^2 2\sigma^2 1\pi^4 1\sigma^2 2\pi^2 3\sigma^1$) is about 1.0 eV.[58] The formaldehyde oxidation is shifted by about 0.08 V with DNA-Ni, which corresponds to about 1.84 kcal/mol. It is possible the energy state difference of Ni along with the coordination environment (the unique DNA aggregate structure) leads to this energy

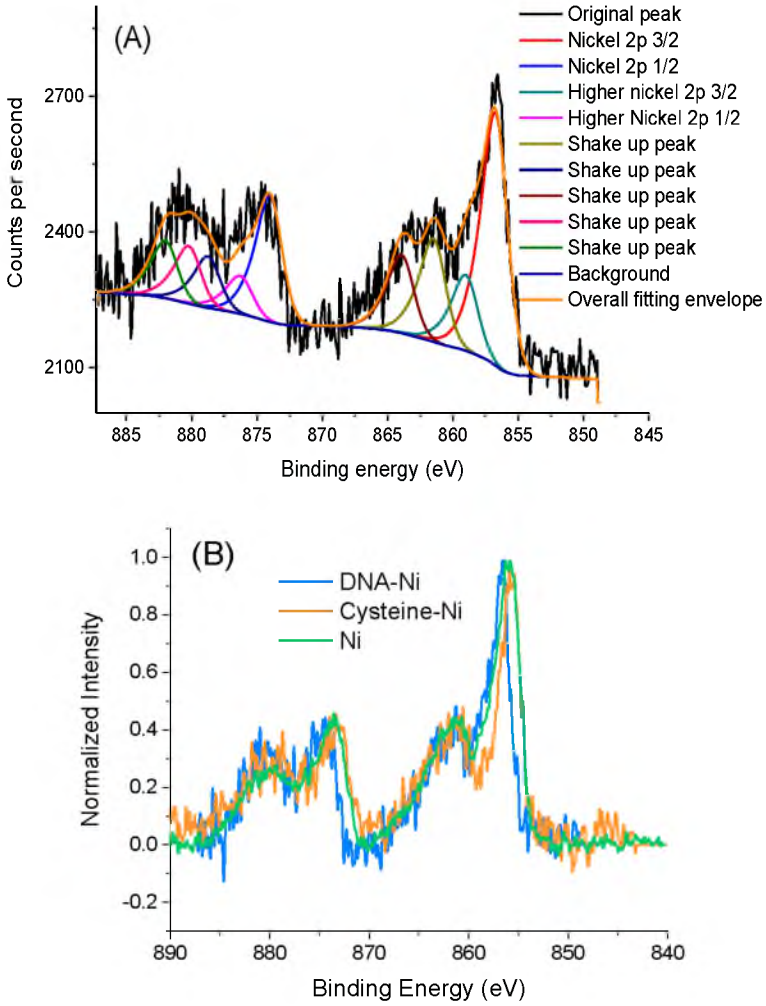

Figure 3.11. XPS Ni 2p spectra: (A). XPS high-resolution deconvolution Ni 2p spectra (Asymetric peak shape for peaks, CasaXPS peak shape parameter = A(0.2,0.5,30)GL(30), with FWHM 2.20eV). (B). DNA-Ni spectrum compared to cysteine-Ni and Ni spectra in Chapter 2.

difference.

In summary, the bases in DNA and DNA-Ni aggregates were oxidized during electrodeposition. Ni ions can interact with water, imine, carbonyl (carboxylate groups if they exist) and phosphate groups in DNA-Ni aggregates. The intramolecular electron transfer properties of DNA-Ni aggregates could be the reason that makes the electronic structure of Ni in DNA aggregates different from Ni with small ligands. DNA-Ni aggregates have some interesting features similar to oxidoreductase enzymes. They contain both hydrophobic and hydrophilic groups, have a large hydrogen bonding network and a large amount of amine, imine, carbonyl, and carboxylate groups. When compared to oxidoreductase enzymes, DNA-Ni aggregates have much higher metal center density, coordinating with imines and other groups that can mimic histidines and other residues in enzymes' catalytic pockets. Moreover, the higher metal center density will probably bring DNA-Ni aggregates much better electron transfer ability than many enzymes, so DNA-aggregates with metal centers may make intriguing alternatives to enzymes. Furthermore, based on the analysis of AFM, UV-Vis and XPS, the calf thymus DNA used in this study did not preserve its original double-stranded structure when forming the aggregates, so in principle, other polymer backbones modified with specific ligands can also form these kind of aggregates that provide microenvironments that can alter the catalytic properties of metal centers.

3.4 Conclusion

Fuel diversity was tested with Ni and DNA-Ni electrodes. Both of them have catalytic activities for oxidizing methanol, ethanol, glycerol, and glucose. Methanol, glycerol, and

glucose can be completely or deeply oxidized, as shown by the presence of carbonate in the fuel solution. This phenomenon makes nickel-based catalysts a candidate for fuel cell electrocatalysts. DNA-Ni aggregates prepared by electrodeposition at 1.8 V form nanoparticles, which create a coordination environment that can change the electronic structure of the Ni centers. The DNA aggregates also make the Ni centers close to functional groups such as imine, carbonyl, and carboxylate groups. These effects make DNA-Ni oxidize formaldehyde and formate differently from Ni with small ligands, including nucleotides, and can completely oxidize methanol at a lower potential. Aggregates formed from polymers modified with various functional groups (represented by DNA in this chapter) could serve as intriguing scaffolds that alter the catalytic properties of metal centers.

3.5 References

(1) Arechederra, R. L.; Minteer, S. D. *Fuel Cells* **2009**, *9*, 63.

(2) Gupta, K. C.; Kumar Sutar, A.; Lin, C.-C. *Coord. Chem. Rev.* **2009**, *253*, 1926.

(3) Schlosser, K.; Li, Y. *Chem. Biol.* **2009**, *16*, 311.

(4) Roelfes, G. *Mol. Biosyst.* **2007**, *3*, 126.

(5) Travascio, P.; Li, Y.; Sen, D. *Chem. Biol.* **1998**, *5*, 505.

(6) Li, H.; Carter, J. D.; LaBean, T. H. *Mater. Today* **2009**, *12*, 24.

(7) Kanan, M. W.; Rozenman, M. M.; Sakurai, K.; Snyder, T. M.; Liu, D. R. *Nature* **2004**, 545.

(8) Oltra, N. S.; Roelfes, G. *Chem. Commun. (Cambridge, England)* **2008**, *44*, 6039.

(9) Liu, Y.; Wei, W.; Liu, X.; Zeng, X.; Li, Y.; Luo, S. *Microchim. Acta* **2010**, *168*, 135.

(10) Costa, C.; Vecherskaya, M.; Dijkema, C.; Stams, A. J. M. *J. Ind. Microbiol. Biotechnol.* **2001**, *26*, 9.

(11) Bambagioni, V.; Bianchini, C.; Marchionni, A.; Filippi, J.; Vizza, F.; Teddy, J.; Serp, P.; Zhiani, M. *J. Power Sources* **2009**, *190*, 241.

(12) Lin, X.; Jiang, X.; Lu, L. *Biosens. Bioelectron.* **2005**, *20*, 1709.

(13) Rippe, K.; Mücke, N.; Langowski, J. *Nucleic Acids Res.* **1997**, *25*, 1736.

(14) Oliveira Brett, A. M.; Chiorcea, A.-M. *Electrochem. Commun.* **2003**, *5*, 178.

(15) Andrushchenko, V.; Leonenko, Z.; Cramb, D.; van de Sande, H.; Wieser, H. *Biopolymers* **2002**, *61*, 243.

(16) Chiorcea-Paquim, a.-M.; Corduneanu, O.; Oliveira, S. C. B.; Diculescu, V. C.; Oliveira-Brett, a. M. *Electrochim. Acta* **2009**, *54*, 1978.

(17) *Nucleic Acids in Chemistry and Biology*; Third ed.; The Royal Society of Chemistry: United Kingdom, 2006.

(18) Eisenberg, H. *Acc. Chem. Res.* **1987**, *20*, 276.

(19) Osada, K.; Shiotani, T.; Tockary, T. A.; Kobayashi, D.; Oshima, H.; Ikeda, S.; Christie, R. J.; Itaka, K.; Kataoka, K. *Biomaterials* **2012**, *33*, 325.

(20) Ojani, R.; Raoof, J.; Zavvarmahalleh, S. *Electrochim. Acta* **2008**, *53*, 2402.

(21) Bambagioni, V.; Bianchini, C.; Marchionni, A.; Filippi, J.; Vizza, F.; Teddy, J.; Serp, P.; Zhiani, M. *J. Power Sources* **2009**, *190*, 241.

(22) Liu, Y.; Wei, W.; Zeng, X.; Liu, X. *Catal. Commun.* **2010**, *11*, 884.

(23) Huang, W.; Li, Z.; Peng, Y.; Niu, Z. *Chem. Commun.* **2004**, 1380.

(24) Spinner, N.; Mustain, W. E. *Electrochim. Acta* **2011**, *56*, 5656.

(25) Koper, M. T. M. *Fuel Cell Catalysis : A Surface Science Approach*; John Wiley & Sons, Inc.: Hoboken, New Jersey, 2009.

(26) Gomes, J. F.; Tremiliosi-Filho, G. *Electrocatalysis* **2011**, *2*, 96.

(27) Fujiwara, N.; Yamazaki, S.-i.; Siroma, Z.; Ioroi, T.; Senoh, H.; Yasuda, K. *Electrochem. Commun.* **2009**, *11*, 390.

(28) Luo, M. Z.; Baldwin, R. P. *J. Electroanal. Chem.* **1995**, *387*, 87.

(29) Yu, X.; Pickup, P. G. *J. Power Sources* **2008**, *182*, 124.

(30) Aslam, N. M.; Masdar, M. S.; Kamarudin, S. K.; Daud, W. R. W. *APCBEE Procedia* **2012**, *3*, 33.

(31) Sigel, H.; Sigel, R. K. O. *Metal Ions in Life Sciences*; John Wiley & Sons Ltd: England, 2007; Vol. 2.

(32) Naumann, C. F.; Sigel, H. *J. Am. Chem. Soc.* **1974**, *96*, 2750.

(33) Sorokin, V. A.; Valeev, V. A.; Gladchenko, G. O.; Sysa, I. V.; Blagoi, Y. P.; Volchok, I. V. *J. Inorg. Biochem.* **1996**, *63*, 79.

(34) Abrescia, N. G.; Malinina, L.; Fernandez, L. G.; Huynh-Dinh, T.; Neidle, S.; Subirana, J. a. *Nucleic Acids Res.* **1999**, *27*, 1593.

(35) Wang, L.; Liu, R.; Teng, Y. *J. Lumin.* **2011**, *131*, 705.

(36) Stangret, J.; Savoie, R. *Phys. Chem. Chem. Phys.* **2002**, *4*, 4770.

(37) Oliveira-Brett, A. M.; Piedade, J. A. P.; Silva, L. A.; Diculescu, V. C. *Anal. Biochem.* **2004**, *332*, 321.

(38) Zhu, J.; Fleming, A. M.; Orendt, A. M.; Burrows, C. J. *J. Org. Chem.* **2016**, *81*, 351.

(39) Hart, J. P. *Electroanalysis of Biologically Important Compounds*; Ellis Horwood Limited: Market Cross House, Cooper Street, Chichester, West Sussex, PO19 1EB, England, 1990.

(40) Wagner, J. R.; Cadet, J. *Acc. Chem. Res.* **2010**, *43*, 564.

(41) Ptasińska, S.; Stypczyńska, A.; Nixon, T.; Mason, N. J.; Klyachko, D. V.; Sanche, L. *J. Chem. Phys.* **2008**, *129*, 065102.

(42) Lee, C.-Y.; Gong, P.; Harbers, G. M.; Grainger, D. W.; Castner, D. G.; Gamble, L. J. *Anal. Chem.* **2006**, *78*, 3316.

(43) Papageorgiou, A. C.; Fischer, S.; Reichert, J.; Diller, K.; Blobner, F.; Klappenberger, F.; Allegretti, F.; Seitsonen, A. P.; Barth, J. V. *ACS Nano* **2012**, *6*, 2477.

(44) Higo, M.; Miake, T.; Mitsushio, M.; Yoshidome, T.; Ozono, Y. *Anal. Sci.* **2008**, *24*, 313.

(45) Ebrahimi, M.; Rios, J. F.; Leung, K. T. *J. Phys. Chem. C* **2009**, 281.

(46) Jiang, L.; Zhuang, J.; Ma, Y.; Yang, B.; Yang, W.; Li, T. *New J. Chem.* **2003**, *27*, 823.

(47) Jermakowicz-Bartkowiak, D.; Kolarz, B. N.; Tylus, W. *Polymer* **2003**, *44*, 5797.

(48) Le Manchet, S.; Verchère, D.; Landoulsi, J. *Thin Solid Films* **2012**, *520*, 2009.

(49) Katsonis, N.; Vicario, J.; Kudernac, T.; Visser, J.; Pollard, M. M.; Feringa, B. L. *J. Am. Chem. Soc.* **2006**, *128*, 15537.

(50) Clarke, R. C.; Latham, K.; Rix, C. J.; Hobday, M. *Chem. Mater.* **2004**, *9*, 2463.

(51) Ariza, M. J.; Rodríguez-Castellón, E.; Rico, R.; Benavente, J.; Muñoz, M.; Oleinikova, M. *J. Colloid Interface Sci.* **2000**, *226*, 151.

(52) Lehninger, A.; Nelson, D. L.; Cox, M. M. In *Lehninger Principles of Biochemistry*; Fifth Edition ed.; W. H. Freeman and Company: 41 Madison Avenue New York, NY 10010, 2008.

(53) Bonds, L.-b. H.; Ghosh, A.; Moulder, J.; Bröring, M. *Science* **2001**, 431.

(54) Faldum, T.; Meisel, W.; Gutlich, P. *Surf Interface Anal.* **1996**, *24*, 68.

(55) Wettig, S. D.; Li, C.-Z.; Long, Y.-T.; Kraatz, H.-B.; Lee, J. S. *Anal. Sci.* **2003**, *19*, 23.

(56) Matienzo, J.; Yin, L. I.; Grim, S. O.; Swartz, W. E. *Inorg. Chem.* **1973**, *12*, 2762.

(57) Yumura, T.; Amenomori, T.; Kagawa, Y.; Yoshizawa, K. *J. Phys. Chem. A* **2002**, *106*, 621.

(58) Fiedler, A.; Schrtider, D.; Shaik, S.; Schwarz, H. *J. Am. Chem. Soc.* **1994**, *116*, 10734.

CHAPTER 4

MECHANISTIC STUDY OF NICKEL-BASED CATALYSTS FOR OXYGEN EVOLUTION COMPARED TO METHANOL OXIDATION REACTIONS IN ALKALINE MEDIUM

Nickel-based catalysts have been studied as catalysts either for organic (especially methanol) oxidation or oxygen evolution reactions in alkaline media for decades, but methanol oxidation and oxygen evolution reactions occur at a similar potential range and pH with nickel-based catalysts. In contrast to previous studies, we studied these two reactions simultaneously under various pH and methanol concentrations with electrodes of a series of NiOOH surface concentrations. We found out that nickel-based catalysts are more suitable to be used as oxygen evolution catalysts than methanol oxidation catalysts, based on the observation that: the rate-determining step of methanol oxidation involves NiOOH, OH^-, and methanol, while high methanol to OH^- ratio could poison the NiOOH sites. Since NiOOH is involved in the rate-determining step, methanol oxidation suffers from high overpotential and oxygen evolution is favored over methanol oxidation in the presence of equivalent amounts (0.1 M) of alkali and methanol.

4.1 Introduction

Currently the world is facing an energy crisis, and efficiently using renewable energy is of extreme importance. One of the solutions is using fuel cells as power sources, because they offer cleaner, more efficient alternatives to the combustion of gasoline and other fossil fuels.[1] Both oxygen evolution and methanol oxidation reactions are intensively studied by electrochemists. Oxygen evolution is the anodic half reaction of water splitting that stores energy from sunlight to hydrogen. Methanol oxidation is the anodic half reaction which occurs in direct methanol fuel cells to convert chemical energy in methanol to electricity. The two reactions are shown in Chapter 1, equation (1.6) and (1.2).

A large number of studies have been done on nickel-based catalysts for either oxygen evolution[2] or methanol oxidation.[3] Based on the standard redox potential, methanol oxidation (E^o= -0.81 V vs. NHE at pH 14) should happen much more easily than oxygen evolution (E^o= 0.40 V vs. NHE at pH 14), but when using nickel-based catalysts, the situation is not that simple. Chapter 2 and 3 have shown that methanol oxidation and oxygen evolution occur at close potential range after Ni(III) (NiOOH) formation, and the redox potential of Ni(II)/Ni(III) sits at around 0.6 V (vs. NHE) in 0.1 M NaOH (pH 12.78).[4,5] This gives the methanol oxidation catalyzed by nickel-based catalysts a large overpotential. For a direct methanol fuel cell, if the cathode (oxygen reduction) is in the same alkaline medium, there will be little power output. Indeed, Tao et al. have constructed a methanol fuel cell using dendritic nano-sized nickel as anode catalysts and MnO_2 as the cathode catalysts to reduce humidified O_2, but 5 M methanol with 3 M KOH only produced 1.4 mA/cm^2 at 30 ^{o}C, and the open circuit potential was 0.38 V.[6]

Since Fleischmann et al. published the first results of the oxidation of organic compounds at nickel anodes in alkaline medium in 1971, there has been a debate about what the real catalytic species is.[7] Fleischmann et al. proposed the organic compounds were oxidized by NiOOH, while Taraszewska et al. proposed it is the OH^- ions "trapped" in the nickel oxide that oxidize the compounds.[8] Recently Valadbeigi et al. studied methanol oxidation in the alkali concentration range 0.05-0.5 M in the presence of 0.5 M Na_2SO_4 and concluded that both pathways exist, and at low and medium concentrations of alkali, there is no NiOOH involved.[9] The two methanol oxidation mechanisms might result from different rate-determining steps: the hydrogen abstraction from the carbon in the α-position with respect to –OH group[10] or the hydrogen abstraction from –OH group.[3] The experiments of Kuruma et al. with deuterium labelled alcohols showed the rate-determining step is the hydrogen abstraction from the carbon in the α-position with respect to –OH group.[11] Koper et al. studied a series of similar alcohols with varying pK_a in alkaline solution on gold and found that the rate-determining step is base catalyzed deprotonation from –OH group, and the second deprotonation is fast but gold catalyzed.[12] Different mechanisms could have different effects on real applications. If the methanol oxidation is mainly dependent on the NiOOH, unless an efficient way is found to decrease the redox potential of Ni(II)/Ni(III) couple, the overpotential of nickel catalyzed methanol oxidation will stay high. If methanol oxidation is more dependent on the alkali concentration, high alkali concentration could lower the overpotential, but high alkali concentration also leads to fast oxygen evolution. The two reactions will compete for the substrate and catalyst sites. It raises the question of whether it is more efficient to use nickel-based catalysts as methanol oxidation catalysts or oxygen evolution catalysts.

To answer this question, in this chapter, we prepared electrodes with NiOOH surface concentrations ranging from 10^{-9}mol/cm^2 to 10^{-7}mol/cm^2. The various NiOOH surface concentrations are achieved by using an anion exchange ionomer, AS-4, to bind nickel hydroxide nanoparticles of different sizes, respectively. Electrodes modified without AS-4 are also studied. AS-4 was developed by Tokuyama Corporation[13,14] and has been applied in alkaline fuel cells, including direct methanol fuel cells.[15-17] It has been shown to have high hydroxide conductivity and good stability in alkaline anion exchange membrane fuel cells.[18,19] In this catalyst layer, the triple-phase boundary of ion conducting phase (OH^-), electron conducting phase, and reactant phase is crucial to the performance of the electrodes. We studied methanol oxidation and oxygen evolution simultaneously, so that the roles of NiOOH, OH^-, and methanol in methanol oxidation and oxygen evolution can be clarified.

4.2 Experimental

4.2.1 Reagents and Apparatus

Methanol-^{13}C, L-cysteine and nickel (II) chloride (anhydrous, powder, 99.99% trace metals basis) were purchased from Sigma-Aldrich. Tokuyama Corporation supplied 5 wt.% AS-4 solution. The ion-exchange capacity of this resin is 1.4 mmol/g. All solutions were made with ultrapure water (Milli-Q system, 18.2 MΩ•cm) and degassed by nitrogen purging.

Three-electrode configuration was used to perform all of the electrochemical experiments. A Hg/HgO (1M NaOH) electrode or a saturated calomel electrode (SCE) was used as the reference electrode, and a platinum mesh electrode was used as the

counter electrode. The working electrode was a glassy carbon disc electrode (CH Instruments: diameter of 3 mm). The glassy carbon electrodes were polished with 1 μm and 0.05 μm alumina polish medium, successively, followed by sonication in ultrapure water and ethanol. After each experiment, the glassy carbon electrodes were soaked in a saturated ethylenediaminetetraacetate (EDTA) solution and stirred overnight to remove nickel residue, so that they can be reused. Cyclic voltammetry (CV) was carried out with a Biologic SP-150 Potentiostat/Galvanostat. Amperometry was performed with CH Instruments 611C potentiostat. Bulk electrolysis was performed with Pine Wavenow.

Modified glassy carbon plate surfaces were characterized by atomic force microscopy (Bruker Dimension Icon-PT atomic force microscope with Peak Force Tapping mode). The silicon nitride lever of AFM has a single cantilever with force constant k=0.4 N/m, resonant frequencies of f_0=50-90 kHz, and radius of curvature of 2 nm. Images were taken with 1 μm size (512 samples/line) at room temperature and analyzed with Nanoscope Analysis software version 1.20. First-order flattening was applied to the images. Bulk electrolysis products were identified with ^{13}C NMR obtained by a Varian Unity 300 MHz NMR.

4.2.2 Electrode Preparation

Three categories of nickel-based electrodes were prepared. In the first category, the precursors contain 0.01 M $NiCl_2$ and cysteine concentrations were varied from 0 M to 0.06 M, and then AS-4 was drop-cast onto the electrodes. These electrodes were denoted as Ni1 AS-4, Ni1Cys0.5 AS-4, Ni1Cys1 AS-4, Ni1Cys2 AS-4, Ni1Cys4 AS-4, Ni1Cys5 AS-4, and Ni1Cys6 AS-4, based on the $NiCl_2$ and cysteine concentrations. The second

category has Ni1 and Ni1Cys5 with no AS-4. The third category has Ni0.5Cys6 AS-4, where its precursor contains 0.005 M $NiCl_2$ and 0.06 M cysteine and AS-4 was applied on top. The procedures are summarized in Table 4.1. The nickel cysteine solutions were stirred for 3.5 hours prior to using to ensure complex formation. A 5 μL aliquot of nickel cysteine complex (with different nickel cysteine ratios) solution or $NiCl_2$ solution was drop-cast onto glassy carbon electrode surfaces. For the electrodes with AS-4, after the precursor solution was dry, 3.54 μL of AS-4 solution was drop-cast on top and allowed to dry overnight. Nickel-based catalysts were formed and attached to the electrode surfaces by CV in 0.1 M NaOH for 30 cycles from 0 V to 0.9 V vs. Hg/HgO at a scan rate of 50 mV/s. Electrodes were then tested in 0.1 M NaOH with 0.1 M methanol with CVs for 30 cycles as well. For AFM characterization, glassy carbon plates instead of glassy carbon electrodes were used.

4.2.3 Chronoamperometry

Three amperometry experiments were conducted. The first is amperometry with methanol concentrations 0 to 1 M in 0.1 M NaOH at 0.7 V versus Hg/HgO while stirring at a constant controlled rate. In each experiment, the charging current was allowed to dissipate for >1000 s, and for each methanol concentration, there were at least 300 seconds between injections to make sure steady-state current is reached. The last 50 seconds were used to calculate current density at this methanol concentration. The second experiment is in 0.1 M methanol while varying the pH from 9.37 to 13.45. The electrolyte is 0.1 M NaCl. The potential was at 0.607 V (vs. SCE) for pH from 9.37 to 12.26 and 0.7 V (vs. Hg/HgO) for pH from 12.54 to 13.45. The solution was stirred at a

Table 4.1. Preparation of nickel-based electrodes.

Category	Shortening notation	$NiCl_2$ concentrations (M)	Cysteine concentrations (M)	AS-4	Γ ($\times 10^{-8}$ mol/cm^2)
I	Ni1 AS-4	0.01	0	Applied	1.0 ± 0.2
I	Ni1Cys0.5 AS-4	0.01	0.005	Applied	2.3 ± 0.6
I	Ni1Cys1 AS-4	0.01	0.01	Applied	5.1 ± 0.8
I	Ni1Cys2 AS-4	0.01	0.02	Applied	7.1 ± 2.0
I	Ni1Cys4 AS-4	0.01	0.04	Applied	8.2 ± 1.1
I	Ni1Cys5 AS-4	0.01	0.05	Applied	11.2 ± 1.5
I	Ni1Cys6 AS-4	0.01	0.06	Applied	12.8 ± 3.2
II	Ni1	0.01	0	No	1.3 ± 0.3
II	Ni1Cys5	0.01	0.05	No	0.5 ± 0.2
III	Ni0. 5Cys6 AS-4	0.005	0.06	Applied	9.2 ± 1.5

constant controlled rate. At each pH, the current was measured for 1200s to allow charging current to dissipate, and the last 50 seconds were used to calculate current density at this pH. The third experiment is without methanol (oxygen evolution), changing pH from 9.37 to 13.47, performed similar to the second experiment.

4.2.4 Stability Tests via Bulk Electrolysis

Potentiostatic bulk electrolysis was performed with constant potential at 0.7 V (vs. Hg/HgO). The bulk electrolysis was stopped when the current dropped to 10% of the initial current. The electrodes were tested before and after bulk electrolysis in fresh solution of 0.1 M NaOH and 0.1 M NaOH with 0.1 M methanol with CVs. Bulk electrolysis products were identified with ^{13}C NMR.

4.3 Results and Discussions

4.3.1 Cyclic Voltammetry

4.3.1.1 Properties of Nickel-based Electrodes

Three categories of nickel-based electrodes were prepared and characterized by cyclic voltammetry. The procedures are summarized in Table 4.1. The first category has electrodes modified from precursors containing 0.01 M $NiCl_2$ and various cysteine concentrations and coated with AS-4. They are denoted as Ni1 AS-4, Ni1Cys0.5 AS-4, and so on. The second category has Ni1 and Ni1Cys5 with no AS-4. The third category has Ni0.5Cys6 AS-4. Representative 30^{th} cycle of cyclic voltammograms from scanning these modified electrodes are shown in Figure 4.1.

In 0.1 M NaOH (Figure 4.1A), the redox peaks belong to $Ni(OH)_2$ and NiOOH. The

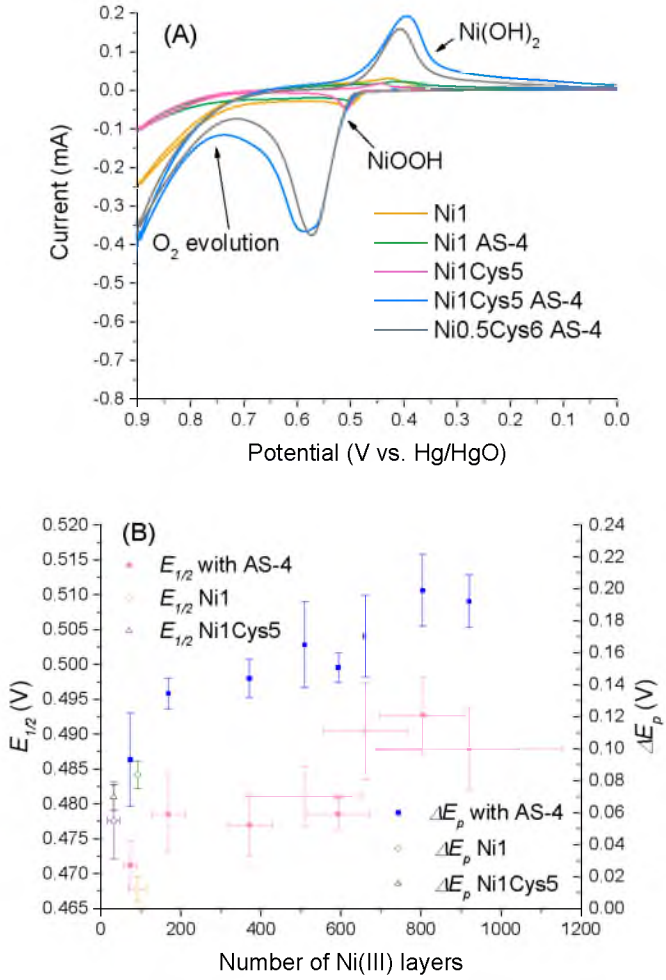

Figure 4.1. Depositing nickel catalysts onto electrode surfaces: (A) Representative 30th cycle of cyclic voltammograms from scanning electrodes modified with nickel-based catalysts in 0.1 M NaOH. Scan rate 50 mV/s. (B). $E_{1/2}$ and ΔE_p trends vs. nickel catalyst thickness.

current increase beginning at 0.7 V (vs. Hg/HgO) is due to oxygen evolution. NiOOH surface concentrations Γ are calculated in the same way as in Chapter 2 (equation 2.4). Chapter 2[20] has shown that this preparation procedure will produce nickel hydroxide nanoparticles on electrode surfaces. Higher cysteine ratio will produce smaller nanoparticles. Without AS-4 as a binder, small nanoparticles only form one particle layer (Figure 2.8 in Chapter 2) and the total NiOOH surface concentration is low (Ni1Cys5). With the AS-4 binder, the nanoparticles are bound together and the total NiOOH surface concentration is high (Ni1Cys5 AS-4). Moreover, with AS-4 binder, the smaller the nanoparticle, the higher the NiOOH surface concentration. Electrodes with NiOOH surface concentrations from 1.0 (± 0.2) × 10^{-8} mol/cm^2 (Ni1 AS-4) to 12.8 (± 3.2) × 10^{-8} mol/cm^2 (Ni1Cys6 AS-4) can thus be prepared as described in Table 4.1.

Table 4.2 summarizes properties of representative nickel-based electrodes. The precursor Ni(II) concentration is 0.01 M or 0.005 M (5μL), corresponding to NiOOH surface concentrations of 70.7 × 10^{-8} mol/cm^2 and 35.4 × 10^{-8} mol/cm^2. Because only one layer of nanoparticles was left on the electrode surfaces, Ni1Cys5 has the smallest Γ_{NiOOH}. The fact that those AS-4-bound electrodes still have a measured Γ_{NiOOH} much smaller than the theoretical value indicates that the majority of nickel sites are buried and/or there is some nickel lost even with AS-4. Since Ni0.5Cys6 AS-4 has Γ_{NiOOH} close to Ni1Cys6 AS-4, buried nickel sites should be the main reason. The number of Ni(III) layers is calculated using NiOOH surface concentrations. The unit cell of $Ni(OH)_2$ is hexagonal with a=b=3.126 Å, and Ni atoms are at the corners of the unit cell, so the number of Ni(III) layers N can be calculated by

Table 4.2. Properties of nickel-based electrodes.

Electrodes	Γ ($\times 10^{-8}$ mol/cm^2)	Number of Ni(III) layers	Estimated thickness (nm)	$E_{1/2}$ (V)	ΔE_p (mV)
Ni1	1.3 ± 0.3	92 ± 22	70 ± 17	0.468 ± 0.002	84 ± 9
Ni1 AS-4	1.0 ± 0.2	73 ± 17	56 ± 13	0.471 ± 0.003	93 ± 29
Ni1Cys5	0.5 ± 0.2	32 ± 15	37 ± 17	0.478 ± 0.006	70 ± 8
Ni1Cys5 AS-4	11.2 ± 1.5	804 ± 107	924 ± 123	0.493 ± 0.006	199 ± 23
Ni0.5Cys6 AS-4	9.2 ± 1.5	661 ± 106	760 ± 122	0.490 ± 0.007	170 ± 25

$$N = \frac{\Gamma \times N_A \times A_{uc}}{A} = \frac{\Gamma \times N_A \times (a^2 \sin 60^o)}{A} \quad (4.1)$$

where Γ is NiOOH surface concentration, N_A is the Avogadro constant, A_{uc} is the area of one unit cell, and A is the geometric surface area of the electrodes.[21] The estimated thickness is calculated by N times d (the intersheet distances of $Ni(OH)_2$, it is around 7.6 Å without cysteine and 11.5 Å with cysteine[20]). The AFM characterization (measuring the majority thickness distribution, not simply the scale bar shown in Figure 2.8) shows that the thickness of Ni1Cys5 surface is 39 ± 3 nm and Ni1 surface is 172 ± 9 nm. Considering the vacancies between the nanoparticles, Ni1Cys5 thickness measured by AFM is close to the thickness calculated from Γ_{NiOOH}, suggesting that most of the nickel sites in Ni1Cys5 are accessible to OH^-. On Ni1 surfaces, there are fused large aggregates and the thickness measured by AFM is 2.5 times the thickness calculated from Γ_{NiOOH}, suggesting a large amount of nickel sites are buried and not accessible to OH^-.

$E_{1/2}$ is the half wave redox potential of Ni(II) and Ni(III). Lower $E_{1/2}$ makes it easier to produce NiOOH, whereas ΔE_p reveals the rate of the electron transfer kinetics, which depends on the Ni(II) to Ni(III) redox transition and/or the electron exchange process at the interface between the electrode surface and the redox centers.[22] The correlations of $E_{1/2}$ and ΔE_p against the number of Ni(III) layers are depicted in Figure 4.1B. As the number of Ni(III) layers increases, both $E_{1/2}$ and ΔE_p shift to larger value, especially the ΔE_p, which is almost tripled. When comparing Ni1 and Ni1 AS-4, Ni1 AS-4 has slightly larger $E_{1/2}$ and ΔE_p values, although it has fewer nickel layers. This suggests the large amount of AS-4 could hinder the electron transfer a bit. When comparing Ni1 and Ni1Cys5, Ni1Cys5 has fewer nickel layers and the ΔE_p is smaller, but its $E_{1/2}$ is larger

than Ni1. This shows adding cysteine does not slow down the electron transfer while making NiOOH produced at slightly higher potential, so the overall trend of ΔE_p increasing as the number of Ni(III) layers increases is not due to the existence of cysteine residues but due to thicker films having slower electron transfer.

4.3.1.2 Catalytic Activities of Nickel-based Electrodes

Figure 4.2 shows that all of the nickel electrodes have activity towards methanol oxidation and it occurs after NiOOH is formed. Figure 4.3 shows CVs in 0.1 M NaOH with 0.1 M methanol and CVs in 0.1 M NaOH together for easy comparison. Bare glassy carbon electrodes as well as glassy carbon electrodes covered with AS-4 have little catalytic activity towards oxygen evolution and methanol oxidation. On the other hand, nickel-based catalysts can catalyze both methanol oxidation and oxygen evolution and their CVs all share some common features. When oxidizing methanol, the NiOOH peak shifts to higher potential because of the adsorption of methanol, and the $Ni(OH)_2$ peak becomes smaller after methanol oxidation, indicating some of the NiOOH was consumed during methanol oxidation. When the potential rises to 0.7 V (vs. Hg/HgO), the adsorbed OH^- is also oxidized and forms oxygen.

Previous studies have summarized that concentration of OH^-, morphology of the modifying film (thickness and permeability), surface concentration of active sites and charge transport through the film, and the electron transfer rate at the substrate/nickel hydroxide interface affect a catalyst's efficiency.[22-24] In the case of methanol oxidation on nickel surfaces, the chemical oxidation rate of methanol is the most important one. It is the rate-determining step. Studies show that the methanol oxidation

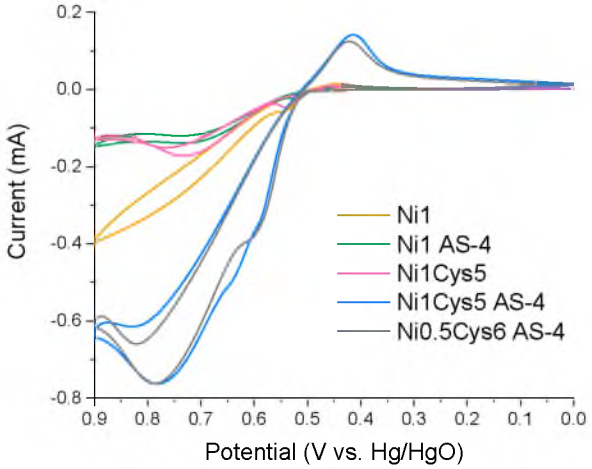

Figure 4.2. Representative 30th cycle of cyclic voltammograms from scanning electrodes modified with nickel-based catalysts in 0.1 M methanol and 0.1 M NaOH. Scan rate 50 mV/s.

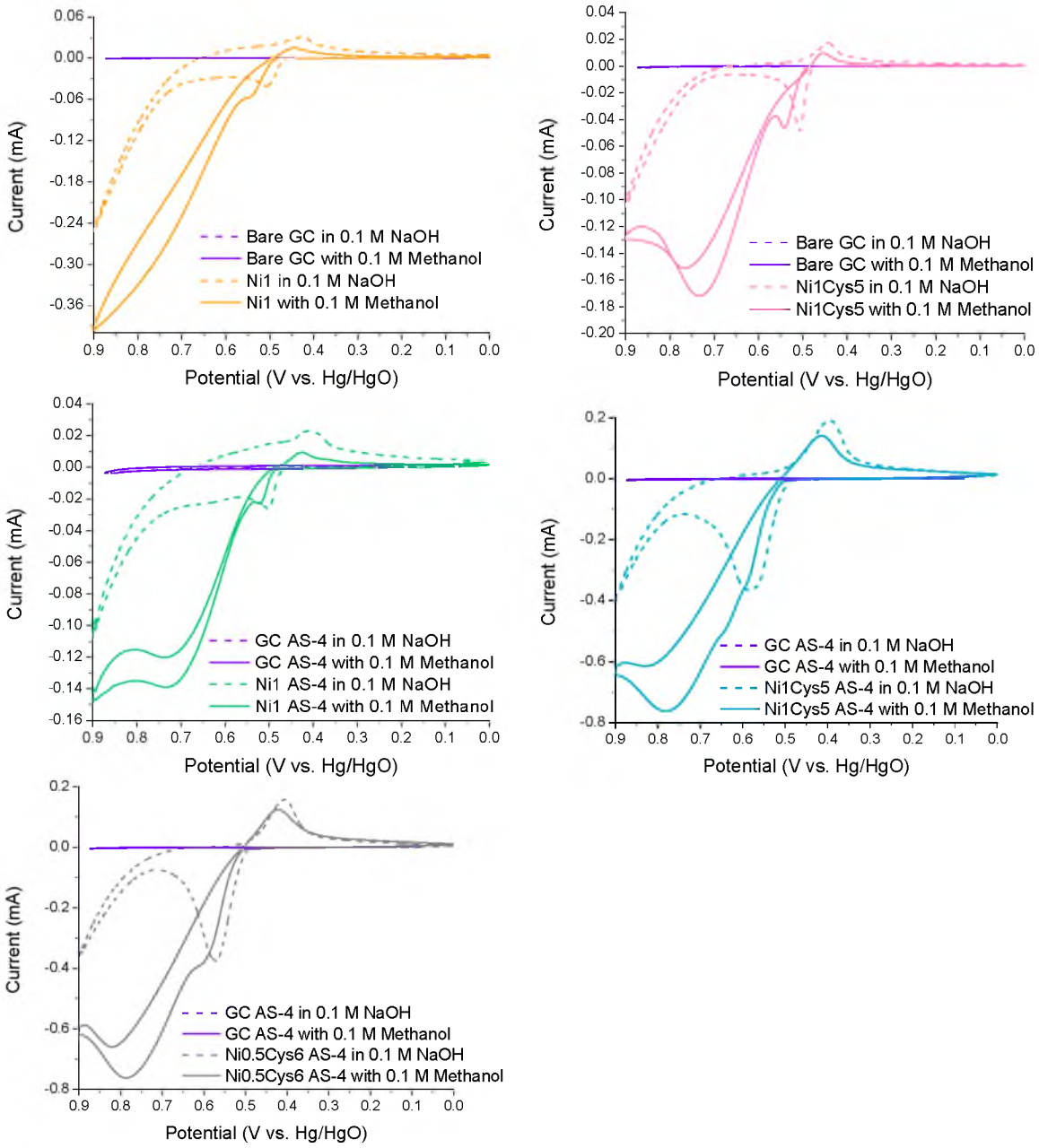

Figure 4.3. Representative 30th cycle of cyclic voltammograms from scanning Ni and NiCys AS-4 electrodes in 0.1 M NaOH and in 0.1 M NaOH with 0.1 M methanol (using the same electrode respectively). Scan rate 50 mV/s.

rate is much lower than its adsorption rate (Langmuir adsorption)[10,25] and the $Ni(OH)_2$/NiOOH transformation rate,[26] although the adsorbed methanol inhibits NiOOH formation.[25,27] However, when considering the general catalytic activity of NiOOH, the concentration of OH^- plays a very important role on both oxygen evolution and methanol oxidation. The solution pH affects the $E_{1/2}$ of Ni(II) and Ni(III) redox couple. The $E_{1/2}$ shifts to lower potential when pH increases. Lyons et al. have shown the potential shift is -0.088 V/pH unit at T=298 K[28]. Pariente et al., working with Ni-DHS (a nickel complex), obtained a similar value, -0.084 V/pH.[27] Although high pH can lead to low $E_{1/2}$, the methanol oxidation which relies on the amount of NiOOH is not always enhanced with high pH. Pariente et al. carried out CVs at pH 12.0 to pH 14.7 with 0.1 M methanol and showed that pH 13.0 gave the highest methanol oxidation current. This phenomenon could result from the competition of methanol oxidation and oxygen evolution. Methanol begins to adsorb at the onset of NiOOH formation,[29] while higher anodic potential prefers OH^- adsorption to methanol adsorption.[9] The adsorbed hydroxyl groups can also remove the methanol oxidation intermediate and generate new sites for further adsorption and reaction.[9] Thus, changing the potential and concentration of OH^- and methanol could make a different reaction dominate.

4.3.2 Chronoamperometry

As mentioned in the introduction section, clarifying the roles of NiOOH, OH^-, and methanol during methanol oxidation and oxygen evolution will be very useful to guide real electrochemical applications. We studied methanol oxidation and oxygen evolution with amperometry under stirred conditions, so that effects from diffusion are minimized

and the kinetics under steady state can be clearly studied. Three amperometry experiments were conducted. The first one was maintaining the alkaline medium at 0.1 M NaOH (pH 12.78) while adding methanol gradually to 1 M. The second one was holding the methanol concentration at 0.1 M while varying the pH from 9.37 to 13.45. The third one was without methanol to study oxygen evolution while changing the pH from 9.37 to 13.47. The potential was held at 0.7 V (vs. Hg/HgO, i.e. 0.85 V vs. NHE), which is the on-set potential in the CVs for oxygen evolution and is also close to the methanol oxidation peak position. Methanol oxidation is supposed to be favored over oxygen evolution when pH is equal to or smaller than 12.78 (0.1 M NaOH) at this potential.

4.3.2.1 Methanol Oxidation

An example of direct amperometry response is shown in Figure 4.4. The resulting calibration curve of methanol oxidation is plotted in Figure 4.5A. The corresponding turnover frequency (TOF) is calculated and plotted in Figure 4.5B. Since the main oxidation product is formate detected by ^{13}C NMR, 4 electrons per methanol molecule is used in the calculation. To address the issue of whether NiOOH is involved in methanol oxidation, logarithmic plots of the current density as a function of NiOOH concentration (using electrodes in category I, Table 4.1) are made at each methanol concentration (Figure 4.6). The resulting NiOOH reaction order is plotted versus methanol concentration in Figure 4.5C. It shows when methanol concentration is lower than 0.2 M, the NiOOH reaction order is around 0.5 and as the methanol concentration increases, the NiOOH reaction order decreases. This clearly shows that NiOOH is involved in methanol oxidation.

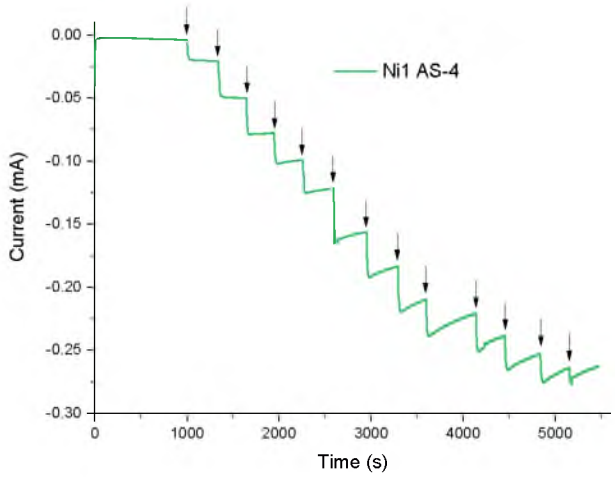

Figure 4.4. Amperometric response for electrode with 0.01 M $NiCl_2$ and 0.005 M Cysteine in 0.1 M NaOH and increasing concentrations of methanol at 0.7 V (vs. Hg/HgO). The methanol concentration is from 0 M to 1 M. The arrows represent each methanol injection. After adding methanol, the current increased immediately. At high methanol concentrations, the nickel centers were saturated and the current did not increase anymore.

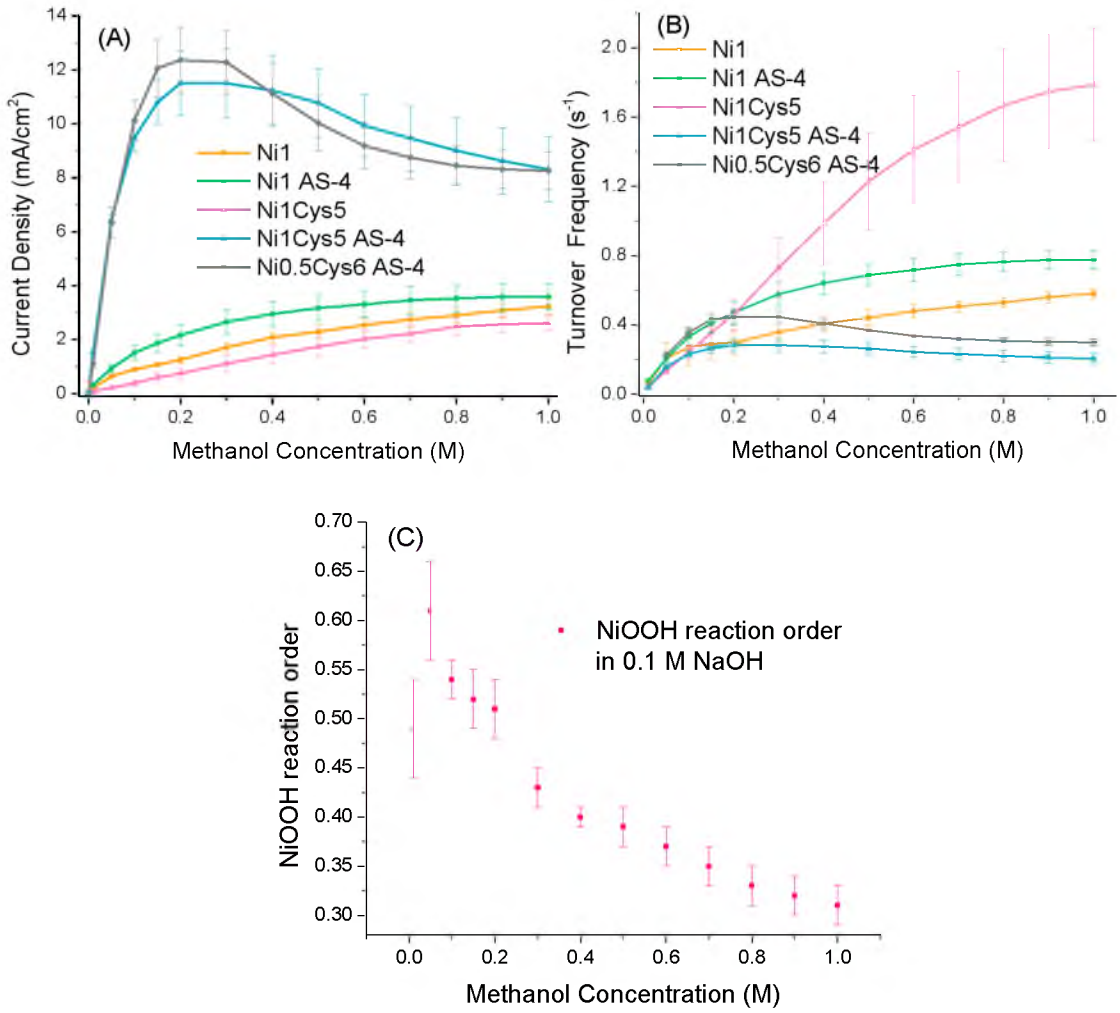

Figure 4.5. Methanol oxidation for different nickel-based electrodes: (A). Calibration curves of methanol oxidation for different nickel-based electrodes. Data were calculated from amperometry experiments (Figure 4.4). (B). Turnover frequency (TOF) of methanol oxidation with different nickel-based electrodes. (C). NiOOH reaction order change vs. methanol concentrations.

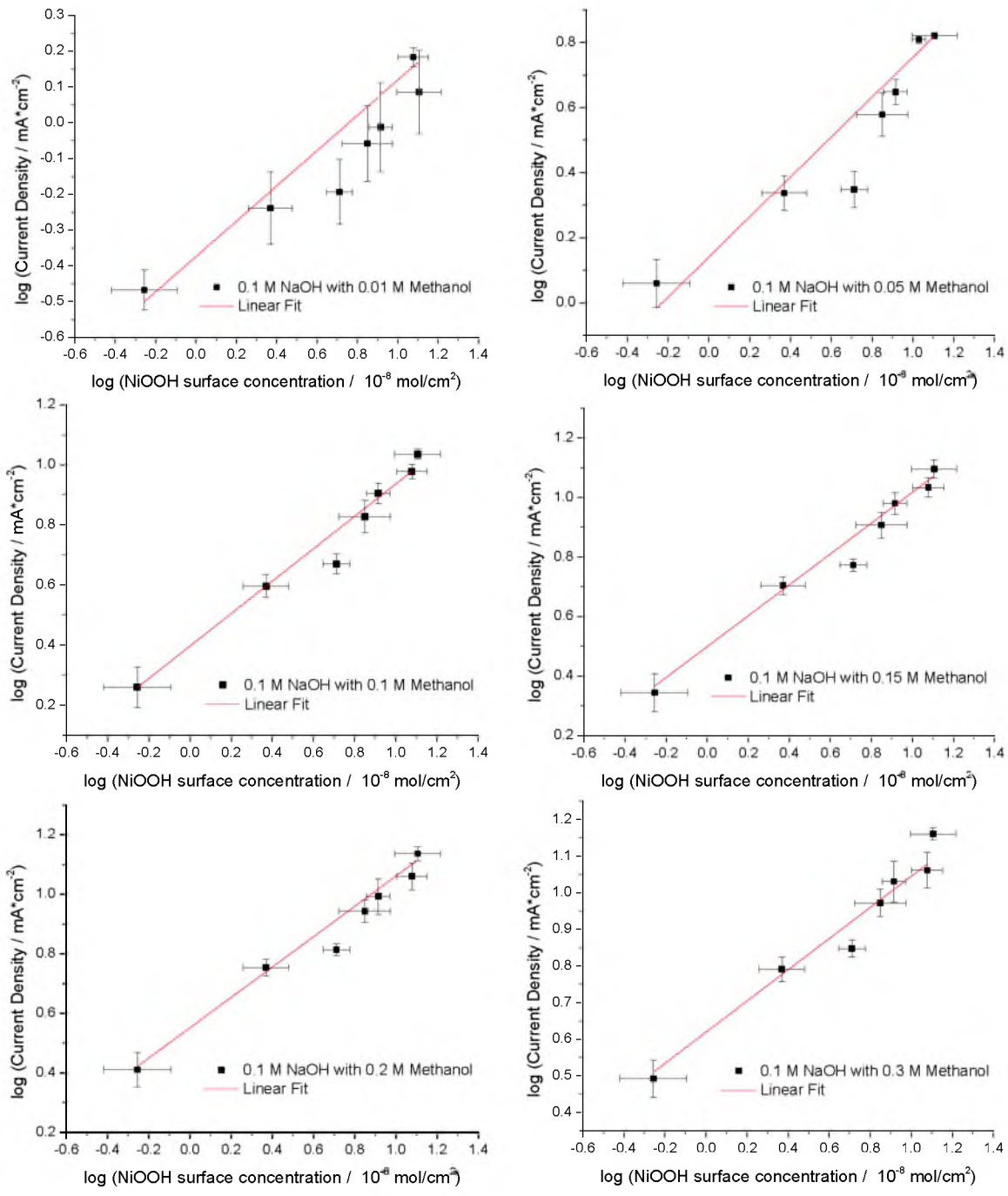

Figure 4.6. Fitting of NiOOH reaction order for methanol oxidation with 0.1 M NaOH. Electrodes were from category I.

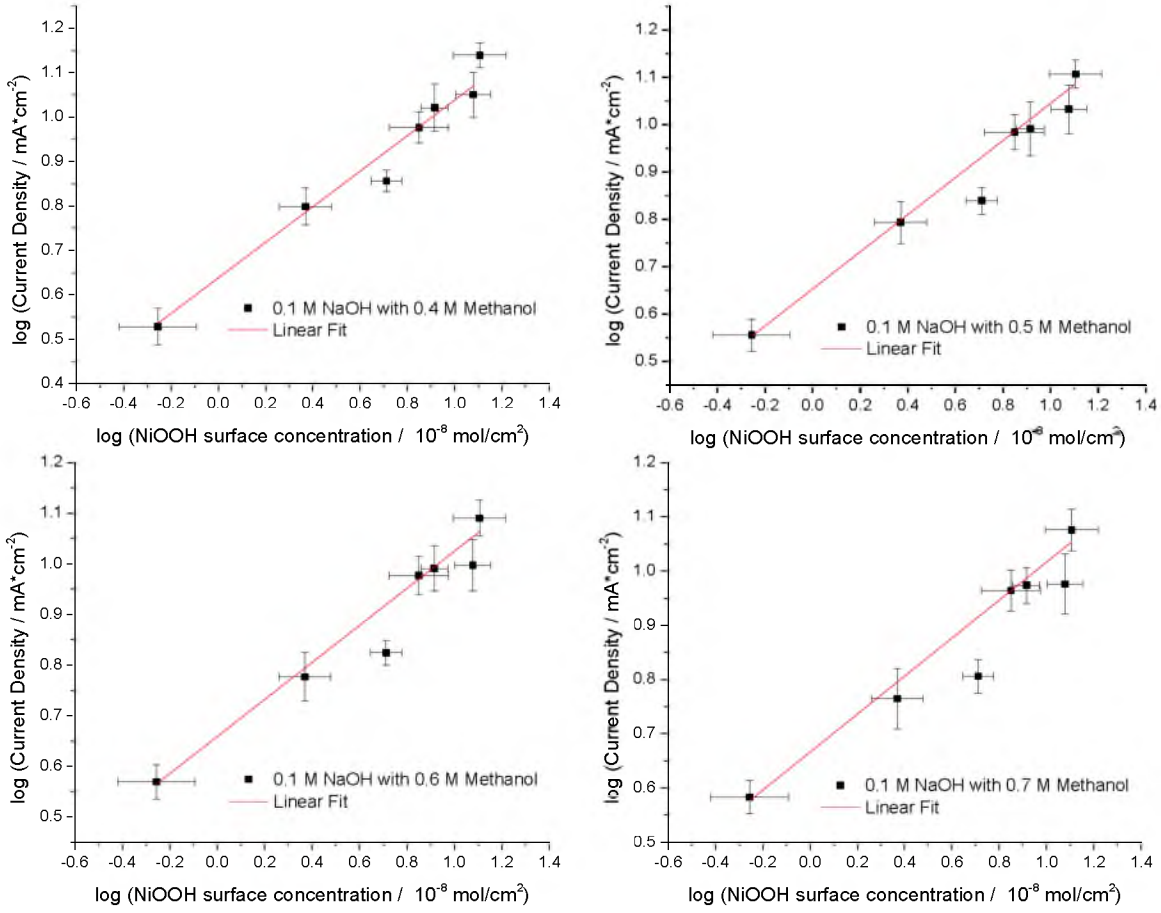

Figure 4.6 (continued).

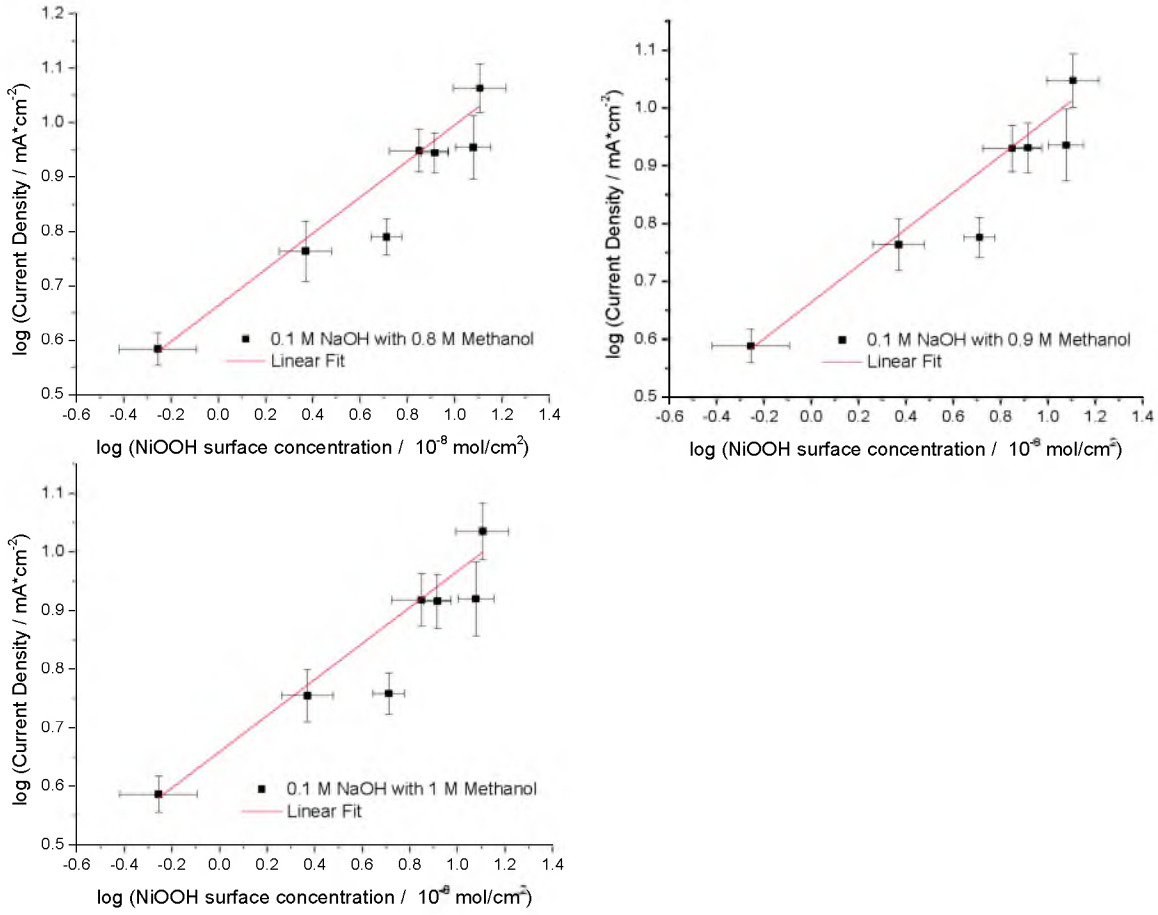

Figure 4.6 (continued).

Generally speaking, electrodes with high NiOOH surface concentrations produce high current output (Figure 4.5A.). When comparing Ni1 and Ni1 AS-4, they have approximately the same amount of NiOOH, but Ni1 AS-4 has higher current output. This indicates the AS-4 layer does not hinder the methanol oxidation in this concentration range with catalyst surfaces that are not very porous. Electrodes with high NiOOH surface concentration, Ni1Cys5 AS-4 and Ni0.5Cys6 AS-4, show current decreases at methanol concentration higher than 0.2 M. The decrease is more severe with Ni0.5Cys6 AS-4. As discussed in section 4.3.1.1, these two electrodes have catalytic layers thicker than the other three and are more porous than Ni1 and Ni1 AS-4, but less porous than Ni1Cys5. Ni0.5Cys6 AS-4 is more porous than Ni1Cys5 AS-4, so without the AS-4 layer, thin porous catalyst layers do not suffer this activity loss in high methanol concentration, but more porous layers suffer more activity loss when AS-4 is present. At least two possibilities could account for this activity loss. The first one is that some toxic oxidation intermediate is adsorbed on the NiOOH sites. As more and more intermediates are adsorbed, the poisoning effect becomes more and more limiting. However, in situ FTIR and Raman spectroscopy only detect methanol, formate, and carbonate on the catalyst surfaces.[29,30] CVs in 0.1 M NaOH with 0.1 M formaldehyde also show nickel-based catalysts catalyze formaldehyde oxidation extremely quickly in alkaline medium,[31] so the only remaining possible poisoning species is formate. Since NiOOH is hydrophobic,[25] methanol should be more competitive than formate to be adsorbed. Thus this intermediate poisoning theory is less likely. The other possibility is that methanol itself is the poison. Logarithmic plots of the current density as a function of methanol concentration are presented in Figure 4.7. Only the first few points are fitted with Ni1

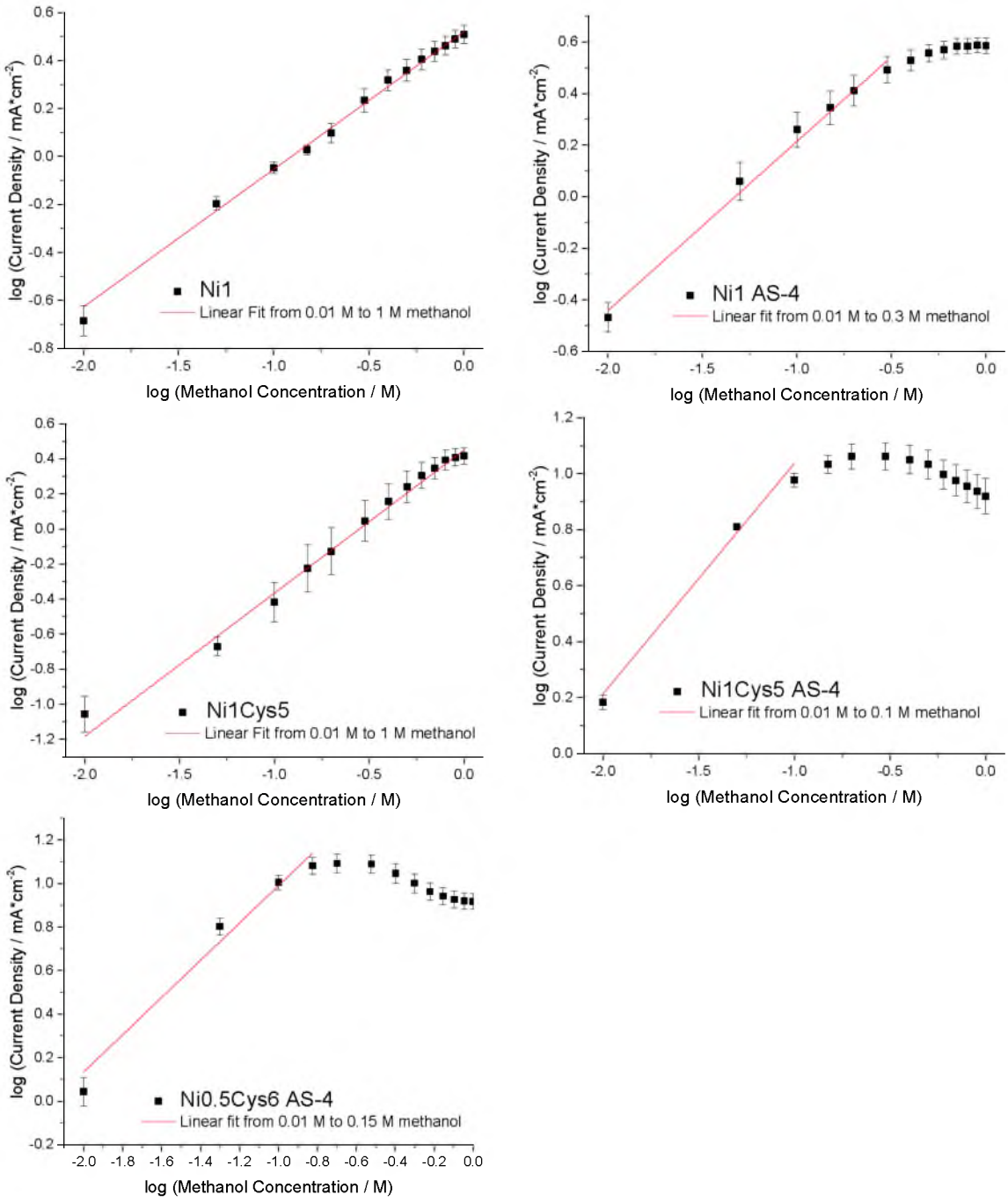

Figure 4.7. Fitting of methanol reaction order in methanol oxidation with 0.1 M NaOH. The resulting methanol reaction orders are Ni1 0.57 ± 0.01; Ni1 AS-4 0.66 ± 0.03; Ni1Cys5 0.82 ± 0.02; Ni1Cys5 AS-4 0.82 ± 0.11; Ni0.5Cys6 AS-4 0.86 ± 0.12.

AS-4, Ni1Cys5 AS-4, and Ni0.5Cys6 AS-4, because at higher methanol concentration the plot is no longer linear. They show that Ni electrodes (Ni1 and Ni1 AS-4) have a methanol reaction order of approximately 0.6 and NiCys electrodes (Ni1Cys5, Ni1Cys5 AS-4 and Ni0.05Cys6 AS-4) are 0.8. The reaction order difference indicates adding ligands could alter the kinetics with methanol, while AS-4 does not have this effect. Discussion in section 4.3.2.2 will show the reaction order of OH^- in methanol oxidation is 1. The reaction rate is more dependent on OH^- concentration in this case. When methanol concentration is much higher than OH^-, less OH^- can be adsorbed on NiOOH sites and the reaction is lower. Langmuir plots (Figure 4.8) for these electrodes support this theory. Ni1Cys5 and Ni1 AS-4 fit very well with a Langmuir plot, suggesting the oxidation follows a Langmuir adsorption and the oxidation is much slower than its adsorption.[25] When methanol concentration is lower than 0.2 M, all of the electrodes have similar TOFs, so the methanol oxidation rates of Ni1Cys5 AS-4 and Ni0.05Cys6 AS-4 are also lower than the methanol Langmuir adsorption rate. Langmuir adsorption indicates one active site can be occupied by one particle at a maximum and active sites are independent. Ni1Cys5 AS-4 and Ni0.05Cys6 AS-4 only obey Langmuir adsorption at methanol concentration lower than 0.1 M. Higher methanol concentration changes the adsorption model and interrupts the methanol oxidation. This also indicates thick porous films with AS-4 adsorb methanol more easily, probably because methanol molecules are trapped in the catalyst structure. In addition, in high methanol concentration where NiOOH sites get poisoned, the NiOOH reaction order decreases. Ni1Cys5 has only one thin nanoparticle layer on electrode surfaces, that is, it is a quite open porous structure, so it is not significantly affected by the poisoning by methanol in this concentration range.

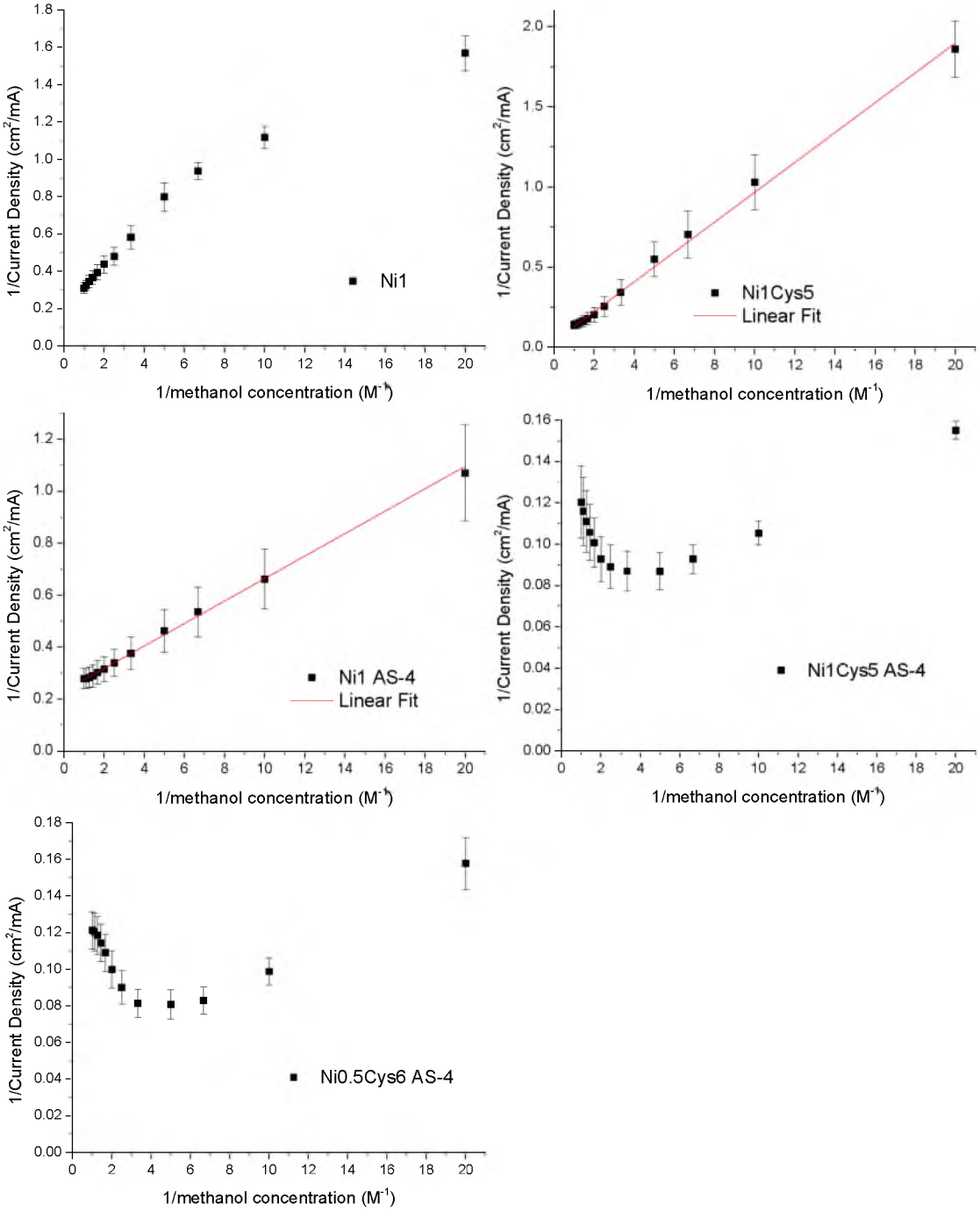

Figure 4.8. Langmuir plot of methanol (0.05 M to 1.0 M) adsorption in 0.1 M NaOH.

Ni1 is also not poisoned by methanol, because of its methanol reaction order that does not change with methanol concentration, as shown in Figure 4.7. When comparing Ni1Cys5 to Ni1, Ni1Cys5 has much higher TOF, probably due to its small particle size, so Ni1Cys5 has the highest activity towards methanol oxidation. On the other hand, the overall current output of Ni1Cys5 is low because only a small amount of nickel catalyst is immobilized on electrode surfaces. In real electrochemical applications, growing these small nickel nanoparticles onto a conductive framework with close to micron size pores could greatly optimize the current output.

4.3.2.2 Competition between Methanol Oxidation and Oxygen Evolution

Amperometry experiments were performed at 0.7 V with and without 0.1 M methanol at different pHs (from 9.37 to 13.47, 0.1 M NaCl as electrolyte). Since the redox potential of Ni(II)/Ni(III) is dependent on pH, a too low pH could lead to no NiOOH formation. If the redox potential of Ni(II)/Ni(III) is at 0.7 V, the pH for different electrodes will be Ni1 10.02, Ni1 AS-4 10.06, Ni1Cys5 10.13 and Ni1Cys5 AS-4 10.31 (using -0.084V/pH from the work of Pariente et al.[27] to do the calculation).

An example of direct amperometric response is shown in Figure 4.9. Calibration curves of 0.1 M methanol oxidation with oxygen evolution and oxygen evolution with no methanol are calculated and plotted in Figure 4.10A and B, respectively. The corresponding TOFs are calculated and plotted in Figure 4.10C and D. Both methanol oxidation and oxygen evolution have 4 electrons transferred per molecule, so 4 electrons is used in the calculation of TOF. The TOF calculated in Figure 4.10D is also the TOF of oxygen evolution. The difference of the data from Figure 4.10C and D gives the TOF of

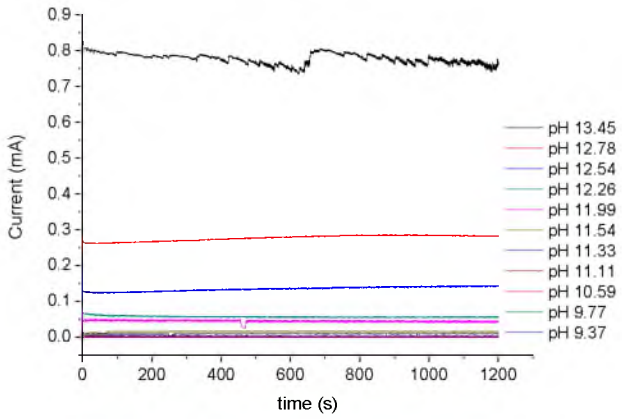

Figure 4.9. Representative amperometric response for Ni1 electrode with 0.01 M $NiCl_2$ in 0.1 M Methanol at a series pH at 0.607 V (vs. SCE) and 0.7 V (vs. Hg/HgO). For each pH value, current densities were taken at steady state, averaged from t = 1150s -1200 s.

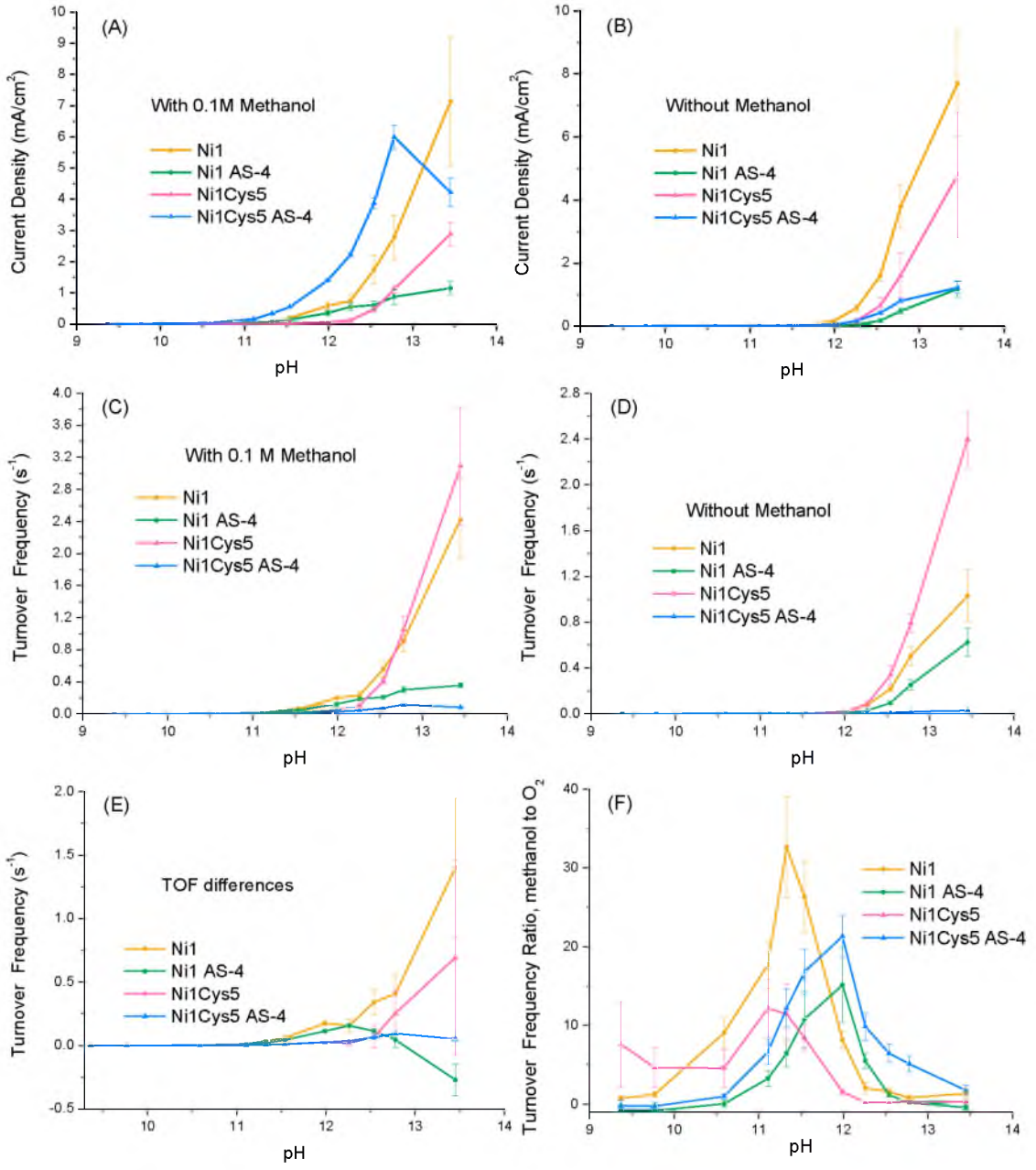

Figure 4.10. (A) and (B) are calibration curves for different nickel-based electrodes at different pH. Data were calculated from amperometry experiments (e.g., Figure 4.9). (A).With 0.1 M methanol. (B).Without methanol. (C) and (D) are TOF of different nickel-based electrodes. (C).With 0.1 M methanol. (D).Without methanol, i.e. TOF_{oxygen}. (E). The difference between (C) and (D), the result of $TOF_{with\ methanol}$ minus $TOF_{no\ methanol}$, i.e. $TOF_{methanol}$ (F). $TOF_{methanol}$ over TOF_{oxygen}.

0.1 M methanol oxidation at different pH, which is plotted in Figure 4.10E. Figure 4.10F plots the ratio of TOF of 0.1 M methanol over TOF of oxygen, reflecting the preference of methanol oxidation or oxygen evolution at different pH at 0.7 V. This calculation method for TOF of 0.1 M methanol is only valid when the two reactions do not interfere with each other, that is, when the pH is relatively low. In the case of Ni1 AS-4, when pH is larger than 12.78, its TOF of 0.1 M methanol is negative. This indicates that the two reactions interfere with each other and methanol oxidation has slower kinetics than oxygen evolution under this condition at Ni1 AS-4 surfaces. Because methanol occupied some catalytic sites that could have been occupied by OH^- to generate oxygen, the overall current decreased in the presence of methanol. However, the data in Figure 4.10F can show whether the higher current output is from methanol oxidation or oxygen evolution in the whole pH range.

Using these data, the reaction orders of OH^- are also obtained (Figure 4.11 and Figure 4.12). The reaction order of OH^- is about 1 in the presence of 0.1 M methanol and about 2 with pure oxygen evolution in high pH range. Most of the reactions occur at pH larger than the pH calculated for NiOOH formation. Ni1Cys5 has the highest TOF towards oxygen evolution, and Ni1 has the highest methanol oxidation TOF with 0.1 M methanol. In Figure 4.10F, electrodes without AS-4 show the highest methanol preference, around pH 11.33, while electrodes with AS-4 have this pH shifted to 11.99. AS-4 could somehow adjust the OH^- adsorption on NiOOH at low pH range. The electrode that favors methanol oxidation the most is Ni1. Methanol oxidation can occur at lower pH than oxygen evolution, but at this range the overall current output is also low. AS-4 shifted methanol preference to pH 11.99, but at this pH the overall current output is still

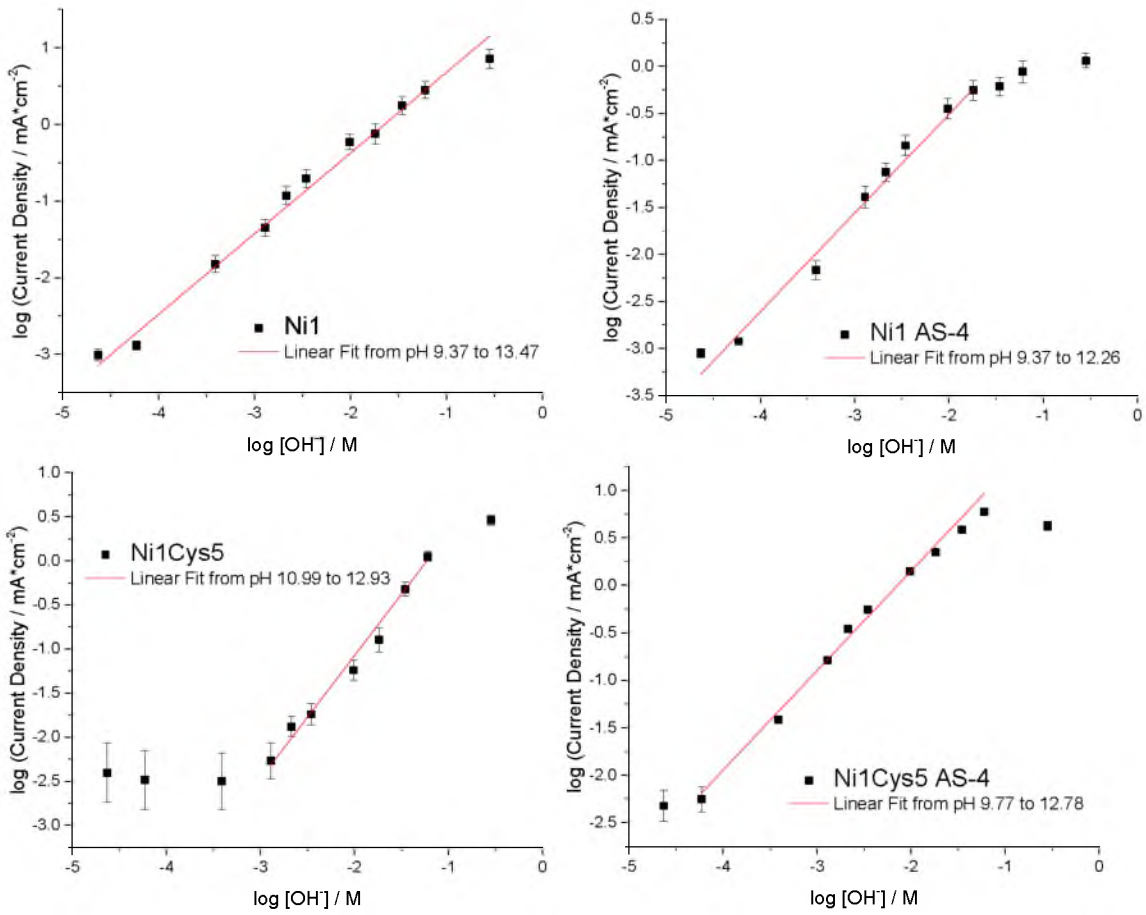

Figure 4.11. Fitting of OH^- reaction order in the presence of 0.1 M methanol. The resulting OH^- reaction orders are Ni1 1.05 ± 0.04; Ni1AS-4 1.05 ± 0.06; Ni1Cys5 1.40 ± 0.07; Ni1Cys5 AS-4 1.05 ± 0.05.

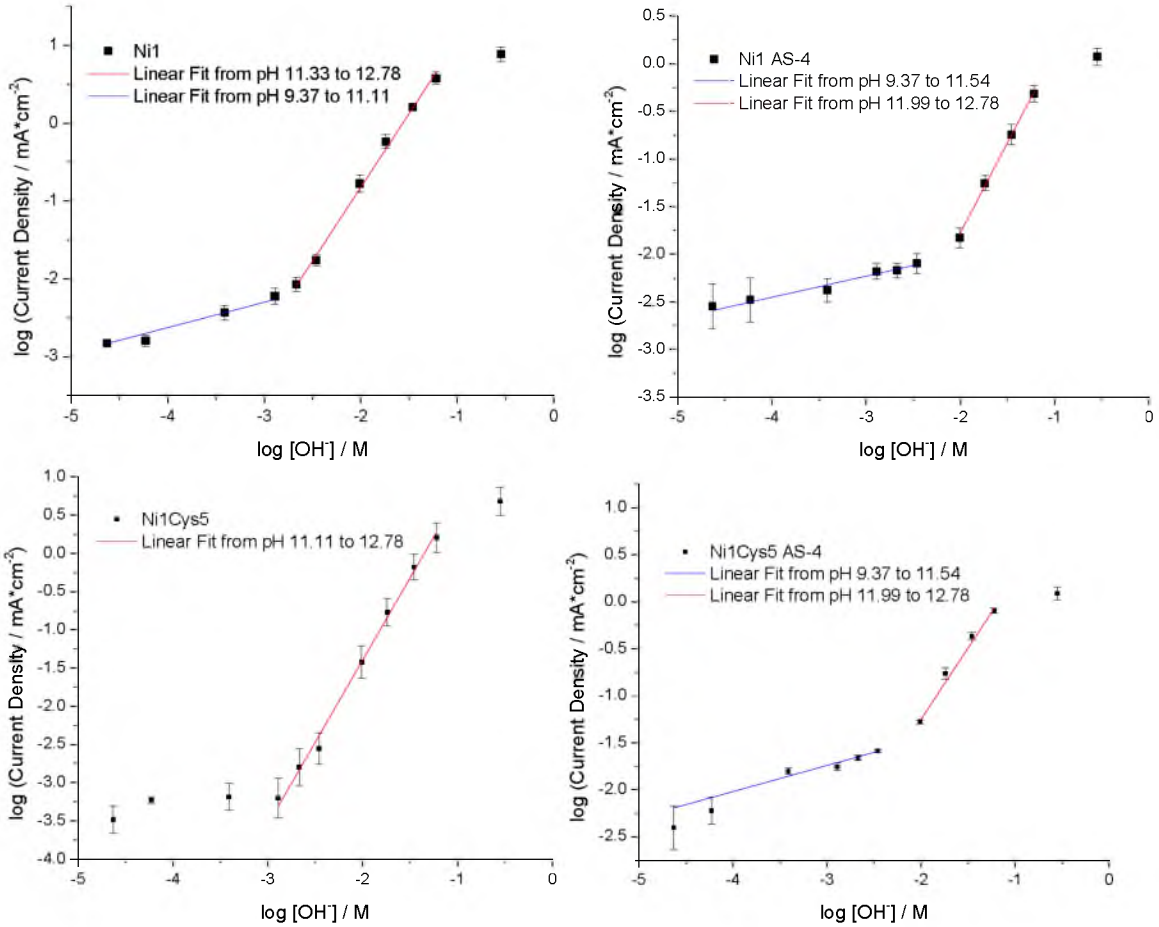

Figure 4.12. Fitting of OH^- reaction order with oxygen evolution reaction. The resulting OH^- reaction orders in the high pH range are Ni1 1.89 ± 0.05; Ni1AS-4 1.89 ± 0.06; Ni1Cys5 2.15 ± 0.07; Ni1Cys5 AS-4 1.51 ± 0.07. In the low pH range are: Ni1 0.33 ± 0.04; Ni1AS-4 0.22 ± 0.03; Ni1Cys5 about 0; Ni1Cys5 AS-4 0.28 ± 0.04.

low, so the effect is limited. Oxygen evolution is favored over methanol oxidation at pH higher than 12.78. Thus at high pH (0.1 M NaOH or more concentrated alkali) with 0.1 M methanol, the majority of the current is produced from oxygen evolution. The overall current output at this pH range is also high. From this point of view, using nickel-based catalysts to catalyze oxygen evolution is more efficient than using them to catalyze methanol oxidation.

4.3.3 Electrode Stability Test

Potentiostatic bulk electrolysis was performed in 0.1 M NaOH and 0.1 M ^{13}C-methanol to evaluate how well Ni1 AS-4 and Ni1Cys5 AS-4 electrodes can work continuously. Figure 4.13 shows an example of the raw data. Table 4.3 summarizes the main parameters calculated from potentiostatic bulk electrolysis data, and it shows that Ni1Cys5 AS-4 electrodes have a larger amount of current passed and thus convert more substrate than Ni1 AS-4 electrodes when they were both stopped at 10% of the initial current. The current drop is caused by NiOOH loss. After bulk electrolysis the AS-4 layer disappeared, and this leads to the nickel loss since the AS-4 layer is the key component to bind the thick catalyst layer on the electrode surfaces. The disappearance of AS-4 could partially result from the formation of oxygen bubbles, which detached the AS-4 layer from the electrode surfaces. Improving the stability of AS-4 layer on the electrode surfaces during bulk electrolysis is expected to greatly improve the electrode stability. Various solutions could resolve this issue. For instance, using porous electrode, for example, Toray paper electrodes, will greatly enlarge the contact surface area, and the catalysts and the binder can be filled in the pores.

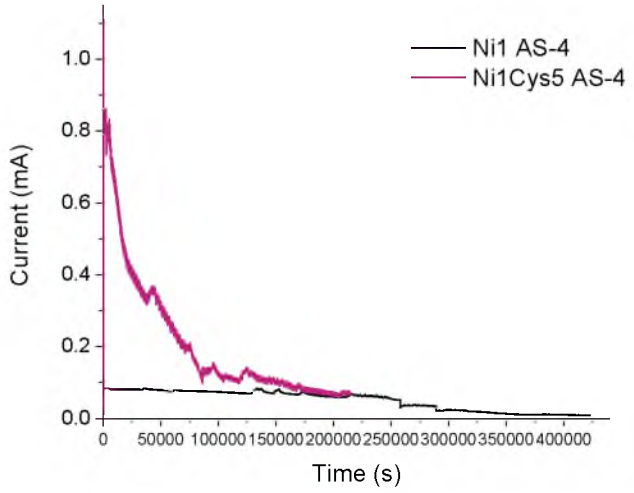

Figure 4.13. Potentiostatic bulk electrolysis of Ni1 AS-4 and Ni1Cys5 AS-4 electrodes in 0.1 M NaOH and 0.1 M ^{13}C-methanol. The potential is hold at 0.7 V (vs. Hg/HgO).

Table 4.3. Bulk electrolysis data comparison.

	Ni1 AS-4	Ni1Cys5 AS-4
Nickel Concentration (M)	0.01	0.01
Cysteine Concentration (M)	0	0.05
Duration time (hour)	125.20± 38.82	44.89 ± 11.45
Charge (coulomb)	24.68 ± 2.56	38.34 ± 3.54
NiOOH loss[a]	78.8% ± 6.4%	92.2% ± 9.7%
Methanol oxidation current decrease[a]	80.9% ± 7.2%	93.0% ± 1.2%

a. NiOOH loss and methanol oxidation current decreases at 0.7 V (vs. Hg/HgO) are calculated by data extracted from CVs taken before and after the bulk electrolysis.

4.4 Conclusions

With our experimental conditions, the rate-determining step of methanol oxidation involves three species, NiOOH (with the reaction order around 0.5), OH^- (with the reaction order around 1) and methanol (with the reaction order 0.6 to 0.8). High methanol to OH^- ratio could poison the NiOOH sites during methanol oxidation. Oxygen evolution is preferred over methanol oxidation when equivalent amounts (0.1 M) of alkali and methanol are present. The catalyst binder AS-4 can hold a large amount of nickel sites onto the electrode surface to increase the overall current output and facilitate methanol oxidation over oxygen evolution to some extent, but stability studies indicate the formation of oxygen bubbles might detach the AS-4 layer from electrode surfaces. This problem is easier to resolve than trying to decrease the overpotential of methanol oxidation. Unless the redox potential of Ni(II)/Ni(III) can be decreased without increasing OH^- concentration, nickel-based catalysts are more suitable to be used as a catalyst for oxygen evolution rather than methanol oxidation.

4.5 References

(1) Office of Energy Efficiency & Renewable Energy, U. S. D. o. E., Ed.; 2014: http://energy.gov/eere/fuelcells/fuel-cells, 2014; Vol. 2014.

(2) Trotochaud, L.; Ranney, J. K.; Williams, K. N.; Boettcher, S. W. *J. Am. Chem. Soc.* **2012**, *134*, 17253.

(3) Cardoso, W. S.; Dias, V. L. N.; Costa, W. M.; Araujo Rodrigues, I.; Marques, E. P.; Sousa, A. G.; Boaventura, J.; Bezerra, C. W. B.; Song, C.; Liu, H.; Zhang, J.; Marques, A. L. B. *J. Appl. Electrochem.* **2008**, *39*, 55.

(4) Oliva, P.; Leonardi, J.; F., L. J. *J. Power Sources* **1982**, *8*, 229.

(5) El-Shafei, A. A. *J. Electroanal. Chem.* **1999**, *471*, 89.

(6) Ewing, S. J.; Lan, R.; Xu, X.; Tao, S. *Fuel Cells* **2009**, *10*, 72.

(7) Fleischmann, M.; Korinek, K.; Pletcher, D. *J. Electroanal. Chem. Interfacial Electrochem.* **1971**, *31*, 39.

(8) Taraszewska, J.; Roslonek, G. *J. Electroanal. Chem.* **1994**, *364*, 209.

(9) Gobal, F.; Valadbeigi, Y.; Kasmaee, L. M. *J. Electroanal. Chem.* **2011**, *650*, 219.

(10) Casella, I. G.; Cataldi, T. R. I.; Salvi, A. M.; Desimoni, E. *Anal. Chem.* **1993**, *65*, 3143.

(11) Konaka, R.; Terabe, S.; Kuruma, K. *J. Org. Chem.* **1969**, *34*, 1334.

(12) Kwon, Y.; Lai, S. C.; Rodriguez, P.; Koper, M. T. *J. Am. Chem. Soc.* **2011**, *133*, 6914.

(13) Yanagi, H.; Fukuta, K. *ECS Trans.* **2008**, *16*, 257.

(14) Fukuta, K.; Inoue, H.; Chikashige, Y.; Yanagi, H. *ECS Trans.* **2010**, *28*, 221.

(15) Wang, Y. J.; Qiao, J.; Baker, R.; Zhang, J. *Chem. Soc. Rev.* **2013**, *42*, 5768.

(16) Leng, Y.; Chen, G.; Mendoza, A. J.; Tighe, T. B.; Hickner, M. A.; Wang, C. Y. *J. Am. Chem. Soc.* **2012**, *134*, 9054.

(17) Prakash, G. K. S.; Krause, F. C.; Viva, F. A.; Narayanan, S. R.; Olah, G. A. *J. Power Sources* **2011**, *196*, 7967.

(18) Yang, D.; Yu, H.; Li, G.; Zhao, Y.; Liu, Y.; Zhang, C.; Song, W.; Shao, Z. *J. Power Sources* **2014**, *267*, 39.

(19) Khadke, P. S.; Krewer, U. *J. Phys. Chem. C* **2014**, *118*, 11215.

(20) Chen, D.; Giroud, F.; Minteer, S. D. *J. Electrochem. Soc.* **2014**, *161*, F933.

(21) Cibrev, D.; Jankulovska, M.; Lana-Villarreal, T.; Gómez, R. *Int. J. Hydrogen Energy* **2013**, *38*, 2746.

(22) Ciszewski, A.; Milczarek, G. *J. Electroanal. Chem.* **1996**, *413*, 137.

(23) Trevin, S. p.; Bedioui, F.; Villegas, M. G. G.; Bied-Charreton, C. *J. Mater. Chem.* **1997**, *7*, 923.

(24) Ojani, R.; Raoof, J.-B.; Zavvarmahalleh, S. R. H. *Electrochim. Acta* **2008**, *53*, 2402.

(25) Ureta-Zañartu, M. S.; Alarcón, A.; Muñoz, G.; Gutiérrez, C. *Electrochim. Acta* **2007**, *52*, 7857.

(26) Golabi, S. M.; Nozad, A. *Electroanalysis* **2004**, *16*, 199.

(27) Revenga-Parra, M.; García, T.; Lorenzo, E.; Pariente, F. *Sens. Actuators B Chem.* **2008**, *130*, 730.

(28) Lyons, M. E. G.; Russell, L.; O'Brien, M.; Doyle, R. L.; Godwin, I.; Brandon, M. P. *Int. J. Electrochem. Sci.* **2012**, *7*, 2710.

(29) Kowal, A.; Portb, S. N.; Nicholsb, R. J. *Catal. Today* **1997**, *38*, 483.

(30) Huang, W.; Li, Z. L.; Peng, Y. D.; Chen, S.; Zheng, J. F.; Niu, Z. J. *J. Solid State Electrochem.* **2005**, *9*, 284.

(31) Chen, D.; Lee, G. G. W.; Minteer, S. D. *ECS Electrochem. Lett.* **2012**, *2*, F9.

CHAPTER 5

CONCLUSION AND FUTURE WORK

The catalytic properties of nickel-based electrocatalysts in alkaline medium for fuel oxidation and oxygen evolution have been explored in this dissertation. Nickel-based electrocatalysts can deeply oxidize small alcohols (methanol and ethanol) as well as more complicated fuels (glycerol and glucose) with carbon-carbon bonds broken. The output current can be enhanced by growing nickel-based nanoparticles on electrode surfaces of smaller sizes. This can be achieved by adding cysteine to the precursor solution to adjust the solubility of $Ni(OH)_2$ during the nanoparticle growth in alkaline medium. The oxidation mechanism of methanol can also be modified by having DNA aggregates as scaffolds for nickel centers. However, these alcohol oxidations catalyzed by current nickel-based electrocatalysts suffer from high overpotential, that is, low power output in fuel cells, as well as the poisoning of the NiOOH active sites in high concentration of the substrate, that is, it is difficult to obtain high energy density. Meanwhile, nickel-based electrocatalysts have very high activity with low overpotential towards the water oxidation reaction, in other words, oxygen evolution reaction, the anodic reaction of the water splitting, so current nickel-based electrocatalysts are more suitable to be used as water oxidation catalysts. Coupling nickel-based electrocatalysts to photoelectrodes to do solar water splitting will be the future research direction.

Since Fujishima and Honda reported using a TiO_2 film as a photoelectrode in 1972,[1] a lot of work has been done using semiconductors as photoelectrodes. During this photolysis process, sunlight is absorbed by TiO_2 or other semiconductors to produce electron-hole pairs. The electrons and holes can be separated and move to the electrode-electrolyte interface, where the holes can oxidize water/OH^- to O_2 while the electrons can reduce H^+/water to H_2, so the energy of sunlight is converted into chemical energy in H_2 fuel, but these semiconductors usually suffer from poor utilization of solar energy, high charge-carrier recombination rates, slow kinetics of surface reactions and poor stabilities.[2,3] TiO_2 has a 3 eV (3 eV for rutile phase and 3.2 eV for anatase phase) band gap, so it can only absorb UV light (shorter than 400 nm), corresponding to a theoretical maximum energy conversion efficiency at 2.2%. The minority carrier (hole) diffusion length is around 70 nm, and to absorb 90% of the light above the band gap, the film thickness should be on the order of 1 μm, so most of the holes and electrons recombine before they reach the TiO_2/H_2O interface.[2] Moreover, the slow kinetics of the reaction makes even fewer holes and electrons to actually convert energy before their recombination.

To improve the efficiency of the photoanode, a photoanode with three components will be constructed (Figure 5.1). The semiconductor will be in the middle with one side of a metal transparent electrode and the other side of $NiO/Ni(OH)_2$ nanoparticles. The metal transparent electrode will be fabricated with nano patterns to have surface plasmon resonances (SPR).[4] SPR can increase the absorption cross-section[2], and the excited plasmons can decay into electron-hole pairs through electron-electron interactions to increase photocurrent so that visible light can also be utilized.[5] Silver is chosen to be

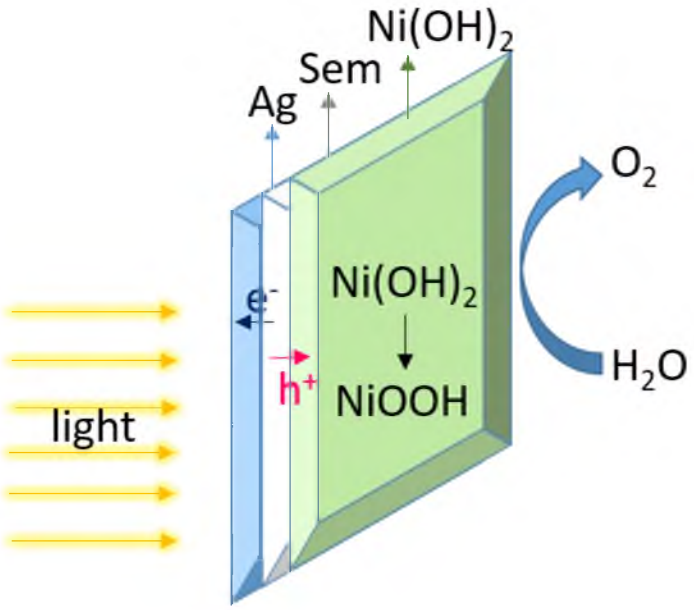

Figure 5.1. The diagram of the photoanode design.

the electrode material for three reasons. First, Ag has strong SPR in the visible range. Second, the flat band potential of metallic Ag is -4.26 eV, close to that of anatase TiO_2 (-4.2 eV), so when Ag contacts with TiO_2, photogenerated electrons can flow towards Ag and finally be conducted to the cathode to do H_2 evolution through the external circuit. Because the holes will flow towards the $NiO/Ni(OH)_2$ nanoparticles and the electrons will flow towards Ag layer, less electron-hole recombination is expected. Third, the melt point of Ag is 961.78 °C, so the nanometer thick layer of Ag can stand the 500 °C sinter process to have TiO_2 crystalized during the electrode preparation. $NiO/Ni(OH)_2$ is a p-type semiconductor. $Ni(OH)_2$ layer has been deposited onto TiO_2 to increase water oxidation efficiency as an electrocatalyst.[6,7] A p-n junction[8] or a so-called adaptive semiconductor/electrocatalyst junction[7] can be formed between $Ni(OH)_2$ and TiO_2. Under illumination, holes will flow to $Ni(OH)_2$ and oxidize it to NiOOH. NiOOH can further oxidize water to O_2.

A porous structure of these three components will be made to have large surface area, long path length of light, and good mass transfer. Polystyrene microspheres with a diameter of 372 nm will be used as template materials. Layers of polystyrene microspheres will be deposited onto the metal transparent electrode surfaces and then Ag will be deposited to the voids among the polystyrene microspheres to form a porous scaffold. TiO_2 precursor solution will be spin-coated to the Ag porous scaffold and then sintered at 500 °C to have crystalline TiO_2. Finally, $NiO/Ni(OH)_2$ nanoparticles will be deposited onto the TiO_2 surfaces by electrochemical methods.

5.1 References

(1) Fujishima, A.; Honda, K. *Nature* **1972**, *238*, 37.

(2) Liu, M.; de Leon Snapp, N.; Park, H. *Chem. Sci.* **2011**, *2*, 80.

(3) Sivula, K.; Zboril, R.; Formal, F. L.; Robert, R.; Weidenkaff, A.; Tucek, J.; Frydrych, J.; Grätzel, M. *J. Am. Chem. Soc.* **2010**, *132*, 7436.

(4) Morfa, A. J.; Akinoglu, E. M.; Subbiah, J.; Giersig, M.; Mulvaney, P. *J. Appl. Phys.* **2013**, *114*, 054502.

(5) Lee, H.; Lee, Y. K.; Hwang, E.; Park, J. Y. *J. Phys. Chem. C* **2014**, *118*, 5650.

(6) Kostecki, R.; Richardson, T.; McLarnon, F. *J. Electrochem. Soc.* **1998**, *145*, 2380.

(7) Lin, F.; Boettcher, S. W. *Nat. Mater.* **2014**, *13*, 81.

(8) Chen, C.-J.; Liao, C.-H.; Hsu, K.-C.; Wu, Y.-T.; Wu, J. C. S. *Catal. Commun.* **2011**, *12*, 1307.